https://lib.uliege.be https://matheo.uliege.be

Master thesis and internship[BR]- [BR]-

Auteur : Puissant, Gauthier
Promoteur(s) : Hillewaert, Koen
Faculté : Faculté des Sciences appliquées
Diplôme : Master en ingénieur civil en aérospatiale, à finalité spécialisée en "aerospace engineering"
Année académique : 2025-2026
URI/URL : http://hdl.handle.net/2268.2/25209

Avertissement à l'attention des usagers :

Tous les documents placés en accès ouvert sur le site le site MatheO sont protégés par le droit d'auteur. Conformément aux principes énoncés par la "Budapest Open Access Initiative"(BOAI, 2002), l'utilisateur du site peut lire, télécharger, copier, transmettre, imprimer, chercher ou faire un lien vers le texte intégral de ces documents, les disséquer pour les indexer, s'en servir de données pour un logiciel, ou s'en servir à toute autre fin légale (ou prévue par la réglementation relative au droit d'auteur). Toute utilisation du document à des fins commerciales est strictement interdite.

Par ailleurs, l'utilisateur s'engage à respecter les droits moraux de l'auteur, principalement le droit à l'intégrité de l'oeuvre et le droit de paternité et ce dans toute utilisation que l'utilisateur entreprend. Ainsi, à titre d'exemple, lorsqu'il reproduira un document par extrait ou dans son intégralité, l'utilisateur citera de manière complète les sources telles que mentionnées ci-dessus. Toute utilisation non explicitement autorisée ci-avant (telle que par exemple, la modification du document ou son résumé) nécessite l'autorisation préalable et expresse des auteurs ou de leurs ayants droit.

University of Liège - School of Engineering and Computer Science

---

Design and Evaluation of Plasma Neutralization Techniques to Produce Hyperthermal Flows Representative of VLEO Conditions

---

Master's thesis completed in order to obtain the degree of
Master of Science in Aerospace Engineering
by
Gauthier Puissant

Thesis supervisors
Professor Koen Hillewaert
University of Liège

Professor Thierry Magin
von Karman Institute for Fluid Dynamics

Jury members
Prof. Koen Hillewaert, Prof. Thierry Magin, Prof. Vincent Terrapon

Academic year 2025-2026

Abstract

The very low Earth orbits (VLEO) offers major advantages over more traditional low Earth orbit (LEO) altitudes in terms of spatial resolution and signal latency. However, operating at these lower altitudes implies interaction with a rarefied atmosphere dominated by atomic oxygen, at orbital velocities of the order of 8 km/s. These interactions lead to aerodynamic drag and material erosion over prolonged periods. Air-breathing electric propulsion (ABEP), is one of the most promising concepts to enable sustained operation in VLEO by collecting the residual atmosphere and using it as propellant to counteract drag forces. To support ABEP development, the von Karman Institute operates the DRAG-ON facility, which produces a fast particle flow representative of VLEO energies. The main limitation of DRAG-ON is that the particle flow is composed of ion species, whereas the orbital environment is essentially neutral. The present work therefore aims to improve the representativeness of DRAG-ON by developing and experimentally validating a practical ion neutralization strategy.

Several neutralization approaches compatible with DRAG-ON constraints are compared, and the perforated plate concept is selected as the most suitable compromise between efficiency, integration simplicity, and preservation of a globally axial flow. To evaluate the performance of this concept, an apparent neutralization efficiency metric is defined from empirical data. A series of experimental campaigns is conducted to map the influence of operating conditions and plate geometry. The results show that perforated plates can strongly reduce the transmitted ion current and achieve high apparent neutralization efficiencies, with clear trends indicating improved performance for higher aspect ratio plates. However, measurements also reveal an unexpected increase in ion energy downstream of the plate, suggesting an additional acceleration mechanism likely linked to plasma potential effects. Finally, a novel polyimide erosion experiment is performed as an indirect neutral diagnostic, providing evidence of a significant neutral contribution downstream of the neutralizer.

Overall, this work demonstrates that perforated plate neutralization is a promising solution to reduce the ionic fraction of the DRAG-ON particle flow. At the same time, it highlights the need for further investigation of the underlying physics and for improved neutral diagnostics to fully quantify the neutral flux properties. These developments are necessary steps toward achieving a truly VLEO-representative ground facility for ABEP intake testing and material degradation studies.

Keywords: Very low Earth orbit (VLEO) – Air-breathing electric propulsion (ABEP) – Rarefied plasma flow – Atomic oxygen (AO) – Ion neutralization – Polyimide erosion

Acknowledgements

I would like to express my sincere gratitude to my promoters, Prof. Koen Hillewaert and Prof. Thierry Magin, for agreeing to supervise this work and giving me the opportunity to carry out my master's thesis at the von Karman Institute. I would like to especially thank Prof. Thierry Magin for his guidance and valuable feedback throughout this semester.

My thanks also go to the DRAG-ON team. Pedro Jorge was always able to point me in the right direction. His reflections on experimental design were a constant source of inspiration. I also thank Damien Le Quang for his structured and practical support in this work. Finally, I would like to thank Mikel Spillemaekers, who was always available to help around the facility, and provided the most useful advice during the experimental campaigns.

More broadly, I would like to thank all the students and staff at VKI. Their welcoming atmosphere made me feel at home from the start, and this experience will stay with me for a long time.

Last but not least, I would like to thank my friends for making my academic journey an enjoyable ride, and especially my family for their continued support over the years. Merci pour tout ce que vous avez rendu possible.

Contents

List of Figures

List of Tables

Chapter 1

Introduction

Since the launch of the first artificial satellite, the number of objects placed in orbit has kept increasing steadily. Today, space is not only a strategic environment, but also a huge laboratory used to observe the Earth, monitor climate, enable navigation and communication services, and perform scientific measurements that are difficult or impossible from the ground. A large fraction of these missions operate in Low Earth Orbit (LEO), typically between a few hundred and about 2000 km altitude, where the distance to the surface enables high spatial resolution and low-latency links.

In the constant effort to obtain better data (finer resolution, improved signal-to-noise ratio, and shorter revisit times), one simple idea comes back often: get closer to the target. Over the last years, this has motivated an interest for operating satellites at significantly lower altitudes than classical LEO, in a region commonly referred to as Very Low Earth Orbit (VLEO). The major difficulty is that at these altitudes the residual atmosphere is no longer negligible, which introduces significant aerodynamic drag and environmental constraints. This master's thesis is part of the broader research effort aiming at enabling robust ground testing of technologies required for VLEO missions.

1.1 The Very Low Earth Orbit

There is no single strict boundary defined for orbit categories, but in this work the term VLEO is used to describe altitudes ranging from ~ 160 km to ~ 250 km [8]. Figure 1.1 provides a visual overview of common orbit families and helps position VLEO with respect to classical LEO and higher orbits.

Two missions are often cited as reference for demonstration of sustained operation in the very low Earth orbit environment. The ESA GOCE mission (Gravity field and steady-state Ocean Circulation Explorer) operated on a very low orbit using an ion thruster to compensate drag and enabled high-accuracy gravity field measurements. GOCE is a strong reference because it showed the performance benefits of going very low, but also highlighted the need for active drag compensation and careful system design. Over the course of its mission GOCE used around 40 kg of Xenon to provide thrust, this fuel reserve being the limiting factor in mission longevity [9]. A second reference is JAXA's SLATS (Super Low Altitude Test Satellite), which demonstrated extended operations at extremely low

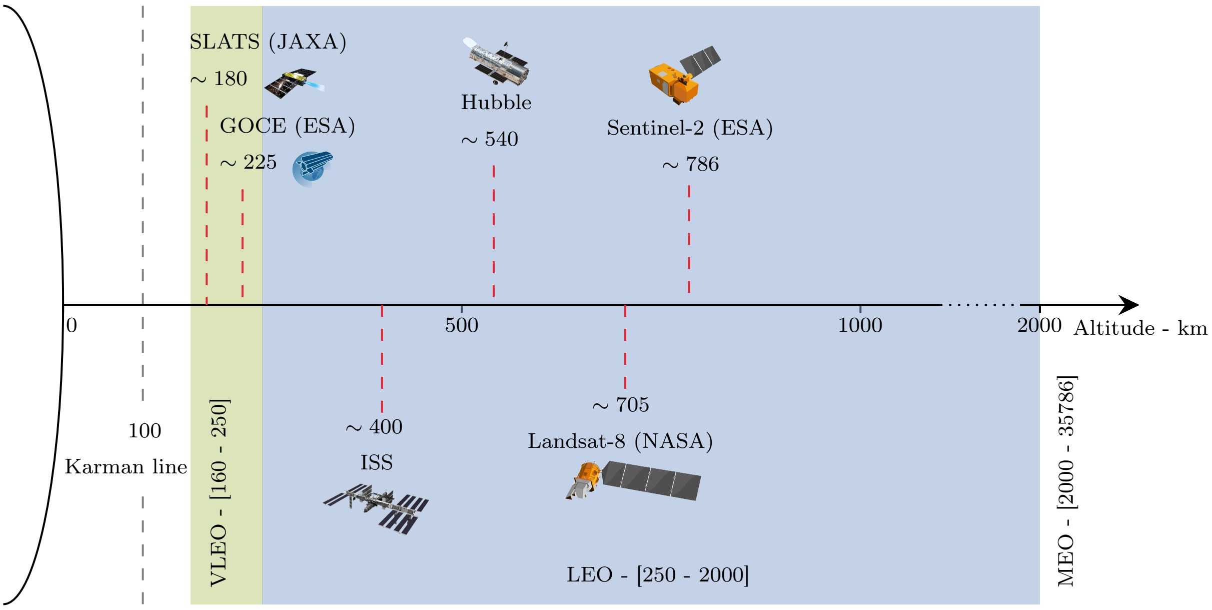

Figure 1.1: Altitude diagram of different Earth orbits and notable satellites.

altitudes using an electric propulsion system to counteract drag [10].

At VLEO altitudes, the flow around a spacecraft is a rarefied high-speed flow. The relative velocity between the satellite and the ambient gas is of the order of 7–8 km/s (∼orbital speeds). The atmosphere is extremely thin, but it still contains a high percentage of atomic oxygen which is a reactive species. This can lead to surface degradation and contamination. These conditions are responsible for limiting a mission's lifetime for two reasons: the drag forces, and interactions between the impinging particles and spacecraft materials that deteriorates the spacecraft.

Operating at very low altitude can provide multiple mission-level benefits:

- Improved spatial resolution for Earth observation instruments, since the ground sampling distance generally improves when the platform is closer to the surface.
- Higher received signal levels (or reduced transmission power) for communication links due to shorter propagation distance.
- Lower latency and potentially faster revisit times for certain constellations and observation concepts.
- Passive end-of-life disposal potential, since atmospheric drag can naturally de-orbit a spacecraft more quickly than from regular LEO.
- Potential increased maneuverability of platform to evade space surveillance.

Despite these advantages, only a small number of missions have operated in VLEO for extended periods. As a matter of fact, there are, as of January 2026, no long duration missions operating fully in the VLEO altitudes (at least not from public space agencies).

The reason VLEO remains challenging is that the residual atmosphere is no longer a small perturbation. Here is a summary of the challenges to overcome in VLEO:

- Relatively strong aerodynamic drag: without compensation, the orbit decays rapidly. Continuous thrust is required.
- Material degradation: atomic oxygen interactions can erode materials and modify surface properties, leading to failures and/or increased drag.
- System constraints: drag compensation consumes power and propellant (or requires alternative concepts), while thermal and contamination constraints can become more severe at low altitude, requiring innovative (but expensive) solutions.

These difficulties motivate the search for technologies that can maintain an orbit without carrying large onboard propellant masses. One of the most promising concepts in this direction is Air-Breathing Electric Propulsion (ABEP).

1.1.1 Air-Breathing Electric Propulsion

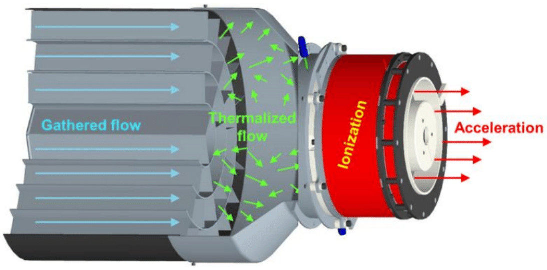

Figure 1.2: Illustration of the RAM-EP Assembly. From Andreussi et al. [1] (fig. 1).

ABEP combines an air intake with an electric thruster. Instead of storing fuel in a propellant tank, the system collects residual atmospheric particles, compresses (or guides) them into a discharge chamber, ionizes them, and accelerates the ions to generate thrust. In an ideal configuration, the intake continuously supplies the thruster with ambient gas, and the produced thrust compensates the atmospheric drag. Figure 1.2 shows a representative architecture of this concept from a study by Andreussi et al. [1].

ABEP has become an active research topic, with efforts focusing on intake design in rarefied hypersonic conditions, efficient ionization of atmospheric species, and stable operation at very low inlet pressures. A well-known industrial effort is the RAM-EP concept developed at SITAEL, which has contributed to the maturation of ABEP-related technologies and system architectures [1]. In parallel, research institutes have been developing dedicated ground-test methodologies and facilities to evaluate both intakes and thrusters in representative flow conditions.

Because in-orbit testing is expensive and slow, ground facilities that reproduce (as closely as possible) the VLEO particle environment are essential. Such facilities enable controlled parametric studies, diagnostic development, and material exposure tests, which are all required before proposing robust mission designs.

Within this global research effort, the von Karman Institute has developed a dedicated experimental facility to study ABEP intake designs and material degradation under VLEO-representative conditions. This facility is called DRAG-ON, and it is the experimental platform used throughout the present work.

1.2 The DRAG-ON facility

DRAG-ON is a ground-test facility designed to reproduce, in a controlled laboratory setting, the VLEO conditions. The facility has been developed and commissioned at VKI in the context of research programs targeting drag compensation and ABEP-related testing. Its design philosophy is to generate a directed beam of particles representative of the orbital conditions and to expose test articles (such as intake models or material samples) to such conditions.

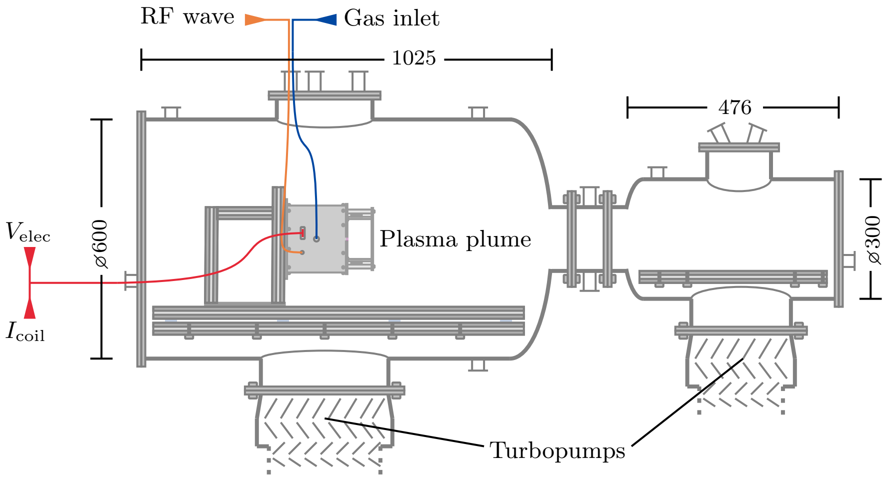

Figure 1.3: Schematic of the DRAG-ON facility. Dimensions in mm. The plasma source inputs are highlighted.

Figure 1.3 provides a reference schematic of the facility. DRAG-ON is composed of two main vacuum chambers connected by a tunnel-like section. The largest chamber hosts the particle flow generator (PFG) and any test article required by a test campaign. The tube-like section is designed to accommodate ABEP intakes design. Finally, the smaller chamber can also accommodate any test articles relevant to a test campaign and most importantly it allows the study of ABEP intakes by isolating the upstream and downstream conditions to infer transmission probabilities. The facility relies on high-vacuum pumping to reach low background pressures and to maintain stable operating conditions while injecting gas into the plasma source.

In simplified terms, here is the working principle of DRAG-ON. Gas is injected into the Particle Flow Generator (PFG), partially ionized in a plasma discharge (ICP), accelerated to hyperthermal energies, and extracted as a directed plume. This particle beam then reaches a test reaches a specific test article and/or diagnostic instrument. During operation, a strong vacuum is pulled through a specifically designed pumping system composed of two roughing pumps and two turbopumps.

The choice of an inductively coupled plasma particle flow generator was guided by factors such as, but not limited to, ease on operation, performance and cost. However, a central limitation is that the generated plume is composed of high energy ions, whereas the VLEO environment is composed of neutral particles. This greatly impacts the representativeness of the facility. For this reason, transforming this flow of fast ions into a flow of fast neutrals is imperative to render DRAG-ON truly representative of orbital conditions. The neutralization of the current ionic flow is the subject of this work.

1.2.1 Particle flow generator

The particle flow generator (PFG) is the element responsible for producing the hyperthermal particle flow. In DRAG-ON, the PFG model is the ThrustMe LTA-100 source, which is an inductively coupled plasma device that includes an electrostatic acceleration stage and magnetic beam-shaping lens.

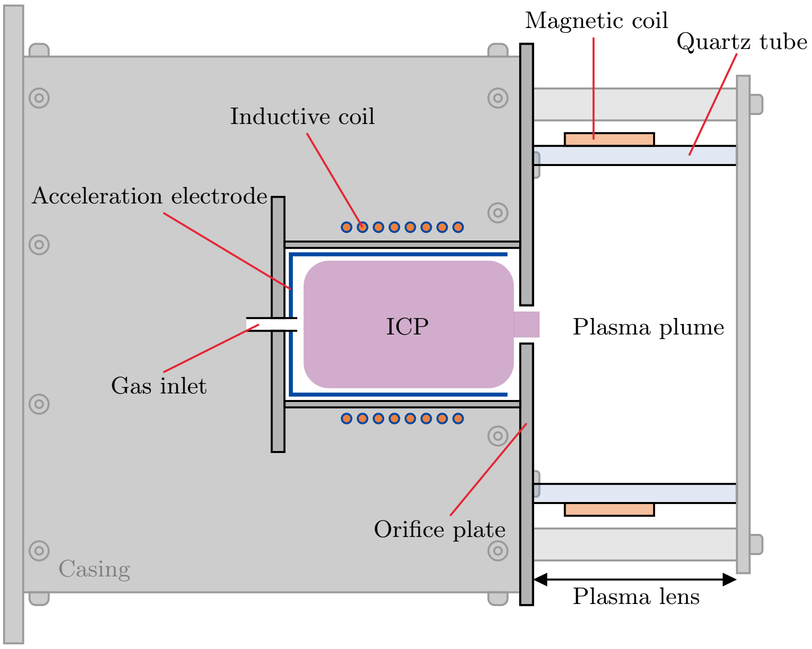

Figure 1.4: Schematic of the LTA-100 particle flow generator. Adapted from Rafalskyi and Dudin [2].

Figure 1.4 illustrates the main functional blocks of the LTA-100 (the drawing is for understanding and not a to-scale representation). A radio-frequency (RF) signal is generated and amplified to power an inductive coil, which sustains an inductively coupled plasma from the injected gas. Charged species are then accelerated through an electrostatic potential difference (tuned by the electrode voltage), producing a directed ion population.

Downstream of the acceleration region, a so-called magnetic lens is used to shape and collimate the plume, taking advantage of the fact that charged particles are sensitive to electromagnetic fields. The reader is invited to refer to Rafalskyi and Dudin [2] for further technical detail on the source design and operating envelope.

There are a number of tunable parameters available that allow an experimenter to reach desired flow conditions. In the experiments conducted in the context of this work, the PFG settings are mainly controlled through:

- Gas flow rate $\dot{m}$: typically between ~ 3 and ~ 13 sccm (standard cubic centimeters per minute).
- Electrode voltage V_{elec}: the negative bias from 0 down to roughly -50 V applied to the acceleration electrodes in the source.
- Magnetic lens coil current I_{coil}: typically up to about 2 A, which affects plume collimation and focusing.
- RF amplifier power P: it is the power absorbed by the source, typically between ~ 50 and ~ 80 W. Reflected power is sometimes mentioned in this work, it is strictly limited to 10 W for safety reasons.

These control parameters are essential later in this thesis, since neutralization performance and plume characteristics depend strongly on plume conditions.

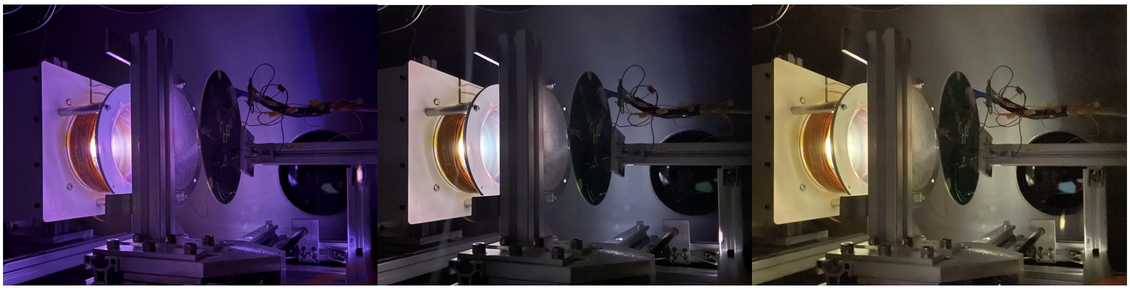

(a) 10 sccm Ar. (b) 10 sccm O_2, 3 sccm Ar. (c) 10 sccm O_2

Figure 1.5: Pictures of the PFG operating on different gas mixtures and flow rates during a test further described in Section 5.3

The PFG can operate on both argon and oxygen, as well as mixtures of the two. Figure 1.5 shows photographs of the discharge under different operating conditions during an experimental campaign described in Section 5.3. The color changes are expected and mainly reflect differences in the excited species and emission lines: a light purple discharge is typical for argon (Figure 1.5a), a more yellowish emission is observed for oxygen (Figure 1.5c), and mixed conditions produce intermediate colors, here close to white for 3 sccm of Argon and 10 sccm of Oxygen (Figure 1.5b). While these images are not used as quantitative diagnostics, they provide an intuitive view of the different reachable conditions.

1.2.2 Diagnostics

The facility is operated through a centralized control interface that monitors the main subsystems (pumps, valves, sensors) and records key quantities such as chamber pressures. Pressures are measured in both chambers using appropriate gauges (e.g. Pirani/cold cathode for a wide range and hot cathode gauges for finer measurement at low pressure when required). Temperatures can also be monitored with thermocouples installed through feedthroughs when required.

In addition to facility monitoring, DRAG-ON is equipped with a suite of electrostatic diagnostics dedicated to plume characterization (ion flux, ion energy distribution, etc.). These diagnostics are an important part of this thesis, they are therefore introduced and explained in detail in the dedicated Chapter 3.

1.2.3 Previous research

The extent of DRAG-ON capabilities today is the result of a long-term effort involving multiple researchers and students. Several works have progressively improved the facility, developed diagnostic methodologies, and established test protocols relevant to ABEP and VLEO. Most notably, Jorge [8] studied gas–plasma interactions with a strong experimental focus on DRAG-ON for his PhD thesis. Parodi [11] contributed to the numerical understanding of flow conditions and collision probabilities through simulation-oriented work in the context of his PhD thesis as well. These two references constitute the main contributions to DRAG-ON to this day.

It is also worth mentioning the contributions of master's student such as Brabants [12] (intake testing methodology), Fontaine [13] (optical emission spectroscopy implementation), and Pascoli [14] (first steps toward flow neutralization). This is a non-exhaustive list, but it helps position the present work within the continuous development of DRAG-ON.

1.3 Context and references

A complete literature review covering VLEO missions, ABEP technologies, plasma sources, diagnostics, and atomic oxygen facilities would be disproportionate for this introduction chapter. Instead, the state of the art is integrated where it is directly needed in dedicated sections. This approach ensures that each reference is introduced together with the assumptions and limitations that matter for the corresponding analysis. For the interested reader, an extensive state of the art is presented by Jorge [8] covering existing molecular beam-scattering experiments, material exposure facilities, in orbit tests and integral quantity measurements.

In the context of this work, the reviewed literature mainly focuses on neutral diagnostic and ion beam neutralization methods. In particular:

- Chapter 3 reviews the diagnostic methods relevant to DRAG-ON and to plume characterization in rarefied plasma facilities.
- Chapter 4 reviews the main ion neutralization strategies compatible with DRAG-ON constraints and motivates the selection of the perforated-plate approach investigated in this thesis.

1.4 Objectives & methodology

VLEO offers major potential benefits for Earth observation and other missions, but it also introduces drag and material-environment challenges. Ground-test facilities are therefore essential to study future technologies in a controlled environment. DRAG-ON was developed to reproduce key aspects of the VLEO particle environment, but the current plume generated by the PFG composed of energetic ions instead of neutrals limits representativeness for most applications.

The goal of this master thesis is to improve the representativeness of DRAG-ON by neutralizing the flow, *i.e.* by generating a fast neutral flux from a fast charged-particle plume while preserving, as much as possible, the useful properties of the beam for intake and material testing.

More practically, this thesis aims at selecting a neutralization strategy compatible with DRAG-ON constraints and at experimentally assessing its performance. The work follows a step-by-step methodology:

- Chapter 2 presents the basic theoretical concepts needed to understand this work.
- Chapter 3 presents the different diagnostic methods used throughout this work in order to understand later results.
- Chapter 4 discusses neutralization strategies and argues for the selection of a custom perforated plate neutralizer.
- Chapter 5 presents the experimental campaigns performed in the context of this work. The experimental methodology is structured as follows:
  - Section 5.2 defines practical metrics to quantify neutralization performance and plume quality.
  - Section 5.3 and Section 5.4 explore the selected neutralization concept through successive experimental campaigns.
  - Finally, Section 5.5 presents the design and results of a novel approach aiming at indirectly measuring a neutral flux.

The remainder of this manuscript follows this structure and progressively builds from theoretical concepts and diagnostic principles toward the experimental validation of the chosen neutralization approach.

Chapter 2

Theoretical framework

This chapter gathers the set of theoretical reminders required to interpret the experiments presented in this work. The DRAG-ON facility operates in a low-density regime where the continuum approximation breaks down. In addition, the flow generated by the particle flow generator is partially ionized, meaning that electrostatic effects (sheaths, quasi-neutrality) and ion-neutral / ion-wall interactions must be considered.

The objective here is not to provide an exhaustive review of rarefied gas dynamics and plasma physics, but rather to define the key quantities and mechanisms that will be referred to throughout the remainder of the report. In particular, this chapter introduces the notions of rarefaction and kinetic description, the basic plasma parameters relevant for probe diagnostics and ion acceleration, and the interaction mechanisms that enable beam neutralization, namely charge-exchange and surface neutralization.

2.1 Fundamentals of rarefied gas and plasma dynamics

The DRAG-ON facility operates a plasma beam source in a rarefied environment. This means that both the theoretical aspects of rarefied flows and plasma physics have to be reviewed in order to better understand the present work. This section will only skim the surface of these subject since going deeper in the theory is outside of the scope of this work.

2.1.1 Rarefied flow regimes

In kinetic theory, the *mean free path* λ is defined as the average distance traveled by a particle between successive collisions. It can be expressed as the ratio of the thermal speed c' to the mean collision frequency ν [3]:

$$\lambda = \frac{c'}{\nu} = \left[n \, \frac{\overline{\sigma_T c_r}}{\overline{c'}} \right]^{-1}, \tag{2.1}$$

where n is the number density, σ_T the total collision cross-section, and c_r the relative speed between molecules. For a gas of identical particles modeled as hard-spheres with a

Maxwell-Boltzmann velocity distribution, this simplifies to

$$\lambda = \frac{1}{\sqrt{2}\, n\, \pi d^2}, \tag{2.2}$$

where d is the particle diameter and the factor $\sqrt{2}$ comes from the statistical relation $\overline{c_r} = \sqrt{2}\, \overline{c'}$ between the mean relative and mean thermal speeds. These assumptions are further discussed in Section 2.1.2.

The Knudsen number Kn is a dimensionless value that describes the degree of rarefaction of a gas. It is defined as the ratio of the mean free path λ to the characteristic dimension L,

$$Kn = \frac{\lambda}{L}. \tag{2.3}$$

It is generally assumed that, for a flow with a Knudsen number $Kn < 0.1$, the Navier-Stokes equations are valid [3]. However, this definition can be imprecise since it depends on the definition of the characteristic length L. An overall dimension L that aims to describe the whole flow might result in a Knudsen number not representative of smaller flow features. The solution here is to define a local characteristic length L dependent on the length scale of macroscopic gradients,

$$L = \frac{\rho}{d\rho/dx}. \tag{2.4}$$

A local Knudsen number $Kn > 0.2$ will lead to large discrepancies in the Navier-Stokes equations results, it is therefore assumed to be the limit at which the continuum model has to be replaced by the molecular model. When approaching $Kn = 0$, the flow is considered inviscid and the Navier-Stokes equations reduce to the inviscid Euler formulation. On the opposite side of the scale the flow is considered collisionless, also known as the free-molecular regime. Figure 2.1 shows a schematic representation of the dependence of the conventional mathematical formulations limits to the Knudsen number.

In the free-molecular regime, intermolecular collisions are negligible and particles travel on ballistic trajectories between surface interactions. As a result, the exchange of mass, momentum, and energy occurs primarily at boundaries, and the details of gas-surface interaction models become essential. In this limit, the molecular flux crossing a unit area in an equilibrium gas is given by

$$\Gamma = \frac{1}{4} n \bar{c}, \tag{2.5}$$

where $\bar{c}$ is the mean molecular speed. In practical DRAG-ON configurations, particles often propagate through apertures, tubes, or perforated plates, where the transmitted flux is reduced by multiple wall collisions. This effect is commonly described through a transmission probability (often referred to as the Clausing factor) which depends primarily on the geometric aspect ratio L/D of the passage. This concept is directly relevant for perforated-plate neutralization, where the hole geometry controls both the probability of wall interaction and the downstream angular redistribution of the beam.

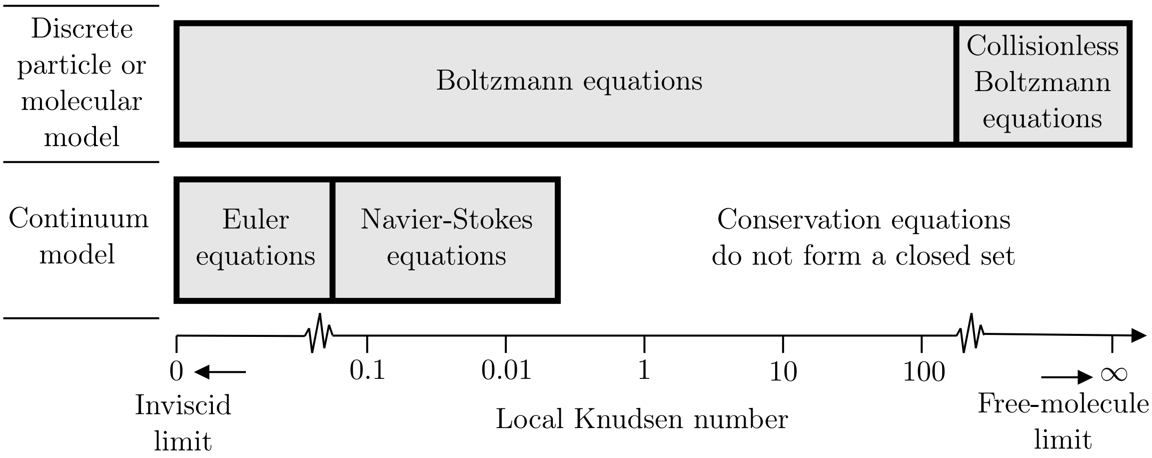

Figure 2.1: The Knudsen number limits on conventional mathematical models. Directly adapted from Bird [3] (Fig.1.1).

2.1.2 Kinetic theory in free-molecular flow regime

The free-molecular flow regime is modeled through the Boltzmann equation and a velocity distribution function. Factors such as collision frequency, mean free path and cross sections of the particles are important aspects of kinetic theory as well.

The distribution function $f(\mathbf{x}, \mathbf{v}, t)$ gives the number of particles located near position $\mathbf{x}$ with velocity $\mathbf{v}$ at time t. Its evolution is governed by the Boltzmann equation,

$$\frac{\partial f}{\partial t} + \mathbf{v} \cdot \nabla_{\mathbf{x}} f + \frac{\mathbf{F}}{m} \cdot \nabla_{\mathbf{v}} f = \left(\frac{\partial f}{\partial t} \right)_{\text{coll}}, \tag{2.6}$$

where the right-hand side represents the effect of binary collisions on the distribution. Macroscopic quantities such as number density, bulk velocity, and temperature are recovered as velocity moments of f. In the collisionless limit, the collision term becomes negligible and particle trajectories are governed only by external forces and boundary interactions [3]. This provides the theoretical basis for ballistic modelling approaches that are applicable in the facility.

The mean collision frequency for a particle in a dilute gas can be written in the form $\nu \sim n\sigma v_{\text{rel}}$, where σ is an effective collision cross section and v_{rel} is a relative speed. The cross section quantifies the probability of interaction between two particles and generally depends on the relative velocity and on the colliding species. In DSMC-type methods, simplified collision models are commonly used to reproduce correct transport properties while remaining computationally tractable. The Variable Hard Sphere (VHS) and Variable Soft Sphere (VSS) models proposed by Bird [3] are widely adopted for this purpose. For ionized air mixtures, dedicated parameter sets are required to obtain consistent transport properties over a wide temperature range [15].

2.1.3 Basics of plasma physics

A plasma is a partially ionized gas composed of electrons, ions and neutrals, whose charged particles collectively respond to electromagnetic fields. A useful measure of how ionized the gas is the degree of ionization, which can be expressed as $\alpha = n_e/(n_n + n_i)$, where n_e, n_n, and n_i are the electron, neutral and ion densities respectively. In DRAG-ON, the generated plasma beam has an ionization degree in the order of ~ 5 to $\sim 40\%$ [16] depending on absorbed power, but the charged fraction is sufficient for electrostatic probe diagnostics and for surface charging effects to be significant. For a more complete introduction to plasma physics, the reader is referred to Chen [17] and Lieberman and Lichtenberg [18].

Local charge imbalances can exist over a characteristic screening length called the Debye length,

$$\lambda_D = \sqrt{\frac{\varepsilon_0 k_B T_e}{n_e e^2}}, \tag{2.7}$$

where T_e is the electron temperature. The associated electron plasma frequency,

$$\omega_p = \sqrt{\frac{n_e e^2}{\varepsilon_0 m_e}}, \tag{2.8}$$

represents the natural oscillation rate of electrons in response to small perturbations. In practice, λ_D provides a useful estimate of the spatial scale over which electrostatic probes perturb the plasma and over which sheaths develop near surfaces.

On scales larger than the Debye length, plasmas are approximately quasi-neutral, meaning that the ion and electron densities are close ($n_i \approx n_e$).

When a plasma is in contact with a material surface, the higher mobility of electrons causes the surface to charge negatively until an electrostatic potential barrier is established. This results in the formation of a sheath, a thin non-neutral region adjacent to the wall. The sheath potential drop repels electrons and accelerates ions toward the surface.

In the context of this work, sheath physics is important for two reasons. First, it influences the interpretation of electrostatic probe measurements (Faraday probes and MRFEA, see Chapter 3). Second, it sets the impact energy and incidence conditions of ions hitting a neutralizing surface (flat surface or perforated plate, see Chapter 4), which directly affects the neutralization mechanisms described in Section 2.2.2.

2.2 Ion-neutral and ion-wall interaction mechanisms

This section acts as the bridge between general theory and the neutralization phenomenon studied in this work. It introduces the concept of charge exchange neutralization, which is limited in free-molecular regimes but still relevant. It also presents the theoretical aspect of Ion-wall neutralization which is the main mechanism at play in a perforated plate neutralizer.

2.2.1 Charge EXchange collisions

Charge-EXchange (CEX) collisions are one of the dominant interaction mechanisms between a directed ion beam and a background neutral gas under rarefied conditions. In the DRAG-ON context, since the ionization of the working gas is not complete, the fast flow will encounter a mass of thermal gas. The purpose of this section is to introduce the basic physics and the standard kinetic expressions used to estimate CEX likelihood, without entering into species-specific cross-section fitting.

A charge-exchange collision is an interaction in which an ion captures an electron from a neutral target. In its simplest form,

$$\mathrm{A}^{+} + \mathrm{B} \rightarrow \mathrm{A} + \mathrm{B}^{+}, \tag{2.9}$$

the projectile ion A^{+} becomes a fast neutral A, while the neutral target B becomes an ion B^{+}. For resonant or near-resonant systems, the electron transfer can occur with only a limited momentum exchange, such that the newly created fast neutral approximately preserves the directed velocity of the incoming ion, whereas the newly created ion tends to follow the velocity distribution of the background gas. From a beam point of view, CEX therefore transfers a fraction of the directed ion flux into a fast-neutral component, and creates a population of slow ions that can be more easily influenced by local electric fields. This mechanism is a standard feature of rarefied plasma plumes in vacuum facilities, where background pressure and propagation distance control the importance of charge-exchange effects [3, 19].

The probability of CEX is governed by the collision cross section and by the relative speed between collision partners. In kinetic theory, binary collision rates are expressed using a velocity-dependent cross section $\sigma(g)$, where $g = \|\mathbf{v}_1 - \mathbf{v}_2\|$ is the relative speed [3]. This is the same framework used in particle-based rarefied-gas methods (DSMC/TPMC), where collisions are sampled based on g and on an effective interaction model. Bird [3] introduced practical collision models such as the Variable Hard Sphere (VHS) and Variable Soft Sphere (VSS) models to represent a total cross section (and associated transport properties) that varies with relative speed while remaining computationally efficient. For high-temperature and ionized air mixtures, the choice of collision model and parameters (often favoring VSS to improve transport consistency) has been discussed in detail in the DSMC literature [15].

In contrast, CEX is a specific inelastic process, and quantitative estimates generally require the use of process-specific cross sections taken from dedicated measurements or databases. Nevertheless, the key qualitative point remains that σ_{CEX} can vary significantly with collision energy, meaning that the CEX probability is not only a function of pressure and distance, but also of the ion energy (through g). For the present work, this section mainly provides the general dependence needed to interpret trends with operating pressure and propagation length.

Probability estimation along a trajectory

In a dilute background gas, binary collisions along a particle path can be modeled as a Poisson process. Under this assumption, the probability that a particle undergoes no CEX event over a travelled distance s is the so-called "survival" probability, written in exponential form from the corresponding collision (optical depth) integral [3, 20]. The probability of at least one CEX event is then one minus this survival probability.

A compact expression commonly used for the probability of at least one collision along a trajectory is

$$P_{\mathrm{CEX}} = 1 - \exp\left(- \int_0^{s_{\mathrm{end}}} n(s)\, \sigma_{\mathrm{CEX}}(g)\, ds \right), \tag{2.10}$$

where $n(s)$ is the neutral number density along the trajectory and $\sigma_{\mathrm{CEX}}(g)$ is the charge-exchange cross section evaluated at the local relative speed g (*i.e.* collision energy), which must be taken from appropriate cross-section models or tabulated data for quantitative estimates [15]. In the simplified case of uniform density and approximately constant cross section, this reduces to

$$P_{\mathrm{CEX}} \approx 1 - \exp(-n\, \sigma_{\mathrm{CEX}}\, s), \tag{2.11}$$

which directly highlights why CEX effects increase with background pressure (through n) and with propagation distance s. This type of reasoning is commonly used in vacuum-facility plume diagnostics to assess when charge-exchange can significantly modify measured ion profiles and integrated currents [19].

2.2.2 Ion-wall neutralization

When a positive ion approaches a conductive surface, it can be neutralized by capturing an electron from the solid. For low-energy ions (typically a few to a few tens of eV in the present work), the dominant channels are near-surface electron-transfer mechanisms rather than sputtering-related processes.

Two mechanisms are classically distinguished. In resonant (or quasi-resonant) charge transfer, an electron tunnels from an occupied electronic state of the surface into an available projectile state when their energies become close during the approach. This process is inherently distance-dependent and is often treated dynamically, since the electron-transfer probability depends on the approach time and level alignment [21]. In Auger neutralization, a conduction-band electron fills the projectile state while a second electron (or a collective excitation of the solid) carries away the excess energy, ensuring energy conservation during the neutralization [22].

In practice, both channels may coexist, and the resulting neutralization probability depends on the projectile species, the surface material (work function, electronic density of states), and the incidence conditions [23, 24]. For the present application, the important point is that ions impacting metallic walls inside a perforated plate can be neutralized with a high probability, producing fast neutrals that continue downstream but with modified energy and angle distributions.

The incidence conditions strongly affect what happens after neutralization. At low energy, ion-surface interactions are often inelastic: part of the directed kinetic energy is transferred to the lattice, and the outgoing neutrals have a lower mean energy and a broader distribution than the incoming ions [24]. These effects become more pronounced when the interaction is not a single, clean reflection but involves multiple contacts and/or rough surfaces.

The incidence angle also matters because it controls both how likely the ion is to undergo a grazing interaction and how many wall encounters occur before the particle exits a channel. Grazing interactions are commonly exploited in surface-neutralization-based neutral beam sources, where ions reflect from a surface while being neutralized, producing a directed neutral beam [7, 25]. In the DRAG-ON operating range (few-tens of eV), the objective is to promote neutralization while keeping a sufficiently directed transmitted flux.

2.2.3 Energy and angular redistribution after neutralization

Wall neutralization is generally accompanied by energy and momentum redistribution. A fraction of the incoming particle flux is lost by reflection upstream or by being captured on the walls, reducing the transmitted flux through the plate. For particles that do transmit, the outgoing neutrals typically retain only a fraction of the incoming directed energy due to inelastic energy loss at the surface and possible multiple collisions inside the channel [24]. This loss factor is usually estimated in the range of $[0.5, 0.7]$ [26]. In other words, even when neutralization is efficient, the transmitted beam may become slower and less directional.

From a practical standpoint, two limiting behaviors can be expected. If neutralization occurs with only one (or very few) grazing wall interactions, the outgoing neutrals can remain relatively directional, with moderate energy loss (this is the principle exploited in shallow-angle or reflected neutral beam devices) [7, 25]. If, instead, the geometry and sheath focusing drive ions into multiple sidewall encounters, the transmitted neutrals become more scattered: the angular distribution broadens and the mean energy decreases due to cumulative accommodation [27, 28].

This provides the qualitative link with perforated-plate design: increasing wall-interaction probability (via higher L/D or stronger sheath moulding) should increase apparent neutralization, but it can also reduce collimation and modify the effective delivered neutral flux on a downstream target.

Chapter 3

Plasma plume characterization and diagnostics

This chapter presents the diagnostic tools that are relevant to characterize the DRAG-ON particle beam and to quantify neutralization performance. Because the particle flow generator produces a partially ionized plume, most direct measurements rely on electrostatic diagnostics, which only interact with charged species. The Faraday probe array and the magnetized retarding field energy analyzer (MRFEA) are therefore the primary instruments used in this work to measure ion current density and ion energy distributions.

A key objective of this chapter is to explicitly connect what the probes measure (currents and I-V characteristics) to the underlying physical quantities of interest (ion flux, ion number density, mean ion energy, and energy spread). The second part of the chapter introduces complementary approaches for neutrals diagnostics, which are generally indirect and rely on material response (erosion) or momentum/force measurements. Finally, the chapter summarizes the work carried out on plume characterization in the context of this work.

3.1 Electrostatic diagnostic methods in DRAG-ON

The electrostatic measurements made in the context of this work were all taken with instruments present on a diagnostic plate designed by ThrustMe presented in Figure 3.1. This plate comports a multitude of electrostatic means of measurement; 9 planar Faraday probes, arranged in a "V" shape with the central probe being aligned with the center of the plate, a Retarding Field Energy Analyzer (RFEA), a Magnetized RFEA (MRFEA) and it can also be equipped with a Langmuir probe, although not present on the picture in Figure 3.1 since it was not installed during the experimental campaigns of this work.

This section will introduce each measurement method one by one. Since only the Faraday probes and MRFEA are used in the context of this work, the other electrostatic measurements method will be only briefly addressed. The DRAG-ON facility also owns an ExB probe that will also be presented here, however this probe is not yet in use in the facility.

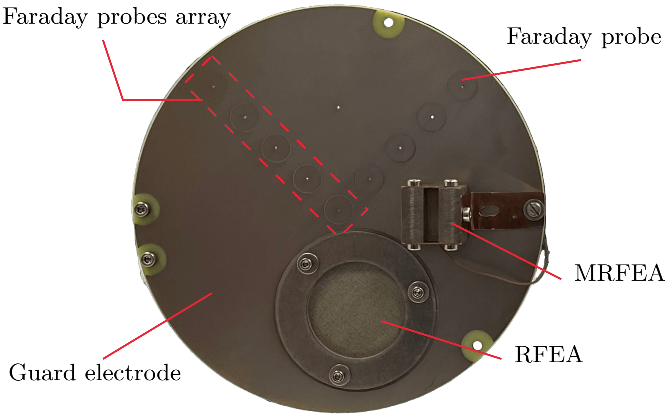

Figure 3.1: Diagnostic plate designed by ThrustMe and equipped with a retarding field energy analyzer (RFEA), a magnetized RFEA and 9 Faraday probes arranged in two normal arrays.

3.1.1 Faraday probes

A Faraday probe is an electrostatic diagnostic instrument used to determine the local ion charge flux in a plasma plume [4]. In practice, the probe does not directly output a flux: it outputs an electrical current drawn by a biased collector. The purpose of this section is to describe the simple operating principle of the probe (collector, guard electrode, biasing, readout), and to explain how the measured electrical signal is interpreted as an ion current density and an ion number flux.

Working principle and measured signal

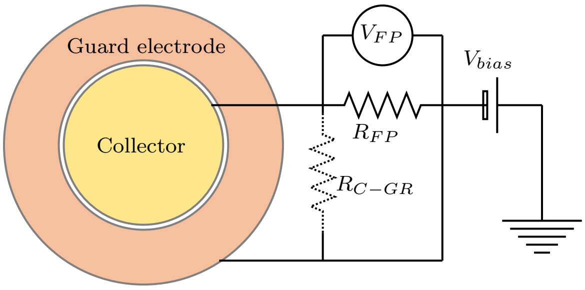

Figure 3.2: Electrical schematic of a typical Faraday probe. Directly adapted from Brown et al. [4] (fig. 9).

In its simplest form, the Faraday probe consists of a conductive collector electrode exposed to the plume [4]. When the collector is biased sufficiently negative with respect to the surrounding plasma, electrons are repelled and the collector operates in the ion saturation regime. Under this condition, positive ions reaching the collector are collected and produce a net current to the collector.

The practical readout follows the circuit shown in Figure 3.2. A bias supply sets the collector (and typically the guard electrode) at a fixed bias voltage V_{bias} with respect to facility ground. The collected current is measured using a shunt resistor R_{FP}: the measured voltage V_{FP} across this resistor gives

$$I_{\mathrm{FP}} = \frac{V_{\mathrm{FP}}}{R_{\mathrm{FP}}}. \tag{3.1}$$

In other words, the probe output is fundamentally the collector current I_{FP}, inferred from a voltage measurement [4]. It is also possible to sweep the bias voltage V_{bias} in order to study parameters such as the floating potential V_f.

From collector current to ion current density

For a probe operating in ion saturation, Brown et al. [4] expresses the ion current density (ion charge flux) j from the measured collector current as

$$j \;=\; \frac{I_{\mathrm{FP}}}{A_C}\,\frac{\kappa_G}{\kappa_{\mathrm{SEE}}}, \tag{3.2}$$

where A_C is the geometric collector area, κ_G is a correction accounting for ions collected in the collector/guard-ring gap, and κ_{SEE} is a correction accounting for secondary electron emission (SEE) at the collector. In other words, the raw ratio I_{FP}/A_C is the starting point, but the literature warns that geometric and surface effects can bias the apparent current density if they are ignored.

In the common case where the charge state distribution is not explicitly resolved, j should be understood as the local ion charge flux ($\mathrm{A\,m^{-2}}$). If multiple charge states are present, j corresponds to $j = \sum_k \Gamma_k Z_k e$, where Γ_k is the particle flux of species k with charge state Z_k [4]. In the present work, the dominant assumption is $Z = 1$ (singly charged ions), unless otherwise stated.

From ion current density to ion number flux and integrated current

Once the ion current density is obtained, the ion number flux follows directly. For a singly charged ion beam ($z = 1$),

$$\Gamma_i \;=\; \frac{j}{e}, \tag{3.3}$$

where e is the elementary charge. This is the key link between what the Faraday probe measures (an electrical current) and the physical quantity of interest (a particle flux).

Finally, Faraday probes are often used to reconstruct an integrated beam current by integrating the measured current density over a plane. For an axisymmetric plume measured as a radial profile $j(r)$ at fixed axial distance, the total ion beam current is

$$I_{i,\mathrm{tot}} \;=\; \int j\,dA \;=\; 2\pi \int_0^{r_{\max}} j(r)\,r\,dr, \tag{3.4}$$

where $r_{\max}$ corresponds to the measurement extent. This integral is evaluated numerically from the discrete probe positions in the post-processing. The same operation can be applied to $\Gamma_i(r)$ to obtain an ion particle flow rate.

3.1.2 Magnetized Retarding Field Energy Analyzer

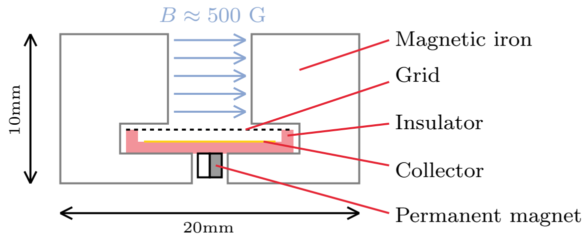

Figure 3.3: Schematic drawing of the MRFEA. Directly adapted from Rafalskyi et al. [5] (fig. 7a).

While a Faraday probe provides the local ion current density, it does not provide direct information on the ion kinetic energy. In DRAG-ON, the ion energy is a key quantity because it directly impacts the expected interaction with tested materials and the interpretation of neutralization mechanisms, where ion acceleration and energy loss may occur. For this reason, an energy analyzer is required in addition to flux diagnostics. The magnetized retarding field energy analyzer (MRFEA) used in this work is designed, with the diagnostic plate, by ThrustMe. It is described by Rafalskyi et al. [5].

Measured quantity

An MRFEA is an electrostatic energy analyzer: it does not measure energy directly, but measures a collector current while an electrostatic potential barrier is varied. The measured signal is therefore an electrical current I_c, and the ion energy distribution is obtained by interpreting how I_c changes when the retarding (rejecting) potential is increased. In other words, the instrument returns an I-V curve, and the physics comes from how this curve is converted into an energy distribution [5].

Link between current-voltage and energy threshold

The analyzer contains an entrance aperture an electrostatic retarding stage composed of a grid and a collector that measures the transmitted charged-particle current as presented Figure 3.3. In the configuration described by Rafalskyi et al. [5], the electrostatic stage is intentionally kept simple (single-grid retarding concept) to obtain a predictable ion transparency.

For a positive ion population of charge $q = ze$, increasing the retarding potential progressively blocks ions with insufficient kinetic energy along the analyzer axis. Therefore, the collector current $I_c(V)$ can be interpreted as a cumulative measurement: at a given retarding setting, only ions with an axial energy-per-charge above the barrier contribute to the current.

Extracting an ion velocity distribution function (IVDF)

Under the usual assumptions of collisionless transport inside the analyzer and a monotonic energy filter, the measured collector current can be viewed as an integral of the ion velocity distribution function (IVDF). This is why the IVDF is obtained by differentiating the measured *I*-*V* curve, a method explicitly used and discussed by Rafalskyi et al. [5]. Note that the terms IVDF and IEDF (ion energy distribution function) are sometimes jointly used; they represent the same metric. Ion energy and ion velocity represent the same value, in both cases measured in eV.

In practice (mono-charge ions), one uses the mapping between retarding voltage and an energy threshold,

$$E \simeq ze\,V_r, \tag{3.5}$$

and the IVDF is obtained from

$$f(E) \;\propto\; -\frac{dI_c}{dV_r}, \qquad \text{with} \qquad E \simeq zeV_r. \tag{3.6}$$

This point is important for interpretation: the MRFEA does not output “the energy”, it outputs a current curve. Any reported energy metric (most probable energy, mean energy, spread) is a post-processed quantity derived from $I_c(V_r)$, and the differentiation step naturally amplifies noise. The numerical processing is kept consistent across datasets, only using a first order Savitzky-Golay filter with a window size of 3.

It is also important to note that only the axial component of velocity is measured. This means that the MRFEA is not necessarily sensitive to the full kinetic energy when ions have a significant incidence angle. As a result, a broad angular distribution tends to broaden and shift the measured IVDF compared to a perfectly collimated beam. In the context of this work, this effect was not strong enough to be measured and used as a means of interpretation.

Importance of magnetization

A classical RFEA can suffer from electron contamination: electrons, co-extracted from the source, can contribute to the collector current and distort the interpretation of the *I*-*V* curve, especially when trying to isolate low ion currents. The MRFEA adds a magnetic electron barrier upstream of the electrostatic stage to strongly reduce electron transport into the analyzer. The idea is to magnetize electrons (small Larmor gyroradius) so they are lost to the channel sidewalls, while keeping ion trajectories only weakly affected. Rafalskyi et al. [5] summarizes this design logic with the practical requirement $r_{ce} \ll z_{MB} \ll r_{ci}$, ensuring electrons are filtered while ions still reach the retarding stage.

In their optimized configuration, meaning the rectangular magnetic barrier showed in Figure 3.3, Rafalskyi et al. [5] report electron suppression ratios reaching the order of 10^3-10^4 (up to ~ 6000 in their tests), while maintaining an ion energy resolution better than about 5 eV. These numbers give the right order of magnitude for what the instrument is designed to achieve: a mostly ion-dominated collector signal that can be safely differentiated to obtain an IVDF.

Physical quantities inferred from MRFEA signals

In this work, the MRFEA is used to extract:

- a most probable ion energy E_{mp},
- a mean ion energy $\overline{E}$,

All energies/velocities are reported in eV per charge (*i.e.* eV for $z = 1$), consistent with the retarding principle.

3.1.3 Retarding Field Energy Analyzer

As shown in Figure 3.1, there is also a RFEA present on the diagnostic plate. The whole working principle has been explained in the previous MRFEA section, the single difference being that the RFEA does not have the magnetic barrier intended to suppress electrons. This might be used as an advantage. It can, in principle, be used to measure an Electron Energy Distribution Function (EEDF). This gives interesting information about the state of the electron population in the particle flow.

Despite the availability of the instrument, it was not used in the context of this work. This research focused on ion behavior and approached diagnostics with this in mind. Furthermore, the instrument is not regularly used as part of usual facility operation.

In hindsight, taking EEDF measurements would have been a positive addition to the current diagnostic suite. The interest in studying electron energy and density only became evident after reviewing experimental results presented in Section 5.5. For future work, the addition of RFEA measurement in the regular operation routine might be interesting.

3.1.4 ExB probe

An ExB probe (also referred to as a Wien filter) is a velocity filter that can separate ions according to their energy E, mass m, and charge state z [19]. The probe is intended to be placed downstream of an ion or plasma source, where it samples the plume. Its working principle relies on crossed electric and magnetic fields: a magnetic field is applied normal to the axis of an electric field, so that only ions with a specific velocity can pass through the filter without being deflected.

In the ideal Wien-filter condition, the electric force and magnetic force cancel each other,

$$ze\,E = ze\,vB, \tag{3.7}$$

so the transmitted ions satisfy

$$v = \frac{E}{B}. \tag{3.8}$$

When the filter setting is swept (typically by changing E while keeping B fixed), the probe output current can be interpreted as a distribution of ion current versus selected velocity. By linking the selected velocity to the ion kinetic energy $E_k = \frac{1}{2}mv^2$ (for a given m and z), peaks in the signal can be associated with different ion species and/or charge states. In other words, the ExB probe does not directly measure "mass" or "energy"; it measures a collector current while selecting ions by velocity, and the species interpretation follows from the physics of the filter and from additional assumptions or complementary diagnostics [19].

An ExB probe designed by Plasma Controls LLC [29], is currently available at VKI, but it was not used in the present work because the operating procedure and calibration workflow still require further work. Nevertheless, it is a promising diagnostic for future DRAG-ON campaigns: it would allow the composition of the beam (species fractions and possible charge states) to be assessed, whereas the current interpretation of the flow composition still relies on assumptions and indirect reasoning.

3.2 Neutrals diagnostic

By definition, neutrals do not respond to electric/magnetic fields, so electrostatic probes cannot measure them directly. Therefore there is a need to come up with neutral diagnostics in order to fully characterize the flow once neutralized. Neutral diagnostics typically rely on material response (erosion) or momentum/force transfer.

3.2.1 Polyimide degradation measurement

In VLEO-representative facilities, one common way to quantify a *neutral* atomic-oxygen flux is to measure how fast a calibrated polymer erodes. The idea is simple: if the erosion yield of a given polyimide is known (removed volume per incoming atom), then measuring the removed mass (or thickness) gives the fluence, and dividing by time gives the flux. Hisamoto et al. [26] use this approach as their primary AO flux diagnostic, based on polyimide-coated quartz crystal microbalances (QCMs). Note that the name polyimide is just another appellation for Kapton.

Principle of the QCM approach

QCM stands for Quartz-Cristal Microbalance. It is a piezoelectric quartz resonator whose resonance frequency shifts when its mass changes. By coating the crystal with a thin polyimide film, the erosion of the film under AO exposure produces a measurable frequency increase (mass loss). Hisamoto et al. convert the measured frequency change Δf into an eroded mass Δm using a standard QCM relation they define more in detail in their paper.

Once the eroded mass is known, the corresponding removed polyimide volume follows from the polyimide density. Hisamoto et al. [26] then infer the AO fluence F by dividing the eroded volume by an assumed erosion yield and by the exposed area. Finally the AO flux Φ is obtained as $\Phi = F/t$.

Relation with the present work

There is no polyimide-coated QCMs available in DRAG-ON/VKI, so the exact implementation of Hisamoto is not reproducible here. However, the concept is directly relevant: polyimide erosion provides an integrated measurement of neutral exposure that is complementary to electrostatic probes, which only see charged particles. In Section 5.5, polyimide degradation is used as a neutral-sensitive indicator, but with a different experimental workflow.

3.2.2 Pendulum-based force probe

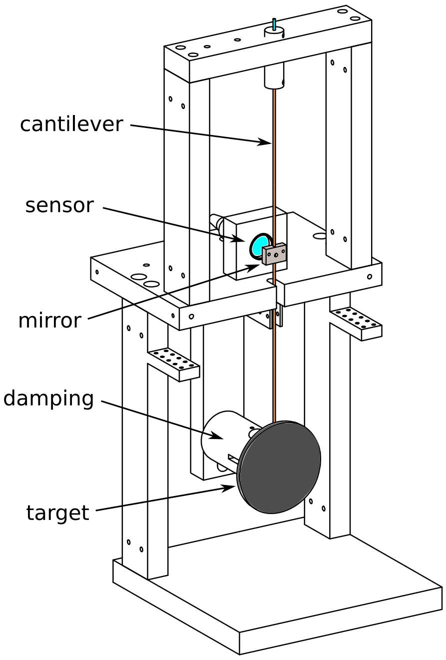

Figure 3.4: One-axis force probe as an indirect thrust balance (without housing). From Spethmann et al. [6] (fig. 2b).

A force probe measures the mechanical push of the plume instead of an electrical signal. A small target plate is placed in the flow; ions and neutrals hit it and transfer momentum, which creates a tiny force on the plate. This force bends a calibrated flexure (or cantilever), and the deflection is measured with an optical displacement sensor (see Figure 3.4). After calibration, the measured deflection is converted into force, and this force is directly linked to the local momentum flux of the plume [30].

In the context of this work, it would have been convenient because it is sensitive to both ions and neutrals. Faraday probes and MRFEA only tell us about the charged fraction, while the whole point of neutralization is to increase the neutral flux. A force probe could therefore provide an independent check of whether the neutralized flow still carries the expected momentum and how it is distributed across the plume. With the addition of current ion-based metrics, it is possible to infer a neutral only flux.

The integration of a force probe in DRAG-ON is planned for early 2026 by Charlotte Borbouse, a student enrolled in the research master program of VKI. This work will be realized, in part, in collaboration with a team from Kiel university, Germany, that developed a pendulum-based force probe for low-thrust applications [6]. An illustration of such a device is presented in Figure 3.4.

3.3 Plume angular distribution characterization

This section presents a method developed in the context of the present work that aims at computing, from experimental data, the relative angle at which an average ion intersects a reference plane. This plane representing the location where a perforated plate neutralizer would be installed, for example. In order to infer the relative angle at a certain plane, this method rebuilds the average trajectory of the flow from multiple ion current density profiles measured at different axial distances from the source. It's important to note that the results presented in this section will not be used to interpret results in this work. The method is deemed to be insufficiently developed and validated to support any robust interpretation at this stage. It is nevertheless presented here as the approach itself and the observed results seem credible. It could benefit from future work, with a more adapted measurement technique, to become a useful mean of analysis.

This method is partly adapted from plasma plumes characterization methods presented by Brown et al. [4]. In this paper, he presents recommended practices when using Faraday probes in the case of electric propulsion testing. The LTA-100 plasma source being derived from ion thrusters technology, it makes sense to use this as a reference. This measurement method, following Brown's definitions, takes place in the near field if the source exit plane is considered to be at the end of the magnetic plasma lens. However the main difference in this case is the measurement method. Brown recommends that the radial range of a measurement profile "should extend to the location where measured ion current density is less than 0.2% of the maximum current density along the radial profile at fixed Z". With the current measurement methods available in DRAG-ON, it is not possible to follow this recommendation, this is where the method presented here starts to differ from the ideal case.

This method will be referred to as the cumulative current approach. Rather than reconstructing individual particle trajectories, this approach relies on flux conservation and on the cumulative contribution of all emitted ions to each measurement location. At several axial locations, the Faraday probes arrays present on the diagnostic plate (see Figure 3.1) measure an ion current density profile from $r = 0$ to $r = 6.4\,\mathrm{cm}$. This method assumes the plasma flow to be axisymmetric around the $z - axis$.

This test is based on a set of measurement made with a flow rate $\dot{m} = 3\,\mathrm{sccm}$ of pure

Argon, an electrode voltage $V_{\text{elec}} = -40V$, an absorbed power $P = 70\,\text{W}$ and variable coil current $I_{\text{coil}} \in \{0,\ 0.5,\ 1,\ 1.5,\ 2\}\,\text{A}$.

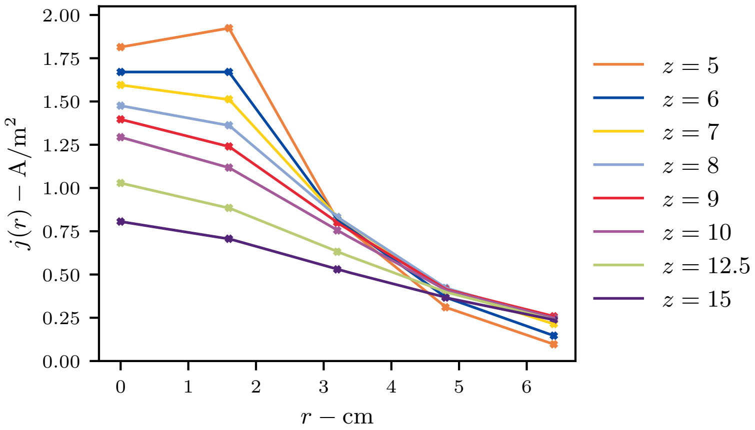

Figure 3.5: Ion current density profiles at different axial distances for $I_{\text{coil}} = 2\,\text{A}$.

Figure 3.5 presents these ion current density profiles at different axial distances $z = \{5,\ 6,\ 7,\ 8,\ 9,\ 10,\ 12.5,\ 15\}$ cm, considering $z = 0$ as the exit plane of the plasma source (the end of the quartz tube). These measurement where possible by mounting the linear stage axially in the facility (see Section 5.1.2). The goal of this technique being an estimation of the relative angle of ions at the $z = 5\,\text{cm}$ plane, it will be referred to as the base plane.

Each of those measurement planes are discretized and cumulative current profile $I(r)$ is defined as

$$I(r) = 2\pi \int_0^r r'\, j(r')\, \mathrm{d}r', \tag{3.9}$$

which is implemented numerically by a trapezoidal cumulative integration of $2\pi r j(r)$. Since $I(r)$ is monotone by construction in the ideal case, it can be inverted to obtain a radius as a function of cumulative current, *i.e.* $r(C)$ where C denotes an enclosed-current level. In practice, slight non-monotonicities due to measurement noise are removed by enforcing strict monotonic increase before inversion, and the inverse mapping is obtained by linear interpolation.

The key step of the method is to use the cumulative level C that identifies a given fraction of the total beam current. For each plane, we compute $r(C)$ on a common grid of C values. Because the total collected current can differ from one plane to another (finite plate radius and potential beam spreading beyond the probe reach), the method distinguishes between: (i) a “common” cumulative range $C \in [0, C_{\text{cap}}]$ that is present on all planes, and (ii) an extended range up to $C_{\max}$ that may be missing on the most downstream planes. Numerically, for each plane p we define $C_{\max,p} = I_p(r_{\max})$ and build a global grid $C \in [0, C_{\max}]$ with $C_{\max} = \max_p C_{\max,p}$, while setting $r(C) = \text{NaN}$ whenever $C > C_{\max,p}$ for a given plane. The common cap is then

$$C_{\text{cap}} \;=\; \min_p C_{\max,p}, \tag{3.10}$$

which corresponds to the maximum enclosed current that is guaranteed to be captured at all planes. In practice, only values contained in the common cap C_{cap} are used for best representation.

This cumulative-current representation transforms the experimental dataset from a set of profiles $j_p(r)$ into a set of current contours $r_p(C)$, where each fixed value of C defines an array of points describing how the radius enclosing the same fraction of beam current evolves with axial distance. Finally those array of points are fitted to a curve to form a streamline-like curve that represents a line of constant cumulative current. There is now a discussion to have on the type of fitting required to best describe the physical reality of this measurement.

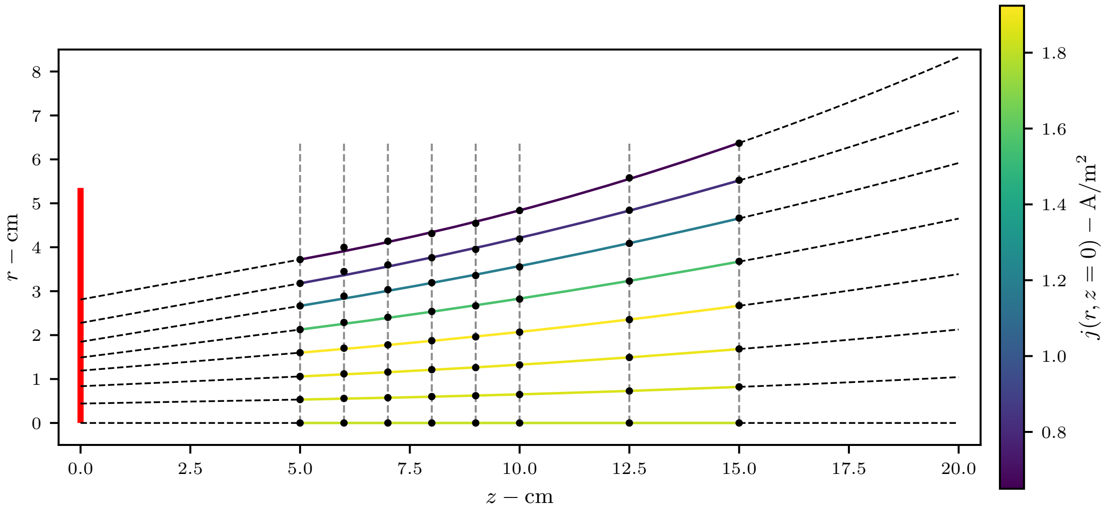

Figure 3.6: Representation of the streamline-like curves with a quadratic fit for $I_{\text{coil}} = 2\,\text{A}$. The ion current density value is taken on the base plane $z = 5\,\text{cm}$. The vertical red line represents the exit plane of the PFG. The vertical dashed black lines represent the measured area.

In Figure 3.6, the fitting between points was done using a quadratic regression. Here only a small sample of rays are showcased, the actual discretization of the domain is much finer. The rays color represent the ion current density at $z = 5\,\text{cm}$. It is good representation of the ion density in the flow. Even though is not physically ion trajectories, these curves are a good representation of the flow's behavior.

Assuming these curves are a fair representation of average ion trajectory, it is possible to infer an effective propagation direction by computing the angle at the start of each curve relative to the axial direction. The local propagation angle associated with the contour is defined from the slope at the reference plane. Figure 3.7 presents the angle relative to the axial direction as a function of radial position at the base plane for different values of focusing coil current. Here, two different fit are presented, a simple linear fit (Figure 3.7a) and a quadratic fit (Figure 3.7b). The resulting difference in angle is quite large. This is a reason why this method should be further developed to be used as a tool in plume

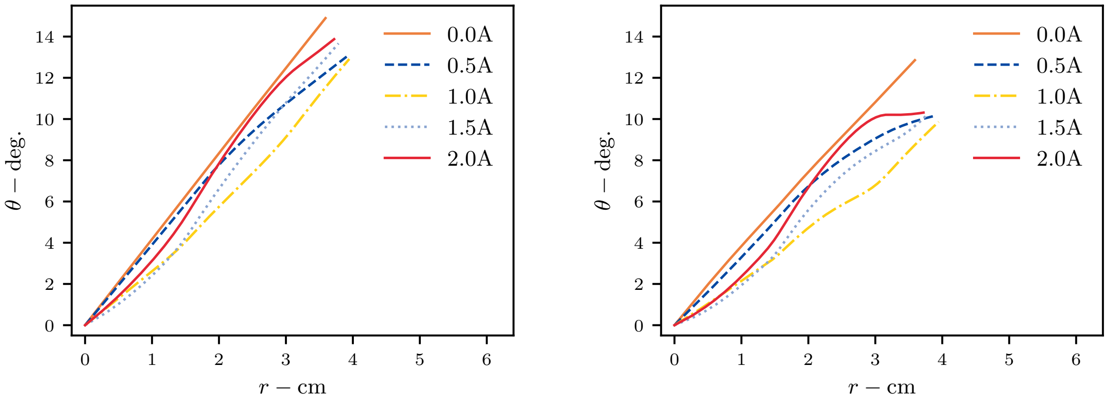

(a) Linear fit.

(b) Quadratic fit.

Figure 3.7: Computed angle distribution at $z = 5\,\mathrm{cm}$ for a linear and a quadratic fit.

diagnostic. A further improvement would be the addition of a second degree of freedom on the linear stage to refine and enlarge the measured region.

Chapter 4

Ion neutralization method selection

This chapter reviews the main ion neutralization strategies that were considered to obtain a VLEO-representative flow in DRAG-ON. The goal here is not to provide an exhaustive review of all neutralizer technologies developed for electric propulsion, but rather to compare the approaches that are practically compatible with DRAG-ON constraints. Each method is introduced with its working principle, advantages, and limitations. The chapter then justifies the selection of the perforated plate approach that is studied experimentally in the remainder of the present work.

The neutralization method selection is based on a few selection criteria, namely the expected neutralization efficiency, the preservation of beam collimation and general properties (axisymmetry, homogeneity,...), conservation of a representative and controllable beam energy, compatibility with DRAG-ON geometry, pumping and available feed gases and finally implementation complexity, cost and ease of maintaining.

In an effort not to depreciate DRAG-ON's capabilities, the resulting neutral flow has to adhere to the designed flow requirements needed for effective ABEP intake testing and material degradation testing. Respecting all requirements perfectly is challenging, and limitations on available hardware in the facility is also a brake. Within the short timeframe of this project, the selected solution has to be both technically sound and realistic to implement quickly and at a reasonable cost.

4.1 Charge EXchange cell neutralization

Charge exchange has been introduced in Section 2.2.1. A direct way to exploit this mechanism for neutralization is to use a charge exchange cell: a dedicated chamber filled with a neutral gas at a certain local density. The ion beam is propagated through this region so that a fraction of ions undergoes charge exchange collisions, producing a fast neutral beam downstream. This concept is widely used in high-energy neutral beam systems, notably for fusion applications where neutral beams are required to cross magnetic fields. A representative example is the neutral beam injector design work for ITER discussed by Hemsworth et al. [31].

For DRAG-ON, the feasibility of such a solution can be assessed with a simple order-of-magnitude estimation. The main limitation is the maximal background pressure attainable within the operating range of the plasma source. In this work, following the usual facility guidelines, an upper limit of $p \simeq 1.5 \times 10^{-4}\,\mathrm{mbar}$ is considered. Assuming a constant pressure along the cell and an ion energy of the order of the VLEO-representative range ($\sim 5\,\mathrm{eV}$), Equation 2.11 provides a direct link between the neutral density, the charge-exchange cross section, and the interaction length required to reach a target neutralization probability.

Using this simplified model (constant n, constant σ_{CEX} evaluated at the considered energy), the required interaction length to reach $P_{\mathrm{CEX}} = 50\%$, 75% and 95% is found to be approximately $0.40\,\mathrm{m}$, $0.80\,\mathrm{m}$, and $1.73\,\mathrm{m}$ respectively. These values are not meant as an exact design result, but they already indicate the scale of the problem for DRAG-ON.

In practice, a charge-exchange neutralizer would also require an additional stage to remove the remaining ions downstream, which increases both the length and the mechanical complexity of the setup. Moreover, the plasma plume is expected to expand significantly with distance (see Section 3.3), meaning that a long cell would need a sufficiently large cross-section to avoid excessive beam interception on the walls.

With these constraints in mind, a charge exchange cell appears difficult to implement efficiently in DRAG-ON: a compact design compatible with the facility geometry would likely result in weak neutralization, while an efficient design would require a length (and volume) that is not realistic within the available space. For these reasons, charge-exchange cell neutralization is not pursued further in the present work, but it remains an interesting concept for future investigations about shape optimization and increased local pressure.

4.2 Secondary electron source neutralization

In the electric propulsion community, the term “neutralization” most often refers to space-charge neutralization of an ion beam: an external electron source is used to supply electrons so that the plume does not remain positively charged and does not create large potentials. Typical examples are hollow cathodes, cathodeless RF neutralizers, or plasma-bridge concepts [32].

However, this type of neutralization is **not** what is needed in the present work. The DRAG-ON objective is not only to make the plume “electrically neutral” in a global, macroscopic sense, but to reduce the ion fraction in a microscopic sense as well. VLEO conditions are not only neutral macroscopically but also microscopically since present species are mostly neutral. An electron source can balance charge, but it does not convert ions into fast neutrals: it changes the potential, not the number of ions.

In practice, the PFG plume in DRAG-ON is already considered quasi-neutral since electrons are co-extracted with the ions. This means that adding a secondary electron source would mostly “inject extra electrons” into an already quasi-neutral beam, potentially shifting local potentials or increasing the electron flux, but without addressing the core problem of ion removal. In other words: it can be a very good solution for thruster neutralization, but it is not suitable for the research carried out in DRAG-ON.

For these reasons, secondary-electron-source neutralization is not considered further in this thesis. The neutralization approaches retained for comparison are those that directly act on the ion population, namely charge-exchange-based neutralization and wall-neutralization concepts.

4.3 Flat plate neutralization

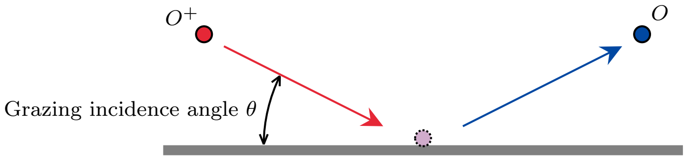

Figure 4.1: Basic schematic of surface neutralization on a flat plate at grazing incidence θ.

Flat-plate neutralization is a surface neutralization method: a positively charged ion approaches a conducting wall, captures an electron near the surface (Auger and/or resonant neutralization, see Section 2.2.2), and leaves the wall as a fast neutral. In the most idealized picture (smooth surface, shallow/grazing incidence), the outgoing neutral approximately conserves the incoming speed and reflects forward with a specular-like angle, as sketched in Figure 4.1. In practice, the neutral beam properties depend strongly on surface material/cleanliness/roughness, incidence angle, and how many interactions occur (single reflection vs multiple bounces), which all control energy loss and angular broadening. These effects of surface interaction are studied in depth by Jorge [8].

Two families of flat-plate neutralizers appear in the literature. The first one is the grazing low-angle forward-reflection approach, used to generate a directional neutral beam. A representative example is the AOSS/Vanderbilt neutral beam facility described by Albridge et al. [33]: ions are decelerated electrostatically, neutralized by grazing reflection on a macroscopically smooth nickel plate, and remaining ions are rejected downstream by a retarding mesh. In that work, the additional energy loss due to grazing reflection is reported to stay below a few percent, and the induced angular spread of the reflected beam is of the order of a few degrees. The neutralization efficiency itself is not necessarily large and depends on the operating point and surface: an estimation around $\sim 40\%$ is reported at 200 eV for N_2^+.

The same philosophy is used in a neutral-beam neutralizer system developed by Wieser and Wurz [25], where an electrostatic analyzer (ESA) and apertures are used to reject "parasitic" neutrals and shape a clean incoming ion beam before hitting a flat Tungsten neutralization surface. After scattering, the remaining charged particles can be removed by electrostatic deflection, leaving only a neutral beam. The trade-off is that such systems typically achieve their beam quality through strong geometrical/electrostatic filtering, which can lead to low overall transmission (*i.e.* only a small fraction of the original ion flux becomes a usable neutral beam).

The second family is a high-incidence (≈ 90 deg. redirection) approach, where the flow is intentionally turned by a reflecting plate rather than preserved as a forward-reflected beam. This approach results is a less directional neutral beam (scattering may be more diffuse) and possibly a broader range of energy. In the more recent development presented by Swami et al. [34], the neutralizer is combined with a grid in front of the plate to reduce the direct ion transmission toward the sample region. This would be an interesting setup to reproduce in DRAG-ON for further research on some aspects of ion-wall neutralization.

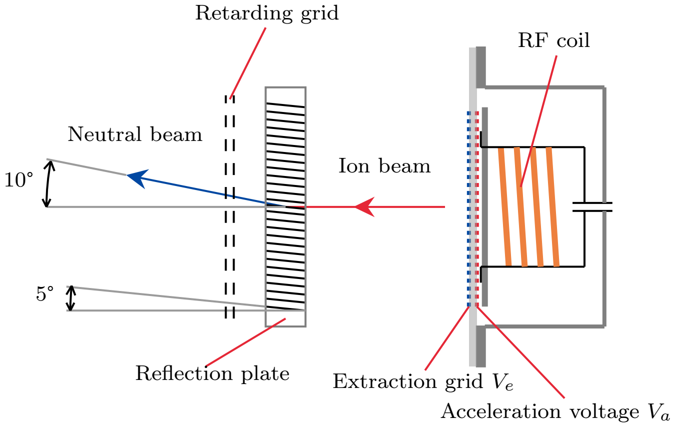

Figure 4.2: Schematic representation of the low-angle forward reflected neutral beam system. Directly adapted from Lee et al. [7] (fig. 1).

Finally, Lee et al. [7] proposes an extension of the grazing-incidence concept using multiple parallel reflector plates. The goal is essentially to increase the effective neutralization surface (and therefore the usable neutral flux) while keeping a forward-directed geometry. Their results indicate that lower reflection angles lead to higher degrees of neutralization, and that complete neutralization can be achieved by adding a retarding stage to reject the residual ions. Conceptually, this “multi-plate” philosophy is closer to the perforated-plate approach used in this thesis than a single flat plate: both rely on repeated ion-wall interactions to promote charge-state conversion while attempting to preserve a reasonably directed flow. This approach looks like a solid candidate to reach a high quality neutral beam and could be adapted to DRAG-ON.

This multi-plate neutralizers design philosophy is close to the perforated-plate solution already available at VKI and tested in this work. For these reasons, flat-plate neutralizers are considered here primarily as a reference and as a promising direction for future dedicated neutral-beam studies, rather than as the main neutralization solution retained in the present experimental campaign.

4.4 Perforated plate neutralization

The perforated plate is the neutralization solution selected in this thesis. The underlying physics is the same ion-wall neutralization mechanism introduced in Section 2.2.2, *i.e.* electron capture at a solid surface during an ion-wall interaction. The key difference

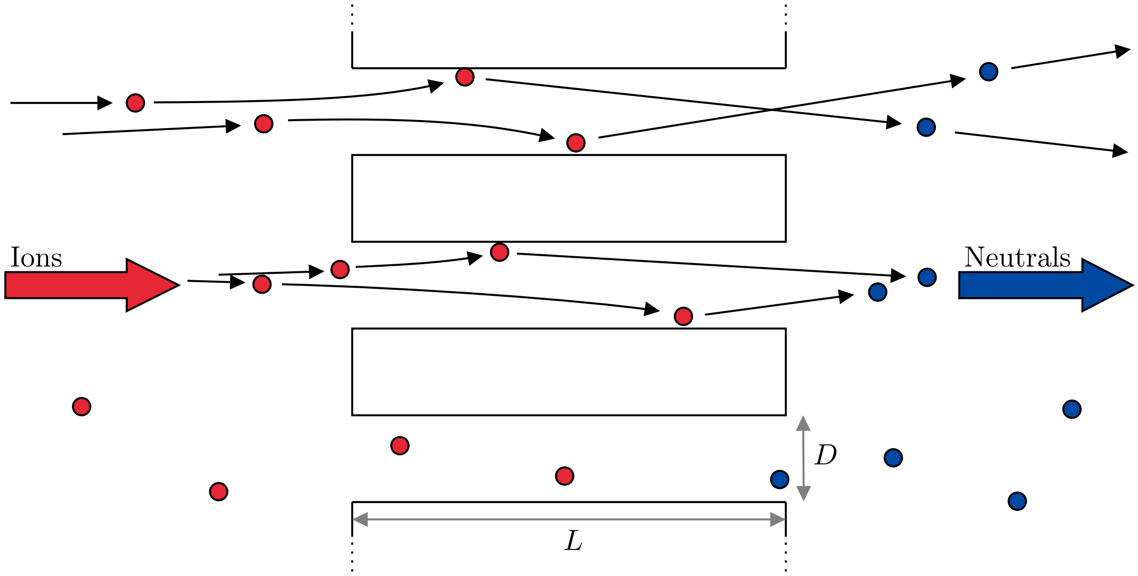

Figure 4.3: Schematic representation of the working principle of a perforated plate neutralizer.

compared to a single flat plate is geometric: instead of reflecting the beam on a single or multiple flat surfaces, the ions enter a channel aligned with the beam axis and undergo one or multiple collisions with the channel walls. These channels are schematically represented in Figure 4.3. From a microscopic point of view, the interaction with the walls is similar to a flat plate. On the macroscopic scale, taking only one channel into account might not make much sense; the flow is heavily restricted, the particles may undergo several collisions,... However when taking into account a larger pattern of these perforations, it makes much more sense. A grid like this do not modify the axisymmetric nature of the flow and is not expected to excessively disturb the average flow direction, albeit this approach has a relatively high flow blockage factor considering ease and cost of manufacture.

The plate can be viewed as an array of identical micro-channels (holes). Ions entering a hole may:

- pass through without touching the wall (remain ions),
- collide once or multiple times with the wall and become neutrals (surface neutralization),
- collide and be scattered to such an angle that they do not exit the hole (loss of transmitted flux).

Because the holes are aligned with the incoming beam, the plate acts as a forward neutralizer. This is conceptually close to the multi-plate forward-reflection idea proposed by Lee et al. [7], but with the benefit of preserving axisymmetry.

4.4.1 Design parameters

The main geometrical parameters are the hole diameter D and the plate thickness L, depicted in Figure 4.3. From those parameters, the aspect ratio is defined as

$$\mathrm{AR} = \frac{L}{D}. \tag{4.1}$$

Although referring to a single channel by definition, the aspect ratio is often used to describe the whole plate (*i.e.* "AR5 plate", which is a plate where all the channels have an aspect ratio AR$= 5$). Additional design parameters are the channels width, spacing, pattern, shape, area of the perforated area and shape of the perforated area. Most of these parameters are set by manufacturing constraints. The specific parameters selected for this work are presented in Section 5.1.3.

The expected qualitative trend when increasing aspect ratio is a general increase of the probability of ion-wall interactions inside a hole, therefore increasing the fraction of ions that can be neutralized. The trade-off is that repeated wall interactions also reduce the transmitted particle flux, broaden the angular distribution and broaden/shift the energy distribution. This means that a higher aspect ratio should lead to a better neutralization performance but there is a limit to this trend.

A closely related demonstration of a perforated plate-based neutralization approach for hyperthermal atomic oxygen is given by Hisamoto et al. [26], where an oxygen plasma is neutralized downstream of an ECR discharge and the resulting AO beam properties are inferred via erosion-based measurements. While the plasma source technology and geometry differ from DRAG-ON, this paper provides a strong experimental proof that surface neutralization can produce a directed hyperthermal AO beam in the few-eV range.

Overall, the perforated plate approach offers the best compromise with the DRAG-ON constraints. Unlike a CEX cell, it does not require raising the chamber pressure or adding a long neutralization volume. Compared to single flat-plate concepts, it preserves a mostly axial, axisymmetric transmitted flow while remaining compact and simple to integrate. Finally, perforated plates were already available at VKI with different aspect ratios, making the method immediately testable within this thesis timeframe. These plates were manufactured in the context of a Master's thesis by Gabriel Pascoli [14].

Chapter 5

Assessing perforated-plate neutralization efficiency

This chapter aims at assessing the neutralization efficiency of a perforated-plate neutralizer placed downstream of the particle flow generator in DRAG-ON. The objective is to infer this efficiency from empirical data. It will mostly be based on the fraction of ions in the flow that are neutralized through interactions with the plate. As stated in Chapter 3, available diagnostics in DRAG-ON are electrostatic. This means that the efficiency can only be computed indirectly since it's not possible to measure fast neutrals directly. Neutralization is therefore mainly inferred from the difference in measured ions behind the perforated-plate compared to the reference configuration without plate.

The residual ions approach to neutralization efficiency is discussed in Section 5.2. Two definitions are presented; a naive approach uses a flow blockage factor computed from perforated-plate geometry and the second definition uses empirical data from tests performed with a thin perforated-plate (AR0.2) presented in Section 5.1.3 to compute this flow blockage factor. Either way, these two definitions assume that the difference in measured ions resulted in an equal number of fast neutrals. However, without any direct neutral diagnostic method available, this assumption cannot be asserted.

Many different flow conditions were tested throughout several experimental campaigns. This allows for a full mapping of the conditions with and without a perforated-plate present downstream of the PFG. This large empirical dataset is discussed in Section 5.3. Specific parameters influencing neutralization are identified and the impact of the perforated-plate on more general conditions are discussed.

An unexpected impact of the perforated-plate on flow conditions compared to a reference setup without plate is that ion energy distribution is strongly modified. An apparent acceleration of the ion flux is observed, this phenomenon is discussed in Section 5.4. Experimental campaigns are carried out to try and better understand this phenomenon. One of the main characteristic of the LTA-100 PFG is the tunability of ion energy, it is therefore important to understand how ion energy is impacted by a neutralizer and how to keep control of this energy no matter the setup.

The final part of this chapter presents an alternative experimental method to try and measure the presence of fast neutrals. This new method is based on polyimide degradation measurements presented in Section 3.2.1. The experimental setup, the testing procedure and the measurement methods are described. Finally, results are presented showing signs of degradation from fast neutrals.

5.1 Experimental framework and capabilities

Different experimental setups were build and tested specifically for this research. This section aims at introducing the capabilities of the facility in a more practical way in order to better understand the specific setups presented in Section 5.3, Section 5.4, and Section 5.5. The limitations and constraints posed on experimental design are also addressed in this section in order to clarify some non-ideal aspects of the campaigns.

5.1.1 Facility modularity

Modularity is a core principle of the DRAG-ON facility design philosophy. Although the facility was primarily developed to study Air-Breathing Electric Propulsion (ABEP) systems (see Section 1.1.1), it was built to support a wide range of experimental configurations without major modifications of the facility.

As of today, the DRAG-ON facility has been employed for ground testing of ABEP intakes [35], characterization of satellite material degradation [36], as an experimental reference for numerical simulations [37], and for plasma diagnostics studies such as optical emission spectroscopy [13], among others.

The mechanical architecture of the facility greatly helps this modularity. Both chambers are equipped with extruded aluminum profiles fixed to the vacuum chambers structure. This allows hardware to be mounted, moved or removed with minimal effort. Users have a high degree of freedom when positioning the PFG, diagnostics, samples, and any other components. The particle flow generator (PFG), which is itself mounted on these structural profiles, can be translated along the central axis of the main chamber. This feature allows the axial distance between the source and downstream components to be adjusted depending on the experimental objectives. Precise alignment of the experimental chain is done thanks to a laser beam reference aligned with the facility's centerline. This makes repeatability between setups easier for the user.

Further flexibility is made possible by the linear translation stage introduced in Section 5.1.2. This system enables precise positioning along a chosen linear path of diagnostics or samples during an experimental campaign, without requiring venting of the vacuum chamber. The high-vacuum requirements of the facility makes the downtime between tests quite high if the facility is vented. The linear stage reduces this downtime.

In the context of this work, this modular framework allows for the realization of an axially aligned configuration. It is composed of the particle flow generator, a perforated-plate, and interchangeable downstream diagnostics and/or samples. In some setups, the perforated-plate is movable thanks to the linear stage, in others, the diagnostic plate/samples are mounted on the linear stage. The testing philosophy remained the same between setups, keeping this axial succession of parts, but some key modifications have to be implemented to make each test a succes. The Von Karman Institute has a fully equipped workshop and instrumentation lab. This makes it possible to manufacture specific holding or aligning solutions. Several mounting pieces were manufactured specifically and allowed for some freedom in the experimental designs explored in this work.

5.1.2 Linear translation stage

A linear translation stage is used throughout the experimental campaigns presented in this chapter. It is used to modify the position of the components mounted on it during a test. This system was developed in-house from a linear screw drive which is vacuum compatible and a linear guide rail.

The translation stage provides a single degree of freedom with a total travel distance of 240 mm with a degree of accuracy of the order of less then 1 mm. Depending on the experiment's needs, this degree of freedom can be oriented in any direction on a horizontal plane. For all the experiments presented in this chapter, this direction was set radially with respect to the particle flow axis. The test results presented in Section 3.3 and Appendix A were obtained with the linear stage aligned axially with respect to the flow. Any other angle of alignment is possible if required by the experimental setup.

The actuation is provided by a stepper motor connected to the drive screw inside of the vacuum chamber. It is connected to an Arduino controller on the outside with wires going through a feed-through on the chamber wall. Movement is controlled directly on the main control interface of the facility by linking the Arduino to the lab computer. This makes this system an easy to use solution for movement in vacuum.

Before each experimental campaign, the stage position(s) is calibrated using the reference laser aligned with the facility's centerline. This consistent alignment allows a good repeatability between tests. This calibration ensures that any equipment moved during a test can be reliably aligned with the center of the flow or any other desired location.

It should be noted that the current linear stage design has certain limitations in terms of reliability. Some issues, for instance the linear stage getting stuck during experiments, have been identified during recent campaigns. This effect getting worse with time, possibly linked to the linear rail's exposition to the plasma flow for extensive amounts of time. In order to negate this problem, a revised version of the linear stage is planned in the near future. It should improve the reliability of the system as well as incorporate a second degree of freedom to further improve the capabilities of the setup.

5.1.3 Perforated-plate geometry

The perforated plates are the central components of the experimental setups presented in this work. This section describes their geometry and design. The two main tunable parameters are the aspect ratio of the perforations and the physical dimensions of the plate. The aspect ratio (AR) of the cylindrical holes has been defined in Section 4.4. Since all perforations have the same diameter ($d = 1\,\text{mm}$), the plate thickness directly determines the aspect ratio. All perforated plates used in this study are manufactured from stainless steel. An overall description of their geometry is presented in Figure 5.1.

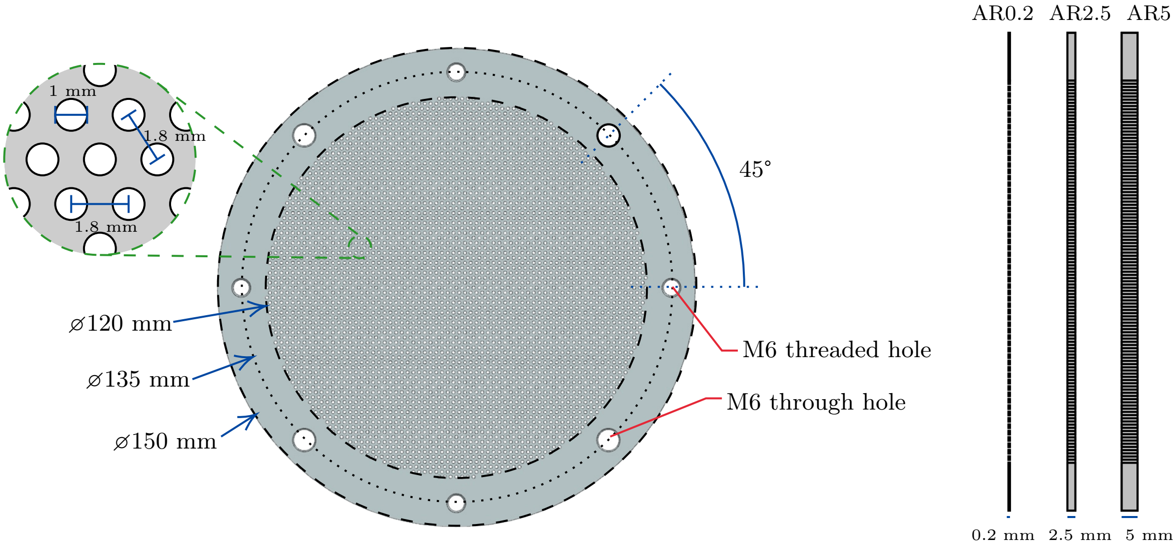

(a) Top view

(b) Side view

Figure 5.1: Drawn representation of the perforated plate geometry.

The external diameter of the plate, 150 mm, is chosen to match that of the diagnostic plate used for Faraday probe and MRFEA measurements (see Figure 3.1).This is also the same diameter as the outside of the end plane of the PFG (see Figure 1.4). Mechanical mounting is achieved through eight M6 holes distributed along the outer diameter as shown in Figure 5.1.

The perforated region occupies a central circular area whose diameter, 120 mm, is selected to be significantly larger than the core of the particle flow. This "core" refers to the approximately 0-3 cm radial region at the center of the flow over which a radially uniform flux has been identified in previous beam characterization campaigns [35]. This choice ensures that the interaction between the flow and the plate is not limited by edge effects associated with the perforated plate itself.

Each perforation has a diameter of 1 mm. In principle, minimizing the hole diameter would allow high aspect ratio plates with a smaller thickness, mass, and material consumption. However, practical manufacturing constraints, considering a plausible budget, impose a lower limit on the diameter. A diameter of 1 mm was selected as a compromise between geometric optimization and manufacturing cost.

The holes are arranged according to a regular triangular pattern, with a center-to-center spacing of 1.8 mm. This pattern is represented in the top left corner of Figure 5.1. As for the hole diameter, this spacing was minimized as much as possible while remaining compatible with standard machining.

Three different plate thicknesses are available: 0.2 mm, 2.5 mm, and 5 mm, corresponding to aspect ratios AR0.2, AR2.5, and AR5, respectively. The 2.5 mm and 5 mm plates were originally manufactured during the initial study by Pascoli [14] and were therefore already available at VKI at the start of the experimental campaigns.

A plate with an aspect ratio of AR7.5 can be obtained by stacking the AR2.5 and AR5 plates. This simple approach provides a cost-effective means of extending the explored range of aspect ratios without needing any additional manufacturing.

The AR0.2 plate was manufactured specifically for this study. Its primary purpose is to serve as a reference configuration that is not expected to neutralize ions in the flow through ion-wall interactions. Due to its very small thickness, this plate is supposed to serve as reference for geometric flow blockage. This thin plate is therefore useful in the definition and interpretation of neutralization metrics. It's impact on those metrics will be further discussed in Section 5.2.

5.2 Useful metric: the apparent neutralization efficiency

The main goal of the present work is to characterize the neutralization of a perforated-plate neutralizer. Therefore, a metric to quantify this how effective this neutralization is has to be defined. This metric should allow systematic comparison between different operating conditions, plate aspect ratios and plasma source settings. The literature on the efficiency of perforated plate neutralization being close to inexistent, this metric has to be derived from experimental data alone.

In the present work, neutralization is inferred from Faraday probe measurements of ion current density profiles downstream of the perforated-plate. These measurements are compared to the ion current density measured in a reference setup where the diagnostic plate remains in place and the perforated-plate is removed from the particle flow. These measurements provide access to the fraction of ions remaining after interaction (or not) with the plate, but do not directly resolve the fate of ions that are no longer detected.

The section introduces and defines the concept of an *apparent neutralization efficiency*. It's important to remember that this quantity does not represent a true neutralization efficiency, but rather an experimentally inferred upper bound based on ion current measurements.

5.2.1 Remaining-ion ratio

Let $j_{\mathrm{NoPlate}}(r)$ be the ion current density measured at radial position r in a reference configuration without a perforated-plate. $j_{\mathrm{Plate}}(r)$ is the corresponding profile measured with a perforated-plate installed in between the PFG and the diagnostic plate. A local remaining-ion ratio is defined as

$$R(r) = \frac{j_{\mathrm{Plate}}(r)}{j_{\mathrm{NoPlate}}(r)}. \tag{5.1}$$

This ratio represents the fraction of ions remaining at radius r after going through the plate. Those ions have most likely not touched the plate and went straight through a hole or their interaction with the channel wall did not result in neutralization. This ratio is directly obtained from experimental measurements and constitutes a fundamental observation used throughout this neutralization analysis.

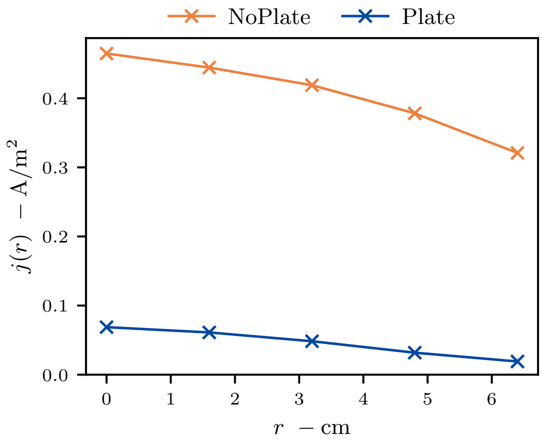

Figure 5.2: Example Faraday probe ion current density profiles measured downstream of the Plate and in the corresponding NoPlate reference configuration. The ratio between these profiles defines the remaining-ion ratio $R(r)$. Test conducted with the AR2.5 plate, a flow rate of 10 sccm Argon, $V_{\text{elec}} = 0\,\text{V}$, $I_{\text{coil}} = 0\,\text{A}$ and $P = 65\,\text{W}$.

While $R(r)$ provides a local measure of ion transmission through the plate, there is no distinction between purely genuine ion neutralization or flow blockage by the unperforated parts of the plate.

5.2.2 Naive apparent neutralization efficiency

A first definition of apparent neutralization efficiency can be defined by assuming that any reduction in ion current beyond purely geometrical interception is attributable to ion neutralization. It is considered a "naive" since it is the simplest interpretation of the remaining-ion ratio previously defined. The geometrical blocking factor β is introduced here.

The factor β represents the fraction of the beam cross-section that is physically obstructed by the solid material of the perforated plate, as defined from its geometry. For an ideal plate acting only as a passive mechanical obstacle, the expected remaining-ion ratio is

$$R_{\text{geom}} = 1 - \beta. \tag{5.2}$$

In the case of the perforated plates available for this work, referring to Figure 5.1, there are a total of 3985 holes with a diameter of 1 mm drilled over a circular surface with a diameter of 120 mm. Let $A_{\text{hole}} = \pi\, 0.5^2\,\text{mm}^2$ and $A_{\text{plate}} = \pi\, 60^2\,\text{mm}^2$ be the area of one perforated hole and the area of the perforated area on the surface of the plate, respectively.

This gives

$$\beta = 1 - \frac{3985 \cdot A_{\text{hole}}}{A_{\text{plate}}} \approx 0.723 \tag{5.3}$$

Using this geometrical reference, the naive apparent neutralization efficiency is defined as

$$\eta_{\text{geom}}(r) = 1 - \frac{R(r)}{1-\beta}. \tag{5.4}$$

By construction, $\eta_{\text{geom}}(r) = 0$ corresponds to a measured ion transmission fully explained by geometrical blockage, while $\eta_{\text{geom}}(r) > 0$ indicates an apparent additional ion loss attributed to neutralization processes. Under this definition $\eta_{\text{geom}}(r) = 1$ corresponds to the absence of ions after the plate, assuming all ions that were not blocked by the plate are neutralized. Under this definition it is also possible to see negative efficiency $\eta_{\text{geom}}(r) < 0$ if the measured amount of ions after the plate is greater then what's expected by the geometrical blockage factor.

Although intuitive, this formulation assumes that the geometrical blocking factor β accurately represents the ion transmission baseline in the absence of neutralization. In practice, additional effects such as beam divergence, angular scattering, or other electrostatic effects might affect the measured ion current independently of neutralization.

5.2.3 Baseline-corrected apparent neutralization efficiency

To mitigate some of the limitations associated with a purely geometrical reference, a baseline-corrected definition of apparent neutralization efficiency is introduced. This approach relies on experimental reference data obtained using the thin AR0.2 plate, which is assumed to induce negligible ion neutralization through ion-wall interactions. This reference measurement can be interpreted as an empirical measure of the geometrical blockage factor β defined above.

For this reference configuration, multiple Plate/NoPlate remaining-ion ratio profiles are measured under identical operating conditions. These profiles are averaged to construct an empirical baseline remaining-ion ratio $R_0(r)$.

Using this experimentally derived baseline, the apparent neutralization efficiency is defined locally as

$$\eta(r) = 1 - \frac{R(r)}{R_0(r)}. \tag{5.5}$$

The profile of apparent neutralization efficiency presented on Figure 5.3 shows that the flow blockage of the plate is not constant along the radius of the flow. This could be due to the angular distribution of the flow with respect to the plate. This formulation removes the explicit dependence on a geometrical blocking factor and makes the negative efficiency behavior impossible.

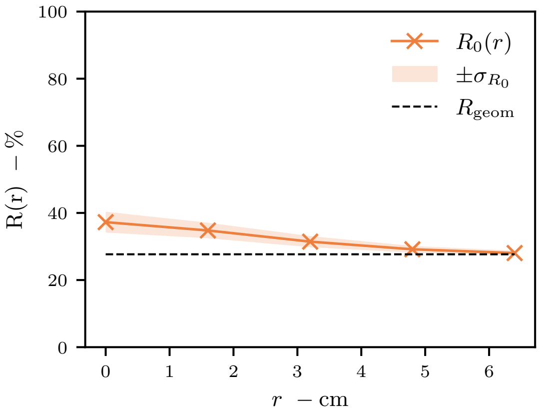

Figure 5.3: Average remaining-ion ratio with the AR0.2 plate $R_0(r)$, with the standard deviation $\pm\sigma_{R_0}$ highlighted. Over the full disk ($r = 6.4\,\mathrm{cm}$), $R_0(r)$ averages to $\overline{R_0} = 30.6 \pm 0.7\,\%$. $R_{\rm geom} = 1 - \beta$ from the naive definition is presented for comparison.

5.2.4 Interpretation and limitations

The apparent neutralization efficiency defined above represents an *upper bound* on the true neutralization efficiency. It assumes that all ions *not* detected downstream of the plate are converted into fast neutrals.

In reality, the actual value of efficiency is most probably lower then this idealized estimate. Additional loss mechanisms may contribute to the observed reduction in ion current, including ion reflection, angular redistribution after the plate, or any other mechanism that may not be measured. As no direct diagnostic of the neutral particle flux is available in the present experimental setup, the true neutralization fraction cannot be precisely quantified.

Therefore, this apparent neutralization efficiency should be viewed as a comparative tool between test conditions rather then an absolute metric of neutralization. Nonetheless, it is a good way of analyzing trends in efficiency when varying conditions such as plate aspect ratio, source biasing, flow rate, gas mixture, focusing coil current, etc.

5.3 Full mapping of the conditions

This section presents a systematic experimental mapping of the particle flow conditions downstream of the plasma source, both with and without the perforated plate installed. The objective is to characterize the evolution of the flow under a wide range of operating conditions. Rather than focusing on isolated test points, this mapping approach aims at identifying global trends in ion current density, ion energy distribution, and apparent neutralization efficiency as functions of controllable parameters such as gas flow rate, plasma source settings, and plate configuration.

This mapping of the conditions was mostly conducted using a gas mixture of 100% argon. This choice was motivated by the fact that erosion caused by ionic argon is negligible compared to ionic oxygen. Considering the long operating times required to acquire a large dataset spanning many operating conditions, this choice significantly reduces the risk of damages to facility components and diagnostics.

From a physical standpoint, global trends observed in flow conditions are not expected to vary (at least qualitatively) with gas mixture. Nonetheless, a limited number of measurements were made using argon-oxygen mixtures. This additional data did not reveal any contradiction with the assumption that the trends observed in pure argon remain valid when oxygen is introduced.

5.3.1 Test matrix and measurement procedure

In order to obtain a systematic and reproducible mapping of the flow conditions, a well structured experimental test matrix was defined. All measurements were performed by varying one operating parameter at a time within predefined bounds. All other parameters were kept constant. This approach allows the influence of each parameter on the measured quantities to be identified individually.

The absorbed RF power was kept constant throughout the campaign at

$$P = 65\,\mathrm{W}. \tag{5.6}$$

This level of absorbed power allows the source to remain within the $P_{\text{reflected}} \leq 10\,\mathrm{W}$ limit on reflected power mentioned in Section 1.2.1.

The investigated parameters and their corresponding ranges are summarized below:

- **Gas mass flow rate $\dot{m}$**: three discrete values were investigated,

  $$\dot{m} \in \{3,\ 6.5,\ 10\}\ \text{sccm}. \tag{5.7}$$

  These correspond to the usual lower, intermediate and upper limits of operation. Lower flow rates than 3 sccm results in the source being unstable and shutting off. Higher flow rates than 10 sccm makes the facility reach the operational limit in terms of reflected power and pressure.

- **Diagnostic type**: two electrostatic diagnostics were employed,
  - a Faraday probe array (FARA), used to measure radial ion current density profiles,
  - a magnetized retarding field energy analyzer (MRFEA), used to characterize ion energy distributions.

  The Faraday probes are swept from 0 to $-60\,\mathrm{V}$ by steps of $-5\,\mathrm{V}$ to allow the measurement of the floating potential V_f (see Section 3.1.1). The MRFEA is swept from 0 to 60 V by steps of 1 V. This small step provides good resolution and accuracy on the IVDF.

- **Perforated-plate configuration**: measurements were carried out both
  - without a perforated plate (baseline configuration) → **NoPlate**,
  - with a perforated plate → **Plate**.

  All measurements are then made for the different aspect ratio plates such that

  $$\mathrm{AR} \in \{2.5,\ 5,\ 7.5\}. \tag{5.8}$$

  Due to the timing of the test campaigns and delays in the manufacturing, the $AR0.2$ was not available during this test campaign. Only a limited number of measurement were taken with the thin plate installed. The global trends that are function of the aspect ratio of the plate are identified from the three thick plates, and are later confirmed by the limited measurements with the thin plate.

- **Magnetic lens coil current** I_{coil}: the current supplied to the magnetic focusing coil was set to

  $$I_{\mathrm{coil}} \in \{0,\ 1,\ 2\}\ \mathrm{A}, \tag{5.9}$$

  to check the influence of the plasma plume shape, which is strongly influenced by the magnetic lens, on the measured conditions.

- **Electrode voltage** V_{el}: for each configuration, the accelerating electrode voltage was set to

  $$V_{\mathrm{el}} \in \{0,\ -10,\ -20,\ -30,\ -40\}\ \mathrm{V}. \tag{5.10}$$

The measurements were always conducted following the same procedure. For a given gas mass flow rate, the diagnostic type was first selected (wiring to the acquisition interface has to be manually modified). For each diagnostic, measurements were then performed both with and without the perforated plate installed. This is possible thanks to the plate being fixed on a translational linear stage aligned in a radial direction (see Section 5.1.2). For a fixed plate configuration, all the combinations of coil current and electrode voltage values are swept automatically by the control interface of DRAG-ON.

Finally, this full procedure was repeated three times, once for each aspect ratio in Equation 5.8. Accounting for all the individual test conditions, different plates and diagnostics, a total of 540 measurements were made, excluding additional measured conditions such as the thin plate and argon-oxygen gas mixtures.

A measurement is recorded at each voltage level once steady-state conditions were reached. Each measurement consists of a voltage sweep of the diagnostic instrument and saving the values through an acquisition interface. At each voltage steps, a 1000 ms break is observed to allow conditions to reach steady state.

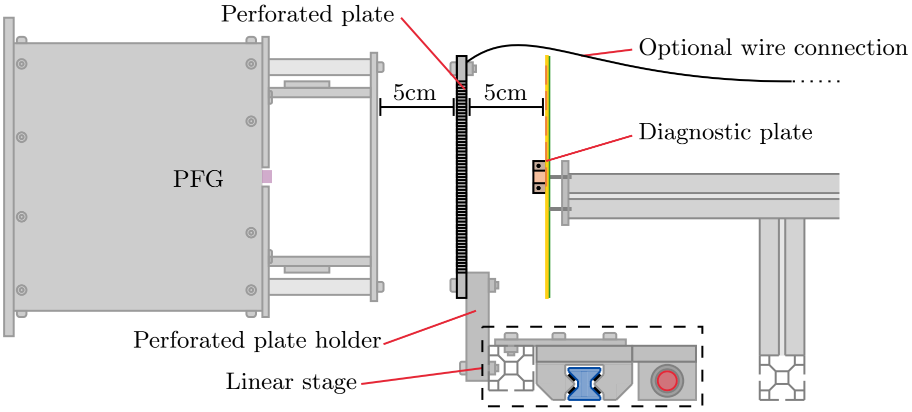

Figure 5.4: Schematic of the test setup with the perforated plate mounted on the linear stage.

5.3.2 Experimental setup

The experimental configuration used for the full mapping campaign is illustrated in Figure 5.4. The perforated plate is mounted on the linear translation stage, allowing to switch between the Plate and NoPlate setups. The linear stage is aligned radially with respect to the flow direction and is fixed so that the front face of the perforated plate sits 5 cm downstream of the exit plane of the PFG.

During this experimental campaign, the perforated plate was mounted on the linear stage with a pair of stainless steel holders. It was assumed that good electrical connection was made with the linear stage. In turn, the linear stage connection to the vacuum chamber structure was considered to be electrically connected. The whole facility structure, meaning the vacuum chamber, is grounded and used as electrical ground reference.

The diagnostic plate is fixed in place 5 cm downstream of the back face of the perforated plate. It is attached rigidly to the structure of the vacuum chamber. A PTFE holder plate is used to isolate it electrically from the rest of the facility. The instruments and guard electrode are connected to the outside of the facility through a D-SUB connector feed-through where it is wired to the acquisition interface and power supply to take measurements.

The diagnostic plate is fixed in the same direction as presented in Figure 3.1. The central Faraday probe is aligned with the centerline of the facility. This follows the experimental chain with the PFG and perforated plate also centered on that centerline. As shown on Figure 3.1, the MRFEA is positioned to the right of the plate, and therefore it actually measures the IVDF at a radius $r_{\mathrm{MRFEA}} \approx 3.5$, cm and not at the center point of the flow.

5.3.3 Results

This subsection presents the experimental results obtained from the systematic mapping of operating conditions described in Section 5.3.1, among others. The objective is to identify and isolate the influence of each controllable parameter on the relevant metrics.

Among the different flow metrics, the apparent neutralization efficiency is the most important one, as the neutralization process is the main focus of the present work. Since this efficiency is derived from ion current density measurements, the analysis of results start with ion current density profiles and the deduced total ion fluxes. Note that all neutralization efficiencies referred to in this Section 5.3 are based on the baseline-corrected apparent neutralization efficiency introduces in Section 5.2.3 rather then the naive approach defined in Section 5.2.2.

The influence of each parameter is discussed independently by comparing sets of measurements where all other operating conditions are kept constant. The ion energy distribution is not discussed in this subsection and is instead addressed separately in Section 5.4, where a more in-depth analysis is presented.

Total ion flux and ion current density distribution

In an effort to understand the impact of each parameter, first the impact of relevant parameters is observed on the ion current density profiles. The apparent neutralization efficiency being defined from ion current density profiles, it's obvious that understanding this is primordial. Both the absolute value of the ion flux and the distribution of density along the profile are studied.

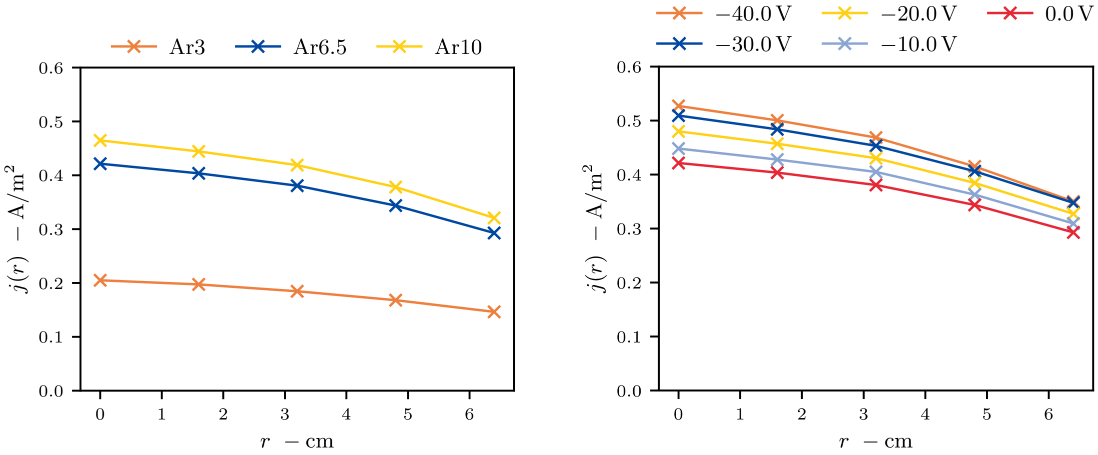

(a) $\dot{m} \in \{3, \; 6.5, \; 10\}$ sccm Ar. Constant: $V_{\text{elec}} = 0$ V.

(b) Variable: $V_{\text{elec}} \in \{0, -10, -20, -30, -40\}$ V. Constant: $\dot{m} = 6.5$ sccm Ar.

Figure 5.5: Ion current density as a function of radial position. Common constant conditions: $P = 65$ W, $I_{\text{coil}} = 0$ A, NoPlate setup.

Keeping all other parameters constant, Figure 5.5a shows that the total ion flux increases with increasing flow rate. This increase in ion flux does not significantly alter the shape of the radial ion current density distribution. The profiles remain similar in shape, with a roughly uniform central region and a comparable decay towards the edges. This behavior is observed across all comparison comparable to this one, meaning that whenever you keep all parameters constant except flow rate you observe similar results.

The relationship between gas flow rate and total ion flux does not appear to be linear over the explored range. A similar non-linear trend was previously reported by Pascoli [14], suggesting that ionization efficiency in the plasma source does not scale linearly with gas flow rate.

Keeping all other parameters constant, Figure 5.5b shows that the total ion flux increases with decreasing electrode voltage. The increase in ion flux with decreasing electrode voltage appears closer to linearity than the flow-rate dependence. However the limited number of comparable data points does not allow a definitive conclusion here.

Where the relationship between flow rate and ion flux is obvious; you input more gas, you get more ions, albeit not in a linear relationship, the link between electrode voltage and ion flux is less evident to draw. The dependence on electrode voltage is likely linked to the inner workings of the particle flow generator. A more detailed discussion of these mechanisms is beyond the scope of this work, it won't be pursued further due to the sensitive nature of the source design.

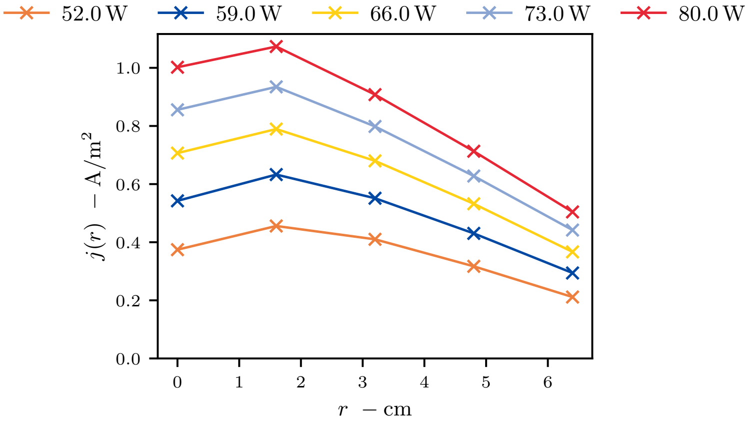

Figure 5.6: Ion current density as a function of radial position for different values of RF power $P \in \{52, 59, 66, 73, 80\}$ W. Constant conditions: $\dot{m} = 4.0$ sccm Ar, $V_{\text{elec}} = 0$ V, $I_{\text{coil}} = 2$ A, NoPlate setup.

Keeping all other parameters constant, Figure 5.6 shows that the total ion flux increases with increased power. The observed relationship between RF power and ion flux is approximately linear over the explored range. This behavior is consistent with an increased ionization fraction at higher absorbed power levels, leading to a larger number of ions. This is a well known phenomenon in plasma physics and is therefore expected.

As its name indicates it, the focusing coil, also known as the magnetic lens, is designed to focus the plasma beam towards the centerline of the flow. This effect is clearly visible in Figure 5.7, where increasing coil current leads to a higher ion current density in the central region of the profile.

In addition to increasing the peak ion current density near the centerline in most cases, magnetic focusing also increases the total ion flux measured on the diagnostic plane. This

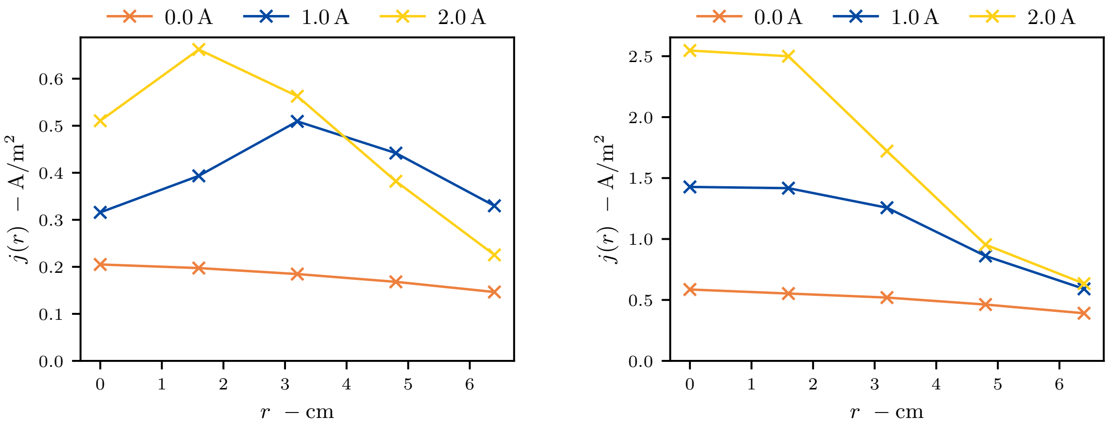

(a) Constant: $\dot{m} = 3\,\text{sccm Ar}$, $V_{\text{elec}} = 0\,\text{V}$. (b) Constant: $\dot{m} = 10\,\text{sccm Ar}$, $V_{\text{elec}} = -40\,\text{V}$.

Figure 5.7: Ion current density as a function of radial position for different values of coil current $I_{\text{coil}} \in \{0,\, 1,\, 2\}\,\text{A}$. Common constant conditions: $P = 65\,\text{W}$, NoPlate setup.

suggests that there is a reduction of ion losses between the source exit and the diagnostic plate. This could be due to less direct interactions with the quartz tube at the exit of the source and a more axial propagation of ions toward the diagnostic plane.

This focusing effect works in most parametrization of the source but it can happen that the system is badly calibrated for some conditions. An example of reduced focusing efficiency is shown in Figure 5.7a, where the expected central high-density region is not present. Here, the high density region is more in the shape of a hollow disc.

Some more in depth results about the focusing coil effect as a function of the applied current are presented by Jorge et al. [35]. Other examples of varying ion current density profiles as a function of coil current are also presented in Appendix A.

Effect of tunable parameters on apparent neutralization efficiency

The apparent neutralization efficiency results presented in the following all follow the definition of apparent neutralization efficiency based on the AR0.2 plate measurements. These efficiency values are therefore function of the radial position r. The same approach to results presentation as the previous section will be followed. The goal is to assess the impact of each controllable parameter on neutralization efficiency in order to better understand how this neutralization mechanism works.

Rather than presenting all possible parameter combinations explicitly, the results are organized to first have a more general view of efficiency, and then assess each tunable parameters one by one to estimate its impact on neutralization. This structured approach allows the main physical mechanisms to be highlighted while avoiding an excessive quantity of data and figures. Finally, Table 5.1 summarizes these results in a more concise way to get.

Core-averaged apparent neutralization efficiency

In order to get a more objective and systematic comparison between operating conditions, the core-averaged apparent neutralization efficiency $\overline{\eta}_{\text{core}}$ is introduced,

$$\overline{\eta}_{\text{core}} = \frac{\displaystyle\int_0^{r_c} \eta(r)\, 2\pi r \, \mathrm{d}r}{\displaystyle\int_0^{r_c} 2\pi r \, \mathrm{d}r} = \frac{2}{r_c^2} \int_0^{r_c} \eta(r)\, r \, \mathrm{d}r. \tag{5.11}$$

with $r_c = 3\,\text{cm}$, corresponding to the radially uniform core region identified in previous beam characterization campaigns. This metric better captures the relevant part of the flow.

General overview from radial efficiency profiles

The apparent neutralization efficiency is first analyzed as a function of the radial position. These radial profiles provide a good understanding of the spatial distribution of neutralization, in particular the efficiency observed in the core region of the flow.

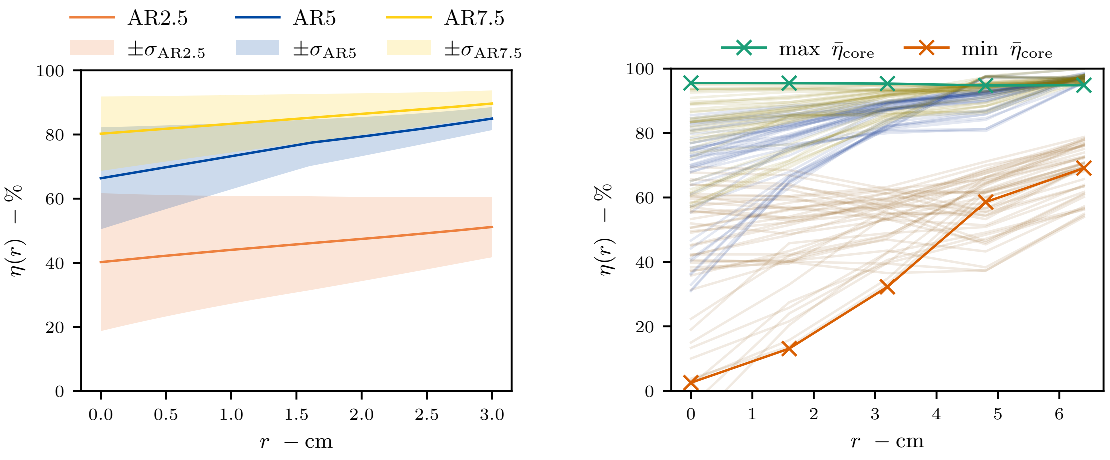

(a) Average efficiency profile and standard-deviation for different plate aspect ratios.

(b) Radial profiles of the operating conditions with maximum and minimum $\overline{\eta}_{\text{core}}$ highlighted.

Figure 5.8: General view of the radial apparent efficiency distribution computed for the whole dataset.

Figure 5.8a presents the average apparent neutralization efficiency for each plate geometry. The standard-deviation is also presented, showing that there is a large variability in efficiency. It is clear that there is a strong correlation between efficiency and plate aspect ratio. The plates were designed with this in mind. These results confirm the assumption that a larger perforated hole aspect ratio leads to better neutralization. However, the relationship between efficiency and plate aspect ratio does not seem to be linear. This is an expected observation since the efficiency can only tend towards 100 % efficiency, a linear relationship wouldn't make sense.

Figure 5.8b identifies the best and worst operating conditions in terms of neutralization efficiency. The best neutralization in the core of the flow reaches $\overline{\eta}_{\mathrm{core}} = 95.45\,\%$ which is the average value over a centered disc of radius $r_c = 3\,\mathrm{cm}$. This maximum is reached with the AR7.5 plate, $\dot{m} = 10\,\mathrm{sccm\,Ar}$, $V_{\mathrm{elec}} = -40\,\mathrm{V}$ and $I_{\mathrm{coil}} = 2\,\mathrm{A}$. The lowest value of core efficiency is $\overline{\eta}_{\mathrm{core}} = 18.70\,\%$ with the AR2.5 plate, $\dot{m} = 3\,\mathrm{sccm\,Ar}$, $V_{\mathrm{elec}} = -30\,\mathrm{V}$ and $I_{\mathrm{coil}} = 0\,\mathrm{A}$. The following sensitivity analysis aims at understanding the parameters influencing these large differences in efficiency.

Influence of gas mass flow rate

The influence of gas mass flow rate on the apparent neutralization efficiency is first examined. For this analysis, all operating parameters other than the flow rate are held constant. It is assumed that, unless counter-indicated, all results presented in this section are from pure Argon gas flows.

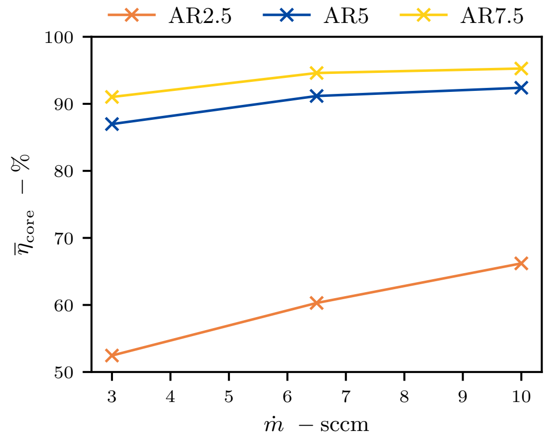

Constant parameters:

- $V_{\mathrm{elec}} = 0\,\mathrm{V}$,
- $I_{\mathrm{coil}} = 2\,\mathrm{A}$,
- $P = 65\,\mathrm{W}$.

Figure 5.9: Core-averaged apparent neutralization efficiency as a function of gas mass flow rate for different perforated-plate aspect ratios. All other operating parameters are held constant.

Figure 5.9 presents the evolution of the efficiency as a function of the flow rate. For each aspect ratio presented here, the increasing relationship between flow rate and efficiency, albeit non-linear, is evident. These results, and their non-linear nature, were already identified by Pascoli [14]. These results confirm it on a larger dataset.

Influence of electrode voltage

The effect of the accelerating electrode voltage on neutralization efficiency is studied next. As for the previous case, all other operating parameters are fixed to isolate the influence of this variable.

Here the relationship is less evident than for flow rate. Figure 5.10 exhibits some slightly different behavior for different plate aspect ratios. Only one set of conditions (other than aspect ratio) is presented here, however this is a representative sample of the rest of the

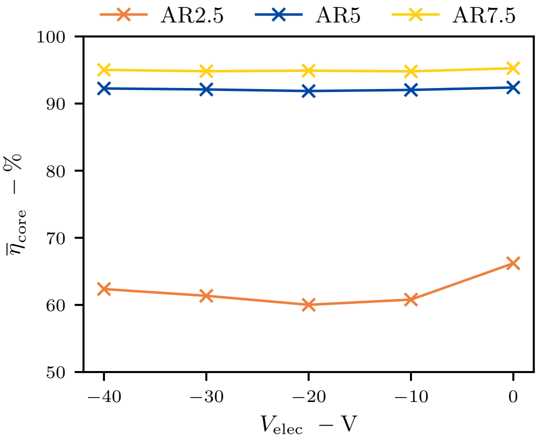

Constant parameters:

- $\dot{m} = 10\,\text{sccm Ar}$,
- $I_{\text{coil}} = 2\,\text{A}$,
- $P = 65\,\text{W}$.

Figure 5.10: Core-averaged apparent neutralization efficiency as a function of electrode voltage for different perforated-plate aspect ratios. All other operating parameters are held constant.

population. The general trend observed is that efficiency is barely noticeably higher for low potential (high absolute value potential), and this for both AR5 and AR7.5 cases. AR2.5 usually shows a more sporadic behavior illustrated here. No real trend is noticeable as most conditions will exhibit a similar but random efficiency profile pattern.

Influence of magnetic focusing coil current

The same analysis is carried out on coil current.

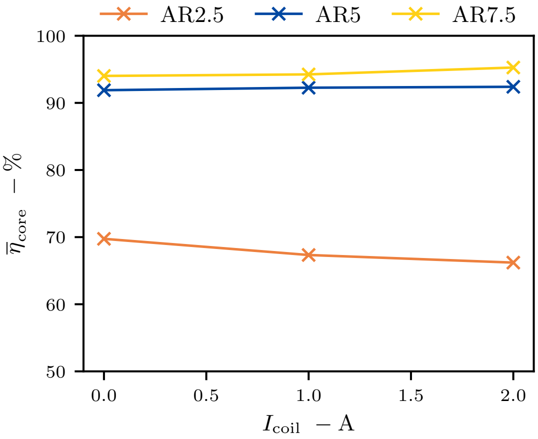

Constant parameters:

- $\dot{m} = 10\,\text{sccm Ar}$,
- $V_{\text{elec}} = 0\,\text{V}$,
- $P = 65\,\text{W}$.

Figure 5.11: Core-averaged apparent neutralization efficiency as a function of focusing coil current for different perforated-plate aspect ratios. All other operating parameters are held constant.

Once again, the measurement sample presented in Figure 5.11 only represents one set of conditions. This particular example shows a slight increase in efficiency with increasing current for AR5 and AR7.5, and the opposite effect for AR2.5, although the observed variations remain small. The general trend for the whole set of varying coil currents is more random than with electrode voltage. Here it is not possible to infer any trends linking coil current to efficiency when taking the whole dataset into account.

Influence of absorbed power

The full mapping experimental campaign did not account for a systematic study of power variation. The data used to infer its influence of efficiency comes from subsequent test campaigns where the power was varied for given sets of conditions. However, these tests were very limited explaining the fact that only two sets of conditions were measured.

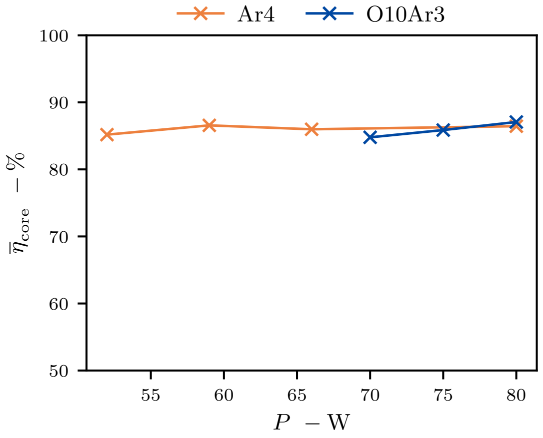

Constant parameters:

- AR = 5,
- $V_{\mathrm{elec}} = 0\,\mathrm{V}$,
- $I_{\mathrm{coil}} = 2\,\mathrm{A}$.

Figure 5.12: Core-averaged apparent neutralization efficiency as a function of focusing absorbed power for different gas mixtures and flow rates. All other operating parameters are held constant.

In this case, only two sets of conditions are available, the first was ran on a flow rate of 4 sccm of pure Argon over 5 power settings. Unfortunately, one of these measurement (73 W) is corrupted, most likely due to a user error causing a bad connection of the acquisition interface. The second set of conditions was ran with a mixture of 3 sccm of Argon and 10 sccm of Oxygen.

The Argon sample exhibits a slight increase in efficiency with rising power. However this effect is not clear enough to discard randomness. The Argon-Oxygen mix shows a similar but stronger increase in efficiency with rising power.

Global sensitivity summary

In order to synthesize the results presented above and avoid redundant graphical representations, the relative influence of each investigated parameter on apparent neutralization efficiency is reviewed over the full available dataset. The identified trends and their importance are qualitatively summarized in Table 5.1.

Table 5.1 highlights that the perforated-plate aspect ratio is the dominant parameter governing apparent neutralization efficiency. The effect of flow rate is also significant,

Table 5.1: Qualitative sensitivity of apparent neutralization efficiency to operating parameters.

Parameter	Influence	Trend	Typical magnitude
Flow rate	Strong	Monotonic increase	$\sim 5 - 10\,\%$
Electrode voltage	Weak	Slight increase	Within uncertainty
Coil current	Negligible	No clear trend	–
Plate aspect ratio	Strong	Monotonic increase	>> 10 %
Applied power	Moderate	Increasing	∼ 2 - 3%

raising some questions about this mechanism. Nor the effect itself nor it's non-linear nature are really understood, this would benefit from further research. Other operating parameters play a secondary or negligible role.

5.4 Ion acceleration phenomenon investigation

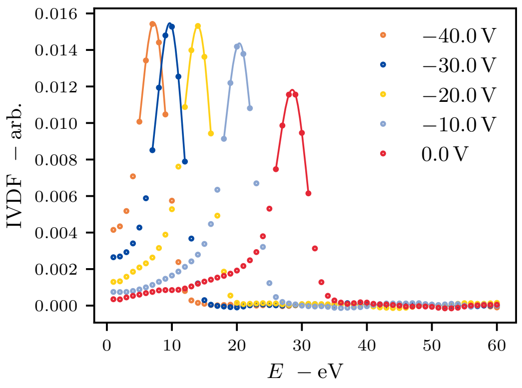

Figure 5.13: Most probable ion energy shifting with respect to V_{elec} under normal operations in the NoPlate setup. The flow rate $\dot{m} = 6.5$ sccm Ar, power $P = 65$ W and coil current $I_{\mathrm{coil}} = 1$ A are kept constant.

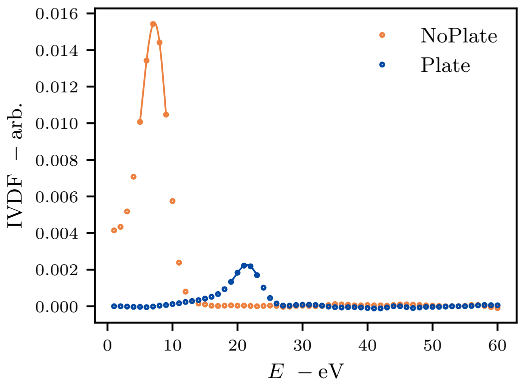

Figure 5.14: Example of most probable ion energy shift due to the presence of a perforated plate. All other parameters are kept constant, here: AR2.5, $\dot{m} = 6.5$ sccm Ar, $V_{\mathrm{elec}} = -40$ V, $P = 65$ W and $I_{\mathrm{coil}} = 1$ A.

The DRAG-ON facility is aimed at being versatile in its experimental abilities. One of the aspects that enables this is the fact the ion energy exiting the PFG is controllable. The main parameter that controls this is the electrode voltage. Figure 5.13 shows the IVDF of different operating conditions where the electrode voltage is varied and all other tunable parameters are kept constant. The lower the electrode voltage, the lower the value of the most probable energy E_{mp}. This control allows the user to select a specific ion energy when designing experiments.

Figure 5.14 presents an example of this effect. Here all operating parameters are kept constant except for the presence or not of the perforated plate in the plasma flow. It's important to point out that the area under the IVDF curve is linked to the ion flux, this explains the large difference in peak height. The interesting metric here is the most probable ion energy E_{mp} that corresponds to the peak of the IVDF curve easily identified on the figure. The acceleration effect is clearly observable in this case, for the NoPlate setup, $E_{mp} = 7.21\,\text{eV}$ while in the case of the Plate setup, $E_{mp} = 21.44\,\text{eV}$.

The most interesting range of ion energy in DRAG-ON is around 5 eV. For single oxygen atoms, this is the energy corresponding to 8 km/s, which is around the orbiting velocity of a satellite in very low earth orbit. This accelerating phenomenon makes it impossible to reach these kind of energies, which is counter-productive for a study aiming at improving the physical representativeness of the facility.

5.4.1 Observations from the full-mapping dataset

A full systematic study of all parameters such as the one made in Section 5.3.3 would be unnecessarily long. The section will only focus on identifying the main parameters influencing ion acceleration. It turns out that there is only one operational parameter that has a significant influence on ion acceleration.

Let's introduce the metric $\Delta E_{mp} = E_{mp,\text{Plate}} - E_{mp,\text{NoPlate}}$. It will be referred to as the apparent ion acceleration. That is simply the difference between the Plate and NoPlate setups most probable ion energy. It's defined positive for higher values in the Plate setup compared to the NoPlate one.

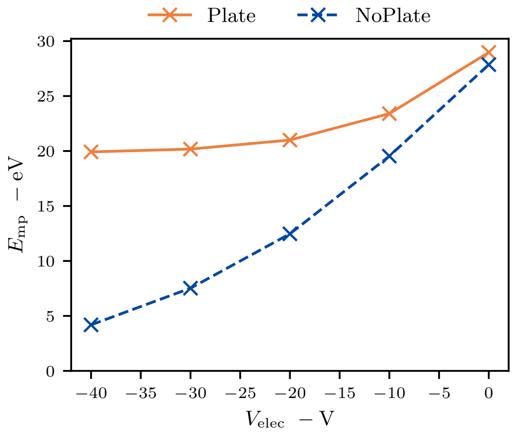

Figure 5.15: Most probable ion energy as a function of electrode voltage for both the Plate and NoPlate setups. All other parameters are kept constant: AR2.5, $\dot{m} = 6.5$ sccm Ar, $P = 65$ W and $I_{\text{coil}} = 2$ A.

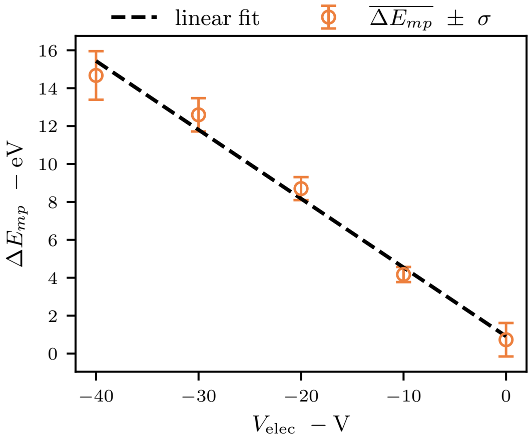

Figure 5.16: Average apparent ion acceleration as a function of electrode voltage for all operating conditions. ± standard-deviation is highlighted.

Electrode voltage is the tunable parameter that has the most influence on apparent ion acceleration. Figure 5.16 showcases a clear linear relationship between acceleration and electrode voltage. All operating conditions tested during the full-mapping campaign are averaged by electrode voltage value and displayed. This shows that this relationship is global; it is observed regardless of flow conditions.

A metric that has not been looked at yet in this work is the floating potential. For every ion current density measurements, the Faraday probes are swept from 0 to −60 V. As explained in Section 3.1.1 the floating potential can be recovered from such a measurement. To allow the study of this metric with respect to the Plate versus NoPlate setups, the metric $\Delta V_f = V_{f,\text{NoPlate}} - V_{f,\text{Plate}}$ is introduced. It will be referred to as the floating potential gain. It is defined positive when the NoPlate floating potential is higher than the Plate floating potential.

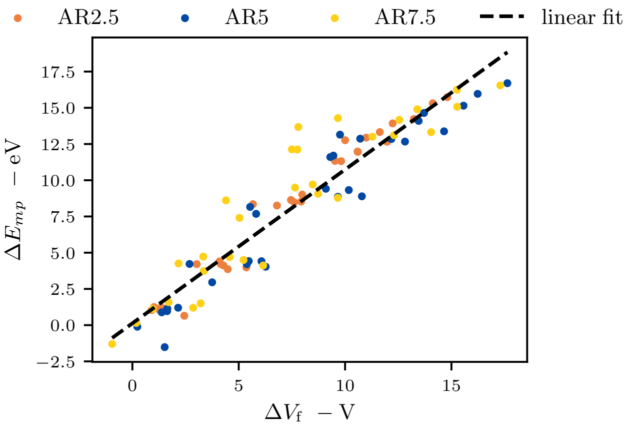

Figure 5.17: Apparent ion acceleration as a function of the floating potential gain. All conditions are included with the aspect ratio being highlighted.

Once again, a relationship between ion acceleration and floating potential can be inferred from Figure 5.17. As defined in Chapter 3, the floating potential is a measure of the potential at which ion and electron flux are equivalent. This suggests a significant effect of the perforated plate on the electrons present in the plasma flow.

The distribution of aspect ratio values across Figure 5.17 suggests that the aspect ratio of the plate might have no effect on the apparent ion acceleration. This is an interesting behavior that needs to be confirmed.

Both Figure 5.18a and Figure 5.18b suggest no significant influence of aspect ratio on ion acceleration. This is an interesting characteristic of the perforated plate. The confirmation of the independence assumption between plate geometry and ion energy enables a new experimental campaign to measure neutral flux. This new experiment is further discussed in Section 5.5.

Although the trends identified above are interesting and provide useful guidance, they do not explain the full picture. At this stage, the physical mechanisms responsible for the apparent ion acceleration remain unclear. From an experimental point of view, it is still difficult to determine whether this behavior corresponds to a real physical effect occurring in the plasma-plate interaction, or if it is partly (or entirely) caused by measurement artifacts or diagnostic biases. As a result, despite the consistency of the observed correlations, the interpretation of the phenomenon remains open, and further dedicated experiments would be required to clarify the underlying physics.

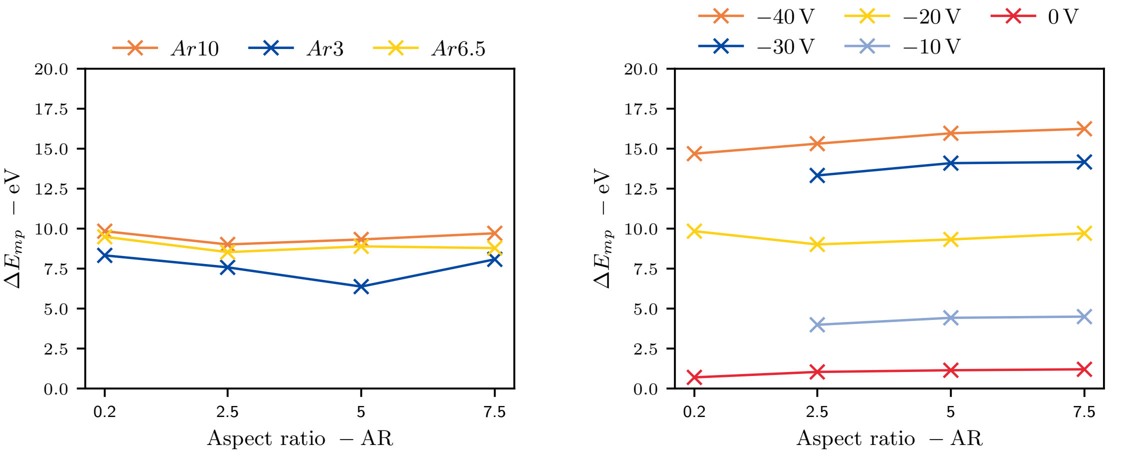

(a) $\dot{m} \in \{3, 6.5, 10\}$ sccm Ar and $V_{\text{elec}} = 0$ V

(b) $V_{\text{elec}} \in \{-40, -30, -20, -10, 0\}$ V and $\dot{m} = 10$ sccm Ar.

Figure 5.18: Apparent ion acceleration as a function of plate aspect ratio for different flow rates (left) and electrode voltage (right). Common constant conditions: $P = 65$ W and $I_{\text{coil}} = 2$ A.

5.4.2 Biased plate experimental setup

Here the idea of a biased plate setup is introduced. Until now, the plate was considered to be grounded through its mounting interface with the facility which was all metal. This was a usual assumption made in the facility. However, resistivity measurement a comparable experimental setup tested recently showed a quite high resistivity between the test subject and the facility structure which is grounded and taken as ground reference. Unfortunately, no resistance measurement was done on the perforated plate setup.

In order to verify that the grounding of the perforated plate was effective during the full mapping test campaign, the experimental setup was replicated and this time the plate was grounded directly with a wire connection (hence the optional wire depicted on Figure 5.4). Resistance was measured to be negligible (on the order of less then 1 ohm (instrument precision)). The results obtained on that specific wire grounded setup showed no difference with the measurements performed during the full mapping campaign.

In order to enlarge the empirical dataset on this apparent ion acceleration phenomenon, a new experimental setup was designed. The goal is to answer the question of the impact of the difference in potential between the plasma source and the perforated plate. This interrogation comes from some additional measurements that were taken with the plasma source in it's "floating" mode and the perforated plate grounded. A slight deceleration of ions was observed. The apparent ion acceleration has been studied with a variable potential in the source and constant one on the plate, let's test it the other way around; keep the source at a constant potential and vary the plate potential.

The experimental setup is similar to the one used previously. A new plate holder has been manufactured from PTFE in order to isolate electrically the plate from the rest of the

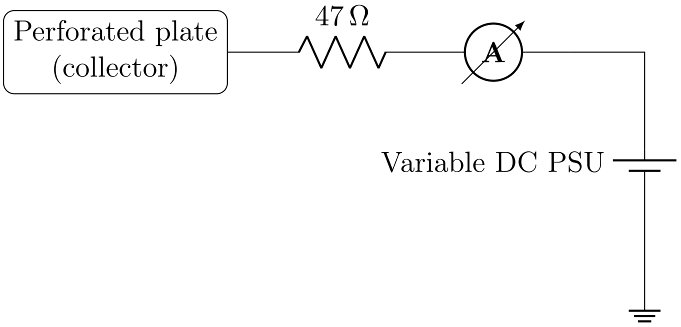

Figure 5.19: Electrical diagram of the biased plate experimental setup.

structure. Figure 5.19 presents a simple electrical diagram of the biased plate experimental setup. The optional wire connection mentioned in Figure 5.4 is passed to the outside of the vacuum chamber through a feed-through. It is connected in series to a 47 Ω resistor, a ammeter to monitor current, and a power supply which is connected to the facility ground reference. This setup allows the biasing of the plate to any reasonable potential, both positive or negative. In order to reach a desired potential on the plate, the potential applied on the power supply takes into account the voltage drop caused by the resistor.

This setup has been tested in various operating conditions. The plasma source is kept at a constant electrode voltage $V_{\mathrm{elec}} = 0\,\mathrm{V}$ while the perforated plate is biased to various values of plate potential V_{plate}. The dataset collected during this experimental campaign is not as systematic and complete as the one compiled in the full mapping campaign, yet some interesting results came out of it.

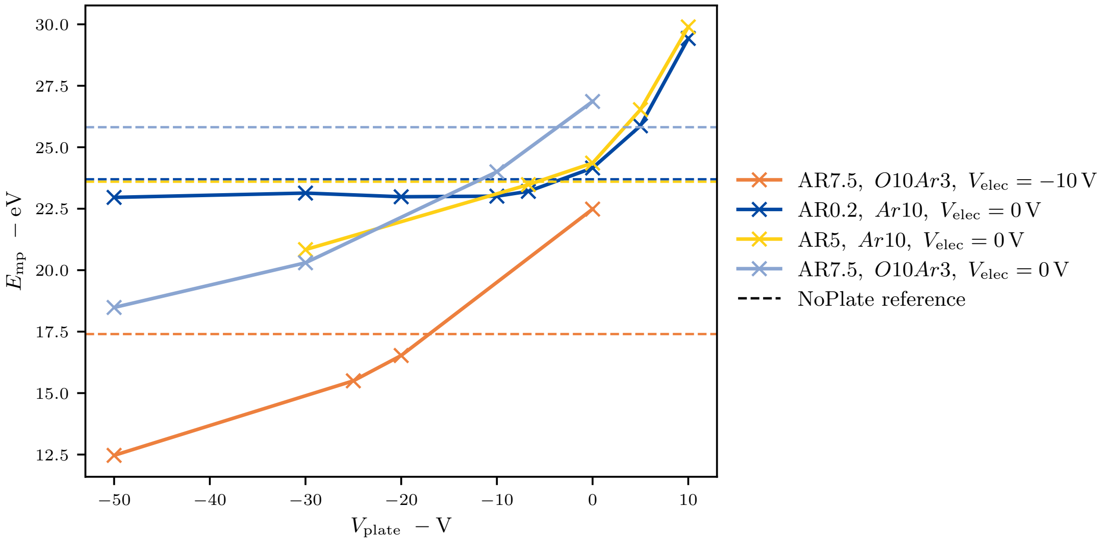

Figure 5.20: Most probable ion energy as a function of plate potential for different operating conditions and constant $I_{\mathrm{coil}} = 2\,\mathrm{A}$.

Figure 5.20 presents the evolution of ion energy as a function of plate biasing. The reference ion energy for each condition is highlighted by the color matched horizontal dashed line. First, let's address the sporadic nature of the data presented. This kind of setup, where a component is biased in the plasma flow is a first in DRAG-ON. The approach to the biasing limits was cautious to avoid any unaccounted for or unwanted effects. Some concerns during testing and issues with the linear stage (see Section 5.1.2) resulted in the test of only a few conditions and only a limited range of biasing potential on some conditions. Nonetheless, the results presented in Figure 5.20 show a clear relationship between plate biasing and apparent ion acceleration.

The fact that ions appear to be accelerated for positive biasing and decelerated for negative biasing is quite surprising. A naive interpretation of such a setup would be to assume that the perforated plate acts as an acceleration grid on an ion thruster[38]. This interpretation would assume ions (that are assumed to be positively charged) to be repelled by a positively charged surface, having an effect of deceleration on the ion flow. The opposite would be expected with a negatively biased surface where ions should be accelerated. However, this is the exact opposite of the behavior observed in this experimental setup. This hints that the physical effects at play here are more complicated then a trivial explanation. Further investigating this subject is paramount if the perforated plate solution is planned for future use in the DRAG-ON facility as a viable neutralization mean. Further investigation is however outside of the scope of this work.

Even though the physical reason for this apparent ion acceleration is not fully understood. The fact that a negative bias on the perforated plate causes a deceleration of ions is a positive result. Further measurements made on the same experimental setup revealed that the deceleration behavior at negative bias remains true with the plasma source also biased negatively. This initial operating principle of the source that allows for ion energy control is therefore made possible with the perforated plate setup thanks to the biasing of the plate. The fact that control of ion energy is regained enables a new experimental setup that aims at measuring neutral flow. It is further discussed in Section 5.5.

5.5 Kapton degradation test

The Kapton degradation test is the name given to an experiment aiming at measuring indirectly a flow of fast neutrals downstream of a perforated plate neutralizer. The DRAG-ON facility is equipped with a multitude of electrostatic diagnostic solutions but no direct neutral diagnostic.

This experiment can be described as a pragmatic experimental setup designed within limitations imposed by available diagnostics, budget, and time constraints. It is based on the polyimide degradation measurement approach introduced in Section 3.2.1. In this case, the neutral flux is not monitored in real time during the test, as it is the case with a quartz crystal microbalance (QCM), but is instead inferred from material erosion measurements after the test.

The test consists in a long-duration exposure experiment, during which Kapton HN samples (a polyimide) are exposed to a plasma flow generated from an argon-oxygen gas mixture, downstream of a perforated plate neutralizer. The test draws inspiration from QCM-based diagnostics—where polyimide mass loss is used as to infer neutral flux—it also builds on the extensive experience gained from material resistance tests against ionic atomic oxygen already conducted in the DRAG-ON facility [36].

The erosion depth of the Kapton samples is measured after exposure. By comparing the measured erosion to the erosion expected from ions alone, the experiment can lead to two possible outcomes. Either the contribution of neutral-induced erosion is negligible or below the measurement uncertainty, or a significant fraction of the erosion cannot be attributed to ions and must therefore be caused by fast neutrals. In the latter case, the experiment provides evidence for effective neutralization of the plasma flow. It is important to note that this method does not allow to distinguish the neutral energy and neutral fluence.

This section presents the experimental setup, the underlying assumptions, and the preliminary model used to interpret the results. The test conditions are then detailed, followed by the post-processing procedure and a discussion of the obtained results.

5.5.1 Methodology

The Kapton degradation test relies on a set of assumptions and a simple analytical model. Two long-duration exposure tests are performed: the first using the AR0.2 perforated plate and the second using the AR7.5 plate. It is assumed that, due to its geometry, the AR0.2 plate does not significantly neutralize ions. As a result, no measurable flux of fast neutrals is expected downstream of this thin plate.

The ionic erosion yield, defined as the volume of material eroded per incident ion, is assumed to be identical for both plate configurations. The operating conditions are kept strictly identical for both tests. Furthermore, the results presented in Section 5.4.1 show that the apparent ion acceleration is independent of the plate aspect ratio. Therefore, the ion energy, and more generally any parameter that could influence the ionic erosion yield, is assumed to be identical for both tests.

After the exposure tests, the results are interpreted using the following relations.

Let Y_i be the ion erosion yield,
Y_n be the neutral erosion yield,
d_1 be the erosion depth of the AR0.2 test,
d_2 be the erosion depth of the AR7.5 test,
and $F_{a,b}$ denote the fluence of species a in test b.

The definition of erosion depth gives

$$d_1 = d_{1,i} + d_{1,n} = F_{i,1}Y_i + F_{n,1}Y_n, \tag{5.12}$$

$$d_2 = d_{2,i} + d_{2,n} = F_{i,2}Y_i + F_{n,2}Y_n. \tag{5.13}$$

The AR0.2 plate is assumed to provide no neutralization, giving $F_{n,1} = 0$. Equation (5.12) becomes

$$Y_i = \frac{d_1}{F_{i,1}}. \tag{5.14}$$

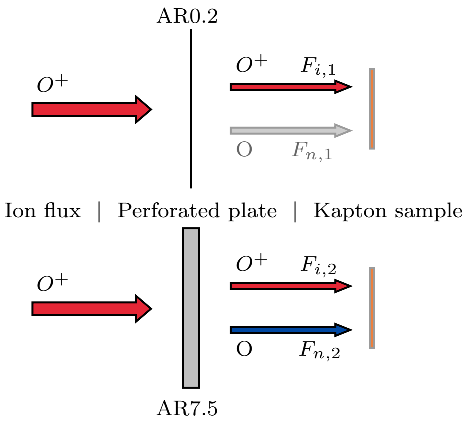

Figure 5.21: Working principle of the Kapton degradation test.

Combining Equation 5.14 and Equation 5.13 yields

$$F_{n,2}Y_n = d_{2,n} = d_2 - F_{i,2}Y_i. \tag{5.15}$$

Equation 5.15 is used to interpret the outcome of the Kapton degradation test. Two limiting cases are considered.

If

$$d_{2,n} \simeq 0 \quad \text{(within measurement uncertainty)}, \tag{5.16}$$

then no significant erosion attributable to fast neutrals can be identified. In this case, either the neutral flux downstream of the perforated plate is negligible, or its effect remains below the sensitivity of the measurement.

If instead

$$d_{2,n} \gg 0, \tag{5.17}$$

and exceeds the combined experimental uncertainty, then a non-negligible neutral-induced erosion is present. Under the assumptions stated above, this constitutes direct evidence of flow neutralization occurring downstream of the perforated plate.

This method provides access only to the product $F_{n,2}Y_n$ and therefore does not allow the neutral fluence and neutral energy to be distinguished.

5.5.2 Experimental setup

The Kapton degradation test setup is illustrated in Figure 5.22. A Kapton sample holder and a diagnostic plate are mounted on the linear translation stage, allowing precise align-

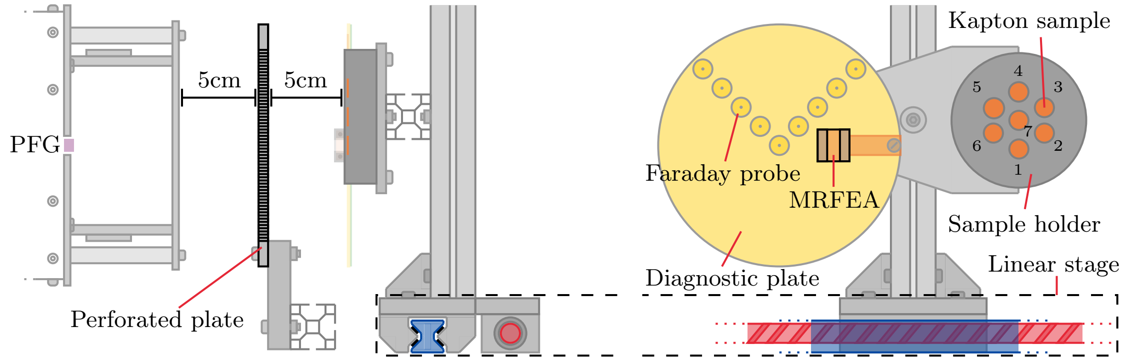

(a) Side view of the setup (b) Front view of the movable parts

Figure 5.22: Schematic representation of the Kapton degradation test setup. The sample holder and the diagnostic plate are mounted on the linear stage to align a specific point (either the center Faraday probe, the MRFEA or sample n°1) with the center of the particle flow.

ment of a selected element with the centerline of the particle flow.

The linear stage translational movement allow the positioning of the Faraday probes, the MRFEA, or a Kapton sample at the center of the plasma flow. This configuration ensures that diagnostic measurements and material exposure are performed under identical conditions conditions.

The plate is positioned 5 cm downstream of the PFG exit plane and the samples as well as the diagnostic plate are positioned 5 cm downstream of the back-face of the perforated plate. Although not depicted on Figure 5.22a, the plate is connected via a wire to a power supply outside of the vacuum chamber, as was done in the biased plate experimental setup.

The sample holder can accommodate 7 Kapton samples. Each slot is numbered following the nomenclature depicted in Figure 5.22b. The center of sample n°1 is horizontally aligned with the MRFEA and the central Faraday probe on the diagnostic plate, such that, when the linear stage is moved to its calibrated "Sample" position, sample n°1 is aligned with the centerline of the facility.

Each sample slot on the holder is regularly spaced with 1.8 cm between the center points. Each slot has a diameter of 1 cm. With sample n°1 considered the "central" sample, this arrangement enables the study of the radial distribution of the neutrals flow, if any is detected. The radial distribution of samples is such that $r_1 = 0\,\text{cm}$, $r_2 = r_6 = r_7 = 1.8\,\text{cm}$, $r_3 = r_4 = 3.12\,\text{cm}$ and $r_4 = 3.6\,\text{cm}$. Finally, for the sake of clarity, samples from the test performed with the thick AR7.5 perforated plate are denoted by the letter 'a' (e.g. sample n°1a) and for the test performed with the thin AR0.2 plate, they are denoted by the letter 'b' (e.g. sample n°4b).

The Kapton used for the samples themselves comes from a large $\sim 125\,\mu\text{m}$ thick sheet where circular holes have been cutout. Figure 5.23a shows a pristine (untouched) sample of Kapton. Figure 5.23b presents an example of the metallic meshes used to cover parts of the sample in order to have some unexposed area next to exposed ones for the sake of

(a) Pristine sample (b) Covering mesh (c) Exposed sample

Figure 5.23: Pictures of a pristine Kapton sample, a stainless steel covering mesh and a Kapton sample exposed to ionic oxygen for 5h from Jorge [8].

comparison. Finally, Figure 5.23c show a Kapton sample that has been exposed for 5h to an argon-oxygen mixture plasma flow in reference conditions. This particular sample comes from a previous material degradation experimental campaign by Jorge et al. [36].

5.5.3 Test conditions

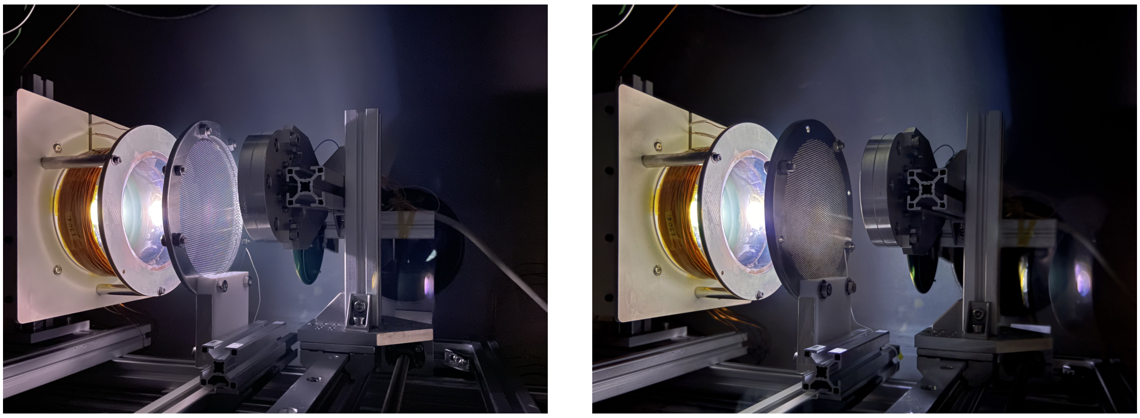

(a) AR0.2 plate. (b) AR7.5 plate.

Figure 5.24: Pictures of the tests during exposure. On each picture, from left to right, there is the PFG, the perforated plate and the samples. The diagnostic plate is mounted on the linear stage next to the sample holder.

The exposure tests for the thin and thick plate were run on consecutive days in the DRAG-ON facility. Figure 5.24 shows photographs of the experimental setup in operation with the linear stage positioned at the calibrated “sample” location. Both tests were performed under the same operating conditions, as required by the design of this experimental campaign.

The choice of operating parameters for the degradation test was guided by several considerations, namely ion energy, ion acceleration, ion flux, neutralization efficiency, and operational safety constraints of the facility. Maximizing the probability of observing a measurable neutral flux requires high neutralization efficiency and avoiding excessive ion acceleration that would increase ion-induced erosion since there is no indication that neutral energies would follow a similar trend. In addition, sufficiently high particle fluxes and energies are required to produce a measurable degradation. Operational limits of the plasma source, biasing hardware and compliance with safety features in the facility are other parameters to take into account.

In the end, a single set of operating conditions was identified as the best compromise and was applied to both exposure tests. The working gas consisted of a mixture of 3 sccm of argon and 10 sccm of oxygen. The magnetic focusing coil current was set to $I_{\text{coil}} = 2\,\text{A}$, the electrode voltage to $V_{\text{elec}} = -10\,\text{V}$, and the perforated plate was biased to $V_{\text{plate}} = -20\,\text{V}$. During the exposure, the absorbed power was maintained between 77 and 73 W, and was manually adjusted over time to ensure that the reflected power remained below the 10 W operational limit of the plasma generator. The AR7.5 exposure test lasted 8 h, while the AR0.2 test was conducted over 6 h, both constrained to fit within a single day of operation. These conditions were previously investigated using the biased plate setup to characterize flow properties and determine the apparent neutralization efficiency for the AR7.5 plate, yielding a core-averaged apparent neutralization efficiency of $\overline{\eta}_{\text{core}} = 94.0\,\%$.

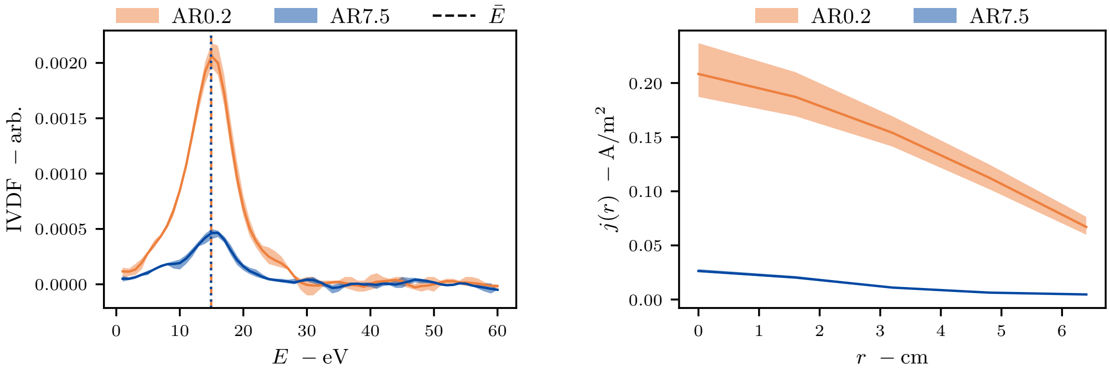

(a) Range of IVDF with average (full line) for both tests.

(b) Range of ion current density with average (full line) for both tests.

Figure 5.25: Measurement of flow conditions downstream of the perforated plate during both AR0.2 and AR7.5 exposure tests. Measurements were taken at the start, mid-point and end of each test, hence the uncertainty highlighted on the measured quantities.

Figure 5.25 presents the flow conditions measured downstream of the perforated plate for both exposure tests. Since the operating conditions evolve slightly over the duration of the test (the absorbed power value) a range of values is reported with the average highlighted. The ion current density and IVDF measured during the AR7.5 exposure test were particularly stable over time. The average ion energy was measured to be 14.91 eV for the AR0.2 test and 14.88 eV for the AR7.5 test, confirming that both exposures were performed under nearly identical energetic ion conditions. The floating potential is measured to stay in the range $V_f \in [-14.2, -12.5]\,\text{V}$, the electronic conditions are similar in both cases. The corresponding ion fluence values and associated uncertainties are reported in Table 5.3 and Table 5.2.

5.5.4 Erosion depth measurement

One of the critical aspects of this experimental campaign is the ability to measure very small erosion depths with sufficient accuracy and repeatability. The reference method for such measurements would normally involve a confocal laser scanning microscope (Olympus OLS 5000), a stylus contact profilometer (Dektak 8) and low-cost in-house stylus roughness tester (Mitutoyo SJ201P). Such measurements have been successfully employed in the context a PhD thesis by Pedro Jorge [8]. The first two measurement instruments, which are much more accurate then the third option, are operated by the department of materials and chemistry of the Vrije Universiteit Brussel (VUB). However, due to the tight time constraints associated with the Kapton degradation test campaign, access to these facilities was not possible within the required time-frame.

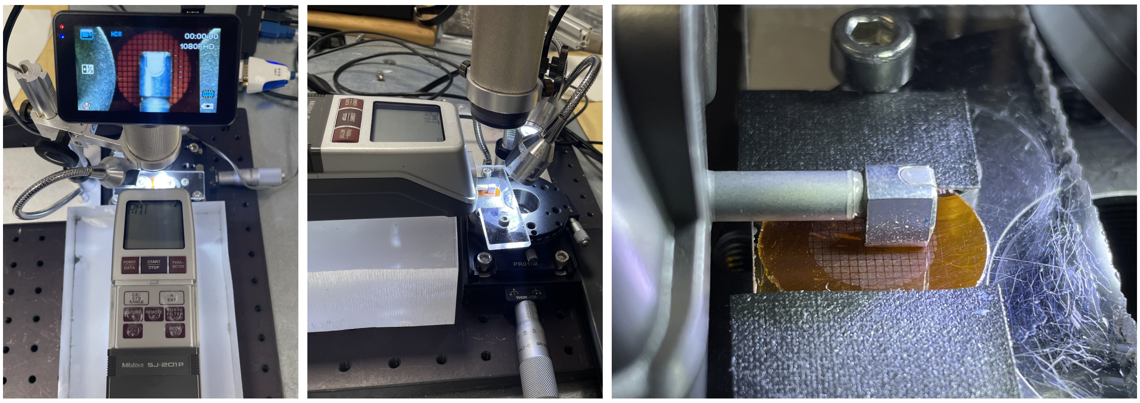

(a) Top view. (b) Side view. (c) Close-up on the stylus and sample.

Figure 5.26: Erosion depth measurement setup composed of the Mitutoyo SJ201P roughness meter, a macro lens camera and a combination of a micrometer translational stage and a micrometer rotational stage for sample alignment.

The in-house alternative is implemented using a contact roughness meter capable of exporting full height profiles point-by-point. The measurement setup, shown in Figure 5.26, consists of a Mitutoyo SJ201P roughness meter, a macro-lens camera for visual alignment, and a combination of micrometer translation and rotation stages for precise sample positioning. The working principle of the device relies on a stylus mechanically scanning the surface along a predefined line, producing a height profile with a nominal vertical resolution of 0.01 μm. While this resolution is sufficient for the erosion depths measure, the method is really sensitive to surface roughness, local defects, and measurement noise, particularly when operating at the sub-micron scale which is the case of the AR7.5 test Kapton erosion.

The profilometer stylus is aligned with the mesh imprint on the sample surface, and 26 parallel scans are performed across the exposed region. Each parallel scan is space by 50 μm and the measurement profile length is set to 2.5 mm. The final size of the scanned area is $2.5 \times 1.25\,\text{mm}^2$. This approach provides a quasi-three-dimensional reconstruction of the surface, offering a more statistically robust approach than isolated single-line measurements. By sampling a large number of profiles, it becomes possible to identify and

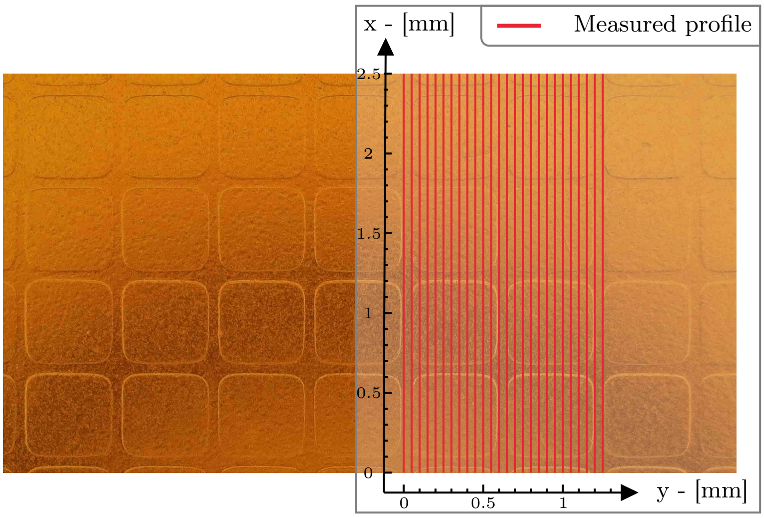

Figure 5.27: Microscopic view of sample n°7b exposed for 6h to the particle flow with the AR0.2 plate. Overlaid on top is a representation of the profiles measured with the SJ201P roughness meter.

filter out macroscopic artifacts or localized defects during post-processing. Figure 5.27 illustrates the correspondence between the physical erosion pattern and the locations of the profilometer scan lines.

Post-processing

The raw data obtained from the SJ201P roughness meter are noisy and affected by macroscopic trends unrelated to physical erosion. As such, post-processing is required to extract meaningful and accurate erosion depths. It's important to pay attention that the processing steps do not artificially alter the data or introduce bias. All assumptions must therefore be physically justified and explicitly stated. The expected surface morphology consists of ridge regions, corresponding to areas protected by the mesh and assumed to remain pristine, separated by eroded pit regions exposed to the particle flow. The quantity of interest is the average height difference between these two regions. The plane set by the average of ridge points is assumed to be the flat top surface reference at a height $z = 0$.

Figure 5.28a shows an example of a raw height profile measured on sample n°1b from the AR0.2 test. The data exhibit significant noise and a pronounced macroscopic trend that is unlikely to be physical, and may originate from sample misalignment, stylus loading effects, or local defects. Nevertheless, ridge and pit regions are clearly identifiable by visual inspection, and an underlying flat reference surface can be inferred.

The first post-processing step consists of fitting a smooth reference curve to the raw profile in order to remove the large-scale trend and flatten the data. This fit is intentionally biased toward the lower portions of the profile, corresponding to the pit regions, and is designed to minimize the influence of the ridges during this initial flattening step. The result of this procedure is shown in Figure 5.28a.

In a second step, ridge and pit reference points are identified on the flattened profiles,

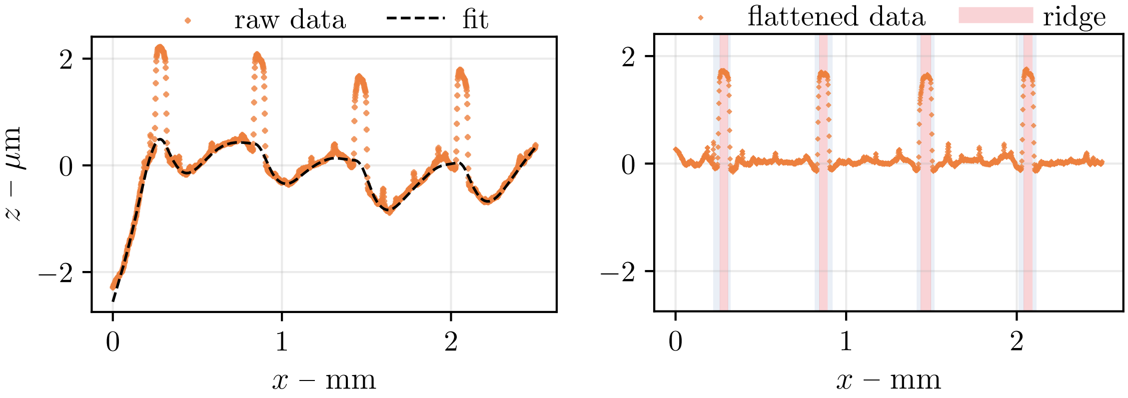

(a) Raw data with first fit. (b) Flattened data with ridge selection.

Figure 5.28: Raw data from the SJ201P roughness meter with the first step fitting and ridge points selection.

as illustrated in Figure 5.28b. This classification is a crucial prerequisite for the subsequent global surface fitting, as the ridge regions define the pristine reference surface against which erosion depths are measured. Here each data point is assigned a category which is either "ridge", "pit" or "intermediate". Intermediate points being the points representing the increasing and decreasing slopes either side of the ridges.

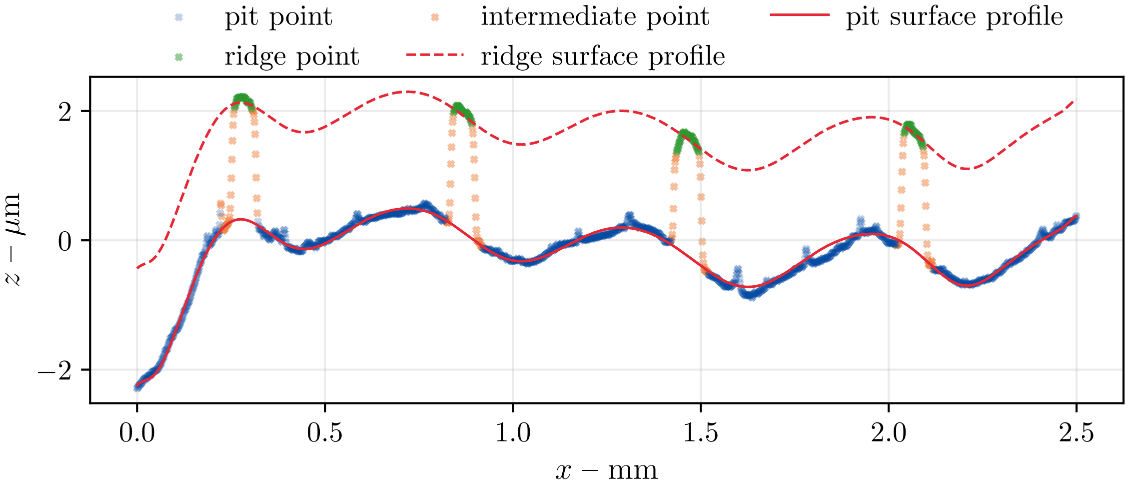

Figure 5.29: Profile showing the raw height measurement at $y = 0.4\,\mathrm{mm}$ on sample n°1b, together with the fitted ridge and pit reference surface intersections.

The final post-processing step consists of performing a global double-surface fit over the entire dataset in order to reduce the influence of per-profile noise and local measurement irregularities [39, 40]. Two parallel reference surfaces are fitted simultaneously: one representing the intact ridge surface and one representing the eroded pit surface. Both surfaces share the same spatial shape and differ only by a constant vertical offset, which is interpreted as the erosion depth.

The reference surface is modeled as a two-dimensional polynomial of degree N,

$$z_{\text{ridge}}(x, y) = \sum_{i+j \leq N} a_{ij}\, x^i y^j,$$

while the pit surface is defined as

$$z_{\text{pit}}(x, y) = z_{\text{ridge}}(x, y) - d,$$

where d is a constant offset representing the average material removal depth.

The polynomial coefficients $\{a_{ij}\}$ and the offset d are obtained simultaneously through a weighted least-squares optimization. Ridge points are assigned a higher weight than pit points, reflecting their role as the primary, non-eroded reference surface, while pit points constrain the vertical offset. A non-negativity constraint is imposed on d to ensure physical consistency.

By enforcing strict parallelism between the two surfaces, this approach provides a physically meaningful interpretation of erosion as a uniform normal material removal from the original surface geometry, while remaining robust to local defects, outliers, and profile-to-profile variability.

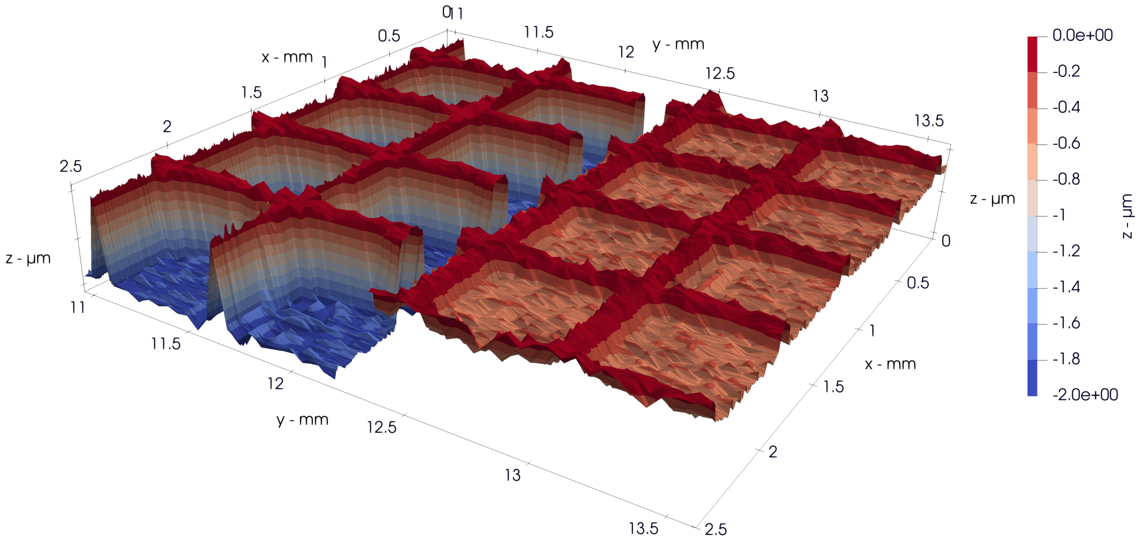

Figure 5.30: 3D reconstruction of the processed surfaces of sample n°1b of the AR0.2 test (rear left) and sample n°1a of the AR7.5 test (front right). The z-axis is scaled (×200) for visualization purposes.

Finally, a three-dimensional reconstruction of the processed profiles is shown in Figure 5.30. The vertical scale is exaggerated to emphasize the relative magnitude and spatial distribution of erosion. It provides a qualitative overview that complements the quantitative erosion depth analysis.

5.5.5 Results

Tables 5.2 and 5.3 summarize the results of the Kapton degradation experiments and allow two limiting cases to be examined: the presence or absence of a measurable contribution from fast neutrals downstream of the perforated plate, as described in Section 5.5.1.

Table 5.2: Ion-only reference quantities obtained from the AR0.2 degradation test. Ranges reflect min-max conditions during exposure.

Sample n°	Y_i [$10^{-23}\,\mathrm{cm}^3/\mathrm{ion}$]	d_1 [μm]	$F_{i,1}$ [$10^{22}\,\mathrm{ions/m}^2$]
1b	5.88 - 7.19	1.819	5.0 - 6.1
2b	5.39 - 6.45	1.449	3.7 - 4.4
4b	6.02 - 7.02	1.255	1.8 - 2.2

The AR0.2 results reported in Table 5.2 serve as the ion-only reference. For this thin plate geometry, the assumption that no (significant) neutralization occurs in this configuration. The inferred ion fluences $F_{i,1}$ are of the order of $10^{22}\,\mathrm{ions/m}^2$ and vary between samples as a consequence of slightly different exposure conditions as a function of the sample radial position. These values provide a robust experimental baseline to estimate ion-induced erosion yields Y_i, which are then reused for the analysis of the AR7.5 tests.

Table 5.3: Summary of Kapton degradation test results for the AR7.5 plate. Expected erosion depths $d_{2,i}$ are computed from the ion-only AR0.2 reference (Table 5.2). Excess erosion is attributed to fast neutrals when above uncertainty. Ranges reflect min-max conditions during exposure.

n°	Y_i [$10^{-23}\,\mathrm{cm}^3/\mathrm{ion}$]	$F_{i,2}$ [$10^{22}\,\mathrm{ions/m}^2$]	$d_{2,i}$ [μm]	d_2 [μm]	$d_{2,n}$ [μm]
1a	5.88 - 7.19	0.451 - 0.494	0.270 - 0.361	0.477	0.116 - 0.207
2a	5.39 - 6.45	0.328 - 0.363	0.180 - 0.238	0.314	0.076 - 0.134
4a	6.02 - 7.02	0.169 - 0.185	0.103 - 0.132	0.138	0.006 - 0.035

The AR7.5 results in Table 5.3 exhibit two distinct behaviors. For samples 1a and 2a, the measured erosion depth d_2 significantly exceeds the ion-only prediction $d_{2,i}$ derived from the AR0.2 reference. The excess erosion $d_{2,n}$ remains well above zero even when accounting for the uncertainty range associated with min-max measured conditions over the exposure duration. In these cases, the inequality $d_{2,n} \gg 0$ is satisfied, indicating a clear and measurable contribution from fast neutrals. This provides direct experimental evidence that the AR7.5 perforated plate induces a significant neutralization of the flow, leading to additional material erosion not attributable to ions alone.

In contrast, sample 4a corresponds to a marginal case. Although the measured erosion depth d_2 is slightly larger than the ion-only expectation, the inferred neutral contribution $d_{2,n}$ remains comparable to the uncertainty level. In this configuration, it is not possible to truly distinguish between a weak neutral-induced erosion and experimental scatter. This case therefore falls into the regime where $d_{2,n} \approx 0$ within uncertainty, and no firm conclusion regarding the presence of fast neutrals can be drawn.

Taken together, these two edge cases illustrate both the capability and the limitation of the Kapton degradation test. When the excess erosion clearly exceeds uncertainty, the test provides strong evidence for flow neutralization downstream of the perforated plate. When the excess erosion approaches the noise floor, the method becomes inconclusive. Nevertheless, the existence of multiple configurations exhibiting $d_{2,n} \gg 0$ demonstrates that fast neutrals are indeed present for the AR7.5 plate, thereby validating that a neutralization mechanism exists.

An additional insight is obtained by considering the radial distribution of the studied Kapton samples. Samples 1, 2 and 4 are respectively located at $r = 0$, $r = 1.8\,\text{cm}$ and $r = 3.6\,\text{cm}$ from the beam axis. The results reported in Table 5.3 show that the magnitude of the excess erosion attributed to neutrals decreases with increasing radial position. At the beam center (sample 1a), the neutral-induced erosion $d_{2,n}$ is clearly significant and well above uncertainty. At an intermediate radius (sample 2a), a measurable but reduced neutral contribution is still observed. At the largest radius (sample 4a), the inferred neutral erosion becomes marginal and falls within experimental uncertainty.

This radial trend is consistent with a neutral flux that is strongest in the core of the flow and decreases toward the periphery, mirroring the apparent neutralization efficiency profiles. The disappearance of a clear neutral signature at $r = 3.6\,\text{cm}$ suggests that the effective neutralization is a function of radius. This could be expected considering all particles in the flow are all not perfectly axial but rather spread radially outwards, as suggested in Section 3.3. This means that the average angle at which an ion encounters a wall inside of the perforated plate channels increases with radius, lowering the probability of this particle going through the plate in few collisions.

5.5.6 Discussion on results validity

The Kapton degradation test is an indirect diagnostic: it does not measure the neutral flux in real time, but infers it from post-test erosion depth measurement. Because of that, the main question is not only *"is $d_{2,n} > 0$?"* but also *"is the inferred $d_{2,n}$ physically plausible under reasonable assumptions?"* The sanity-check presented here answers that second question by verifying that the measured excess erosion can be produced by a neutral flux consistent with the independently measured neutralization efficiency.

The AR7.5 campaign measured a core-averaged apparent neutralization efficiency $\eta = 0.94$ for the specific conditions of the erosion tests. In the simplest particle-balance picture, the downstream ion fluence $F_{i,2}$ represents the non-neutralized fraction, while the neutralized fraction is converted into fast neutrals. Assuming one fast neutral per neutralized ion, the maximum neutral fluence compatible with η is

$$F_{n,2}^{\max} = \frac{\eta}{1-\eta} F_{i,2}. \tag{5.18}$$

From the data presented in Table 5.3, a range of maximal neutral fluence is given for each sample, $F_{n,2}^{\max} = 7.07\text{-}7.75 \times 10^{22}\,\text{m}^{-2}$ (sample 1a), $5.14\text{-}5.68 \times 10^{22}\,\text{m}^{-2}$ (sample 2a), and

2.65-2.91 × $10^{22}\,\mathrm{m}^{-2}$ (sample 4a).

To translate a neutral fluence into erosion depth, a neutral erosion yield Y_n must be assumed. A widely used reference value for atomic oxygen neutrals at 5 eV energy is

$$Y_n(5\,\mathrm{eV}) = 3.0 \times 10^{-24}\,\mathrm{cm}^3/\mathrm{atom}\ [41], \tag{5.19}$$

and the scaling with energy is taken as

$$Y_n(E) = Y_n(5\,\mathrm{eV}) \left(\frac{E}{5\,\mathrm{eV}}\right)^{0.68} \quad [42]. \tag{5.20}$$

The remaining missing piece is the neutral energy after the perforated plate. Literature on particle transmission through grids/plates commonly reports that particles retain only a fraction $\alpha \in [0.3, 0.5]$ of their incoming energy [26]. This implies

$$E_n = \alpha E_{in}. \tag{5.21}$$

Using $E_{in} \approx 15.6\,\mathrm{eV}$ (from the MRFEA measurements), this gives a plausible neutral energy window of approximately $E_n \simeq 4.67\text{-}7.79\,\mathrm{eV}$.

If *all* neutralized ions produced fast neutrals ($\varepsilon = 1$ effectiveness), the maximum neutral-only erosion depth would be

$$d_n^{\max}(E_n) = F_{n,2}^{\max}\, Y_n(E_n). \tag{5.22}$$

Over the plausible energy window (4.67-7.79 eV), this yields:

- Sample 1a: $d_n^{\max} \approx 0.203\text{-}0.314\,\mu\mathrm{m}$,
- Sample 2a: $d_n^{\max} \approx 0.147\text{-}0.230\,\mu\mathrm{m}$,
- Sample 4a: $d_n^{\max} \approx 0.076\text{-}0.118\,\mu\mathrm{m}$.

These maximum depths are of the same order of magnitude as the measured excess depths and generally larger, which is expected because they correspond to a best-case conversion of neutralization into fast neutrals.

To quantify how demanding the comparison is, an effectiveness factor $\varepsilon \in [0, 1]$ is introduced, representing the fraction of the theoretical maximum neutral fluence that actually behaves as fast neutrals able to erode Kapton. The required effectiveness to reach the observed neutral erosion ranges is given by

$$d_{2,n} \approx \varepsilon\, F_{n,2}^{\max}\, Y_n(E_n) \qquad \Rightarrow \qquad \varepsilon_{\mathrm{req}} = \frac{d_{2,n}}{F_{n,2}^{\max} Y_n(E_n)}. \tag{5.23}$$

A required effectiveness $\epsilon_{\mathrm{req}} \leq 1$ is physically plausible because it means that the measured excess erosion can be explained by at most the neutral flux allowed by the independently measured neutralization efficiency, without the need for more fast neutrals than can actually be produced by the ion-to-neutral conversion process.

For all samples and all energies in the plausible window, the computed required effectiveness range is:

- Sample 1: $\varepsilon_{\text{req}} \approx 0.37\text{-}1.02$ (worst-case just at the edge of 1 when using the lowest neutral energy and most conservative combination of ranges),
- Sample 2: $\varepsilon_{\text{req}} \approx 0.33\text{-}0.91$,
- Sample 4: $\varepsilon_{\text{req}} \approx 0.05\text{-}0.46$.

This is the most important outcome of this sanity-check: the excess erosion measured in the AR7.5 test does not require an unphysical neutral flux or an effectiveness greater than 1. In other words, the degradation results are consistent with the independently measured neutralization efficiency, a reasonable neutral energy loss through the plate, and a standard neutral erosion yield model.

Under the assumptions listed above, the inferred excess depths $d_{2,n}$ are quantitatively compatible with a fast-neutral contribution. This does not prove the uniqueness of the presented solution (other unmodeled effects such as flow species composition could contribute), but it shows that the magnitudes reported in Table 5.3 are physically credible and do not contradict the measured efficiency of the perforated-plate neutralizer.

Chapter 6

Conclusion

This thesis focus was to improve the representativeness of the DRAG-ON facility for Very Low Earth Orbit (VLEO) conditions. More specifically, the objective was to reduce the ionic fraction of the particle flow generated by the PFG, and to move toward a directed flow of fast neutrals that can be used for ABEP intake testing and for satellite material degradation studies.

A first important contribution of this work is the definition of a practical metric to quantify neutralization based on experimental data. Contrary to earlier approaches where a "naive" neutralization efficiency was estimated from geometric assumptions (based on the open area ratio of the plate), the definition introduced here is directly built from empirical data. New hardware, namely the AR0.2 plate, was manufactured specifically for this purpose. It shares the same geometry as other perforated plates available with exception of the aspect ratio. Such a thin plate is assumed not to cause any significant neutralization. In this thesis, the apparent neutralization efficiency is therefore defined from the reduction of measured ion flux comparing a setup with and without the AR0.2 plate installed.

Using this metric, the experimental campaigns show that the perforated plate neutralizer covers a wide range of apparent efficiencies highly dependent on flow conditions and operating parameters. A systematic study of efficiency sensibility to every tunable parameters forms a large dataset that, after analysis, offers great insight on the phenomenon at hands. The main trends are consistent and clear: increasing the aspect ratio enhances neutralization, and higher flow rates and/or power settings generally increase efficiency as well. Overall, the perforated plate approach is validated as a practical and scalable method to strongly reduce the transmitted ion current while maintaining a globally axial flow.

However, an important limitation was identified: the presence of the plate is associated with an apparent acceleration of the ions, observed as an increase of the most probable ion energy measured downstream. This effect, converging to a common energy regardless of electrode voltage, disables the controllable nature of the ion flow properties. This effect is a major problem since VLEO representativeness is not only about neutral species, but also about energy, with orbital conditions corresponding to around ~ 5 eV for atomic oxygen.

Dedicated experimental campaigns were designed to enlarge the empirical dataset on this apparent ion acceleration phenomenon. Results of an initial setup, where the perforated plate is grounded, highlight that electrode voltage is the main controllable parameter influencing ion acceleration. Floating potential is also shown to be highly correlated to this phenomenon, hinting at the influence of plasma potential, which is not currently measurable in DRAG-ON. Another notable results is the observed independence of ion acceleration from plate aspect ratio.

In a subsequent test, the plasma source is kept in its grounded state and the perforated plate itself is biased. The results show a clear relationship between plate bias and ion acceleration, this time with the ability to decelerate ions. The combination of this effect with variable electrode voltage on the source allows for regained control on ion flux energy.

Finally, a novel experimental setup was designed to indirectly measure neutral flux from polyimide (Kapton) erosion measurements. This test consists in the long exposure of Kapton samples to specific flow conditions downstream of the AR7.5 perforated plate. A second exposure test with fresh samples is conducted in the same flow conditions with the exception of the perforated plate being the AR0.2 one. The ion flux in both case is measured downstream of the plate. After measuring the erosion depth of each sample with an in-house precision profilometer, an ion erosion yield is estimated. From the result that apparent ion acceleration is independent of plate aspect ratio, this erosion yield is then used to compute an expected ion degradation depth for the AR7.5 test. The results provide a strong indication that a significant neutral contribution exists downstream of the perforated plate, the measured depth being significantly beyond what would be expected from ions alone. These findings are further consolidated by a thorough discussion on the validity of these results under several realistic assumptions. However, this method remains indirect and does not provide a full characterization of the neutral flux since it is not able to dissociate neutral fluence and energy, which limits the interpretation.

In summary, this work shows that perforated plate neutralization is a promising and operationally compatible solution for DRAG-ON, but that the neutralization process still requires further research before it can be considered fully controlled and fully representative. Future work should therefore

- continue improving and refining the neutralization concept, including exploring other innovative neutralizer designs to reach a more robust and possibly closer-to-100% conversion, and
- develop stronger neutral diagnostics to directly quantify neutral flux properties.

Only with a combination of efficient neutralization and accurate neutral characterization will DRAG-ON be able to provide a truly VLEO-representative flow for ABEP intake testing and satellite material degradation studies.

References

[1] T. Andreussi, G. Cifali, V. Gianetti, A. Piragino, E. Ferrato, A. Rossodivita, M. Andrenucci, J. Longo, and L. Walpot. “Development and experimental validation of a Hall effect thruster RAM-EP concept”. In: Georgia Institute of Technology, Atlanta, Georgia, USA, 2017.

[2] D. Rafalskyi and S. Dudin. “Plasma source for simulating ionosphere and upper atmosphere environments at low Earth orbits”. en. In: *Vacuum* 241 (Nov. 2025), p. 114597.

[3] G. A. Bird. “Molecular gas dynamics and the direct simulation of gas flows”. eng. Reprinted. Oxford engineering science series 42. Oxford: Clarendon Press, 2003.

[4] D. L. Brown, M. L. R. Walker, J. Szabo, W. Huang, and J. E. Foster. “Recommended Practice for Use of Faraday Probes in Electric Propulsion Testing”. en. In: *Journal of Propulsion and Power* 33.3 (May 2017), pp. 582–613.

[5] D. Rafalskyi, S. Dudin, and A. Aanesland. “Magnetized retarding field energy analyzer measuring the particle flux and ion energy distribution of both positive and negative ions”. en. In: *Review of Scientific Instruments* 86.5 (May 2015), p. 053302.

[6] A. Spethmann, T. Trottenberg, H. Kersten, F. G. Hey, L. Grimaud, S. Mazouffre, D. Bock, and M. Tajmar. “Force probes for development and testing of different electric propulsion systems”. en. In: *EPJ Techniques and Instrumentation* 9.1 (Dec. 2022), p. 4.

[7] D. Lee, J. Bae, S. Park, and G. Yeom. “Development of a low angle forward reflected neutral oxygen beam for materials processing”. en. In: *Thin Solid Films* 398-399 (Nov. 2001), pp. 647–651.

[8] P. D. C. Jorge. “Gas and plasma surface interactions in hyperthermal rarefied flows: application to very low earth orbit platforms”. en. PhD thesis. Vrije Universiteit Brussel, 2025.

[9] M. Drinkwater, R. Haagmans, and D. Muzi. “The GOCE Gravity Mission”. en. In: *Proceedings of the 3rd International GOCE User Workshop*. Frascati, Italy, 2006.

[10] S. Imamura, M. Sasaki, Y. Yamamoto, T. Sakamoto, and T. Ozawa. “Attitude and Orbit Control Result of Super Low Altitude Test Satellite “TSUBAME” (SLATS)”. en. In: *JOURNAL OF THE JAPAN SOCIETY FOR AERONAUTICAL AND SPACE SCIENCES* 69.1 (2021), pp. 35–41.

[11] P. Parodi. “Modeling and particle methods for plasma simulation applied to Air-Breathing Electric Propulsion”. en. PhD thesis. KU Leuven, 2025.

[12] C. Brabants. “Master thesis and internship[BR]- Master’s thesis : Development of a methodology for VLEO intake performance testing in a low density facility[BR]-Integration internship”. en. MA thesis. Université de Liège, 2021.

[13] B. Fontaine. “Rebuilding Optical Emission Spectroscopy Measurements in a Low Density Plasma Facility using a Collisional-Radiative Model”. en. MA thesis. Université de Liège, 2023.

[14] G. Pascoli. “Generation of VLEO-Representative Flows Through Plasma Neutralization”. MA thesis. Université Libre de Bruxelles, 2025.

[15] K. Swaminathan-Gopalan and K. A. Stephani. “Recommended direct simulation Monte Carlo collision model parameters for modeling ionized air transport processes”. en. In: *Physics of Fluids* 28.2 (Feb. 2016), p. 027101.

[16] D. Rafalskyi. “RF Plasma Flow Generator for LEO Environment Simulation: Use Cases”. en. In: *th International Electric Propulsion Conference* (2024).

[17] F. F. Chen. “Introduction to Plasma Physics and Controlled Fusion”. en. Cham: Springer International Publishing, 2016.

[18] M. A. Lieberman and A. J. Lichtenberg. “Principles of Plasma Discharges and Materials Processing”. en. 1st ed. Wiley, Apr. 2005.

[19] R. Shastry, R. R. Hofer, B. M. Reid, and A. D. Gallimore. “Method for analyzing E×B probe spectra from Hall thruster plumes”. en. In: *Review of Scientific Instruments* 80.6 (June 2009), p. 063502.

[20] C. Birdsall. “Particle-in-cell charged-particle simulations, plus Monte Carlo collisions with neutral atoms, PIC-MCC”. en. In: *IEEE Transactions on Plasma Science* 19.2 (Apr. 1991), pp. 65–85.

[21] J. C. Tully. “Neutralization of ions at surfaces”. en. In: *Physical Review B* 16.10 (Nov. 1977), pp. 4324–4334.

[22] H. D. Hagstrum. “Ion-Neutralization Spectroscopy of Solids and Solid Surfaces”. en. In: *Physical Review* 150.2 (Oct. 1966), pp. 495–515.

[23] N. P. Wang, E. A. García, R. Monreal, F. Flores, E. C. Goldberg, H. H. Brongersma, and P. Bauer. “Low-energy ion neutralization at surfaces: Resonant and Auger processes”. en. In: *Physical Review A* 64.1 (May 2001), p. 012901.

[24] D. Goebl, D. Valdés, E. Abad, R. C. Monreal, D. Primetzhofer, and P. Bauer. “Band structure effects in Auger neutralization of He ions at metal surfaces”. en. In: *Physical Review B* 84.16 (Oct. 2011), p. 165428.

[25] M. Wieser and P. Wurz. “Production of a 10 eV–1000 eV neutral particle beam using surface neutralization”. en. In: *Measurement Science and Technology* 16.12 (Dec. 2005), pp. 2511–2516.

[26] Y. Hisamoto, K. Nishiyama, and H. Kuninaka. “Characteristics of Hyperthermal Atomic Oxygen Source Using Electron Cyclotron Resonance Discharge and Neutralization Grid”. en. In: *TRANSACTIONS OF THE JAPAN SOCIETY FOR AERONAUTICAL AND SPACE SCIENCES, AEROSPACE TECHNOLOGY JAPAN* 12.ists29 (2014), Pc_43–Pc_48.

[27] D. J. Economou. “Fast (tens to hundreds of eV) neutral beams for materials processing”. In: *Journal of Physics D: Applied Physics* 41.2 (Jan. 2008), p. 024001.

[28] S. K. Nam, D. J. Economou, and V. M. Donnelly. “Generation of Fast Neutral Beams by Ion Neutralization in High-Aspect-Ratio Holes: A Particle-in-Cell Simulation Study”. In: *IEEE Transactions on Plasma Science* 35.5 (Oct. 2007), pp. 1370–1378.

[29] Plasma Controls, LLC. *ExB Velocity Filter*. Company product webpage. Accessed 2026-01-05.

[30] T. Trottenberg, T. Richter, and H. Kersten. “Measurement of the force exerted on the surface of an object immersed in a plasma”. en. In: *The European Physical Journal D* 69.3 (Mar. 2015), p. 91.

[31] R. S. Hemsworth, J.-H. Feist, M. Hanada, B. Heinemann, T. Inoue, E. Küssel, V. Kulygin, A. Krylov, P. Lotte, K. Miyamoto, N. Miyamoto, D. Murdoch, A. Nagase, Y. Ohara, Y. Okumura, J. Pamela, A. Panasenkov, K. Shibata, M. Tanii, and M. Watson. “Design of the ITER Neutral Beam injectors”. en. In: *AIP Conference Proceedings*. Vol. 380. ISSN: 0094243X. Upton, New York (USA): AIP, 1996, pp. 504–517.

[32] F. Scholze and D. Spemann. “Design and performance test of a RF plasma bridge neutralizer”. In: (2019).

[33] R. G. Albridge, A. V. Barnes, and N. H. Tolk. “Neutralizer and Sample Chamber for the Atomic Oxygen Simulation System (AOSS)”. Tech. rep. NAS8 - 37748. Vanderbilt University: NASA, 1992.

[34] S. S. Swami, S. V. Bhoraskar, and V. L. Mathe. “Development of the Neutralizer Assembly to Obtain Atomic Oxygen Species Derived from ECR Oxygen Plasma.” en. In: *Acta Astronautica* (Nov. 2025), S0094576525007763.

[35] P. D. C. Jorge, M. Spillemaekers, D. Le Quang, A. Hubin, and T. Magin. “Progress in ground testing of intake-collector for Air-Breathing Electric Propulsion”. en. In: *2nd International Symposium on Very Low Earth Orbit Missions and Technologies*. Stuttgart, Germany, 2025.

[36] P. D. C. Jorge, M. Spillemaekers, D. Le Quang, T. Magin, P. Laha, H. Ottevaere, and A. Hubin. “Characterization of RF plasma degradation of Kapton® HN films”. en. In: *2nd International Symposium on Very Low Earth Orbit Missions and Technologies*. Stuttgart, Germany, 2025.

[37] P. Parodi, D. Le Quang, G. Lapenta, and T. Magin. “Particle-in-Cell simulation of the VKI DRAG-ON facility”. en. In: *AIAA SCITECH 2024 Forum*. Orlando, FL: American Institute of Aeronautics and Astronautics, Jan. 2024.

[38] R. Kaufman. “Ion source design for industrial application.” en. In: *Department of Physics Colorado State University Fort Collins, Colorado* (1981).

[39] P. Podulka. “Selection of reference plane by the least squares fitting methods”. en. In: *Advances in Science and Technology Research Journal* 10.30 (2016), pp. 164–175.

[40] W. Graboń and P. Pawlus. “Distinguishing the Plateau and Valley Components of Profiles From Various Types of Two-Process Textures”. en. In: *Metrology and Measurement Systems* 23.4 (Dec. 2016), pp. 593–602.

[41] K. K. de Groh and B. A. Banks. “Atomic oxygen erosion data from the MISSE 2-8 missions”. In: (2019).

[42] B. A. Banks, S. K. Rutledge, and P. E. Paulsen. “Simulation of the Low Earth Orbital Atomic Oxygen Interaction With Materials by Means of an Oxygen Ion Beam”. en. In: ().

Appendix A

Angular distribution test results

This appendix presents the results of the angular distribution test campaign explained in Section 3.3. It first presents the axial evolution of the ion current density profiles. Then a representation of the trajectories with the ion current density highlighted. In reality, the images presented in Figure A.2 are not real trajectories but rather lines of constant cumulative current. Only a small number of lines are represented here for the sake of clarity, the actual discretization is much finer.

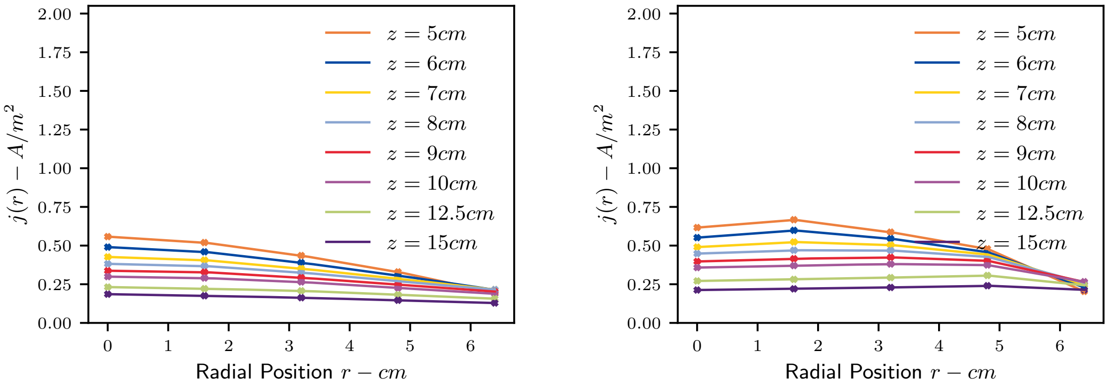

(a) $I_{\text{coil}} = 0A$.

(b) $I_{\text{coil}} = 0.5A$.

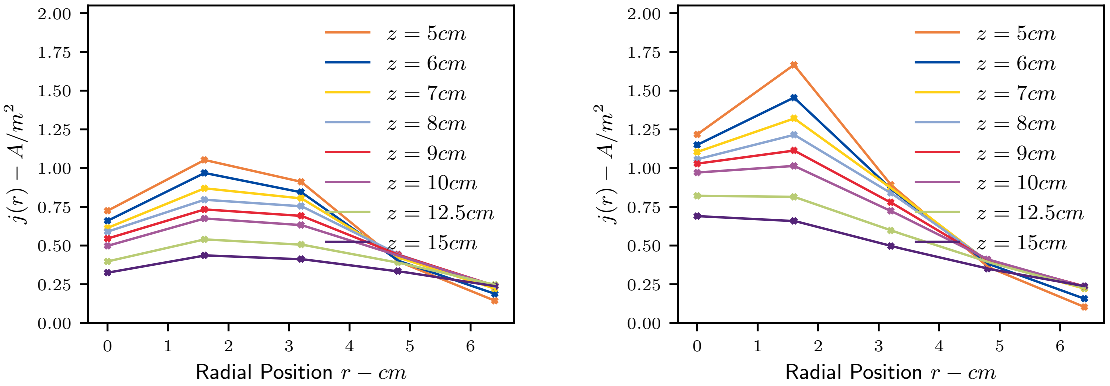

(c) $I_{\text{coil}} = 1A$.

(d) $I_{\text{coil}} = 1.5A$.

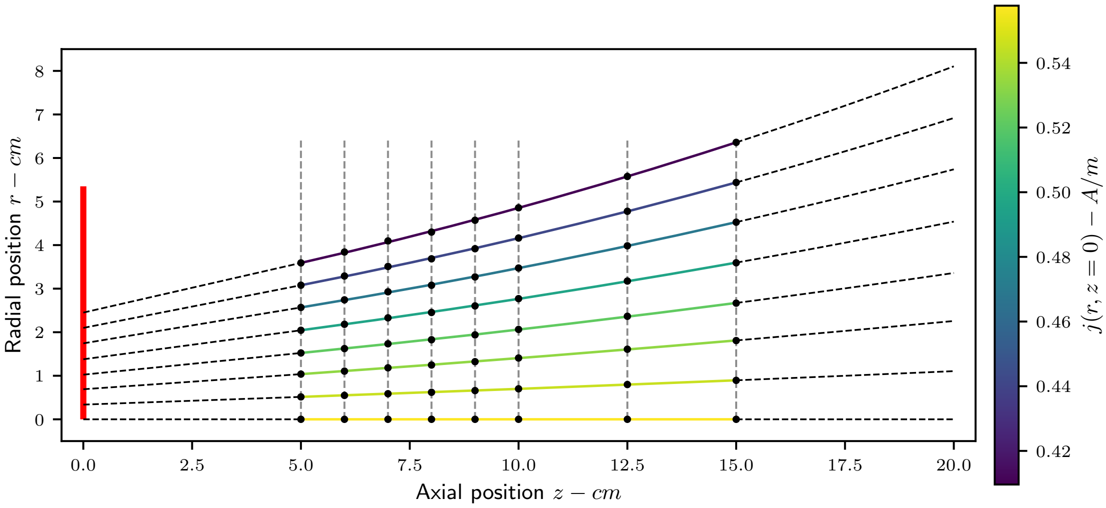

(a) $I_{\text{coil}} = 0A$.

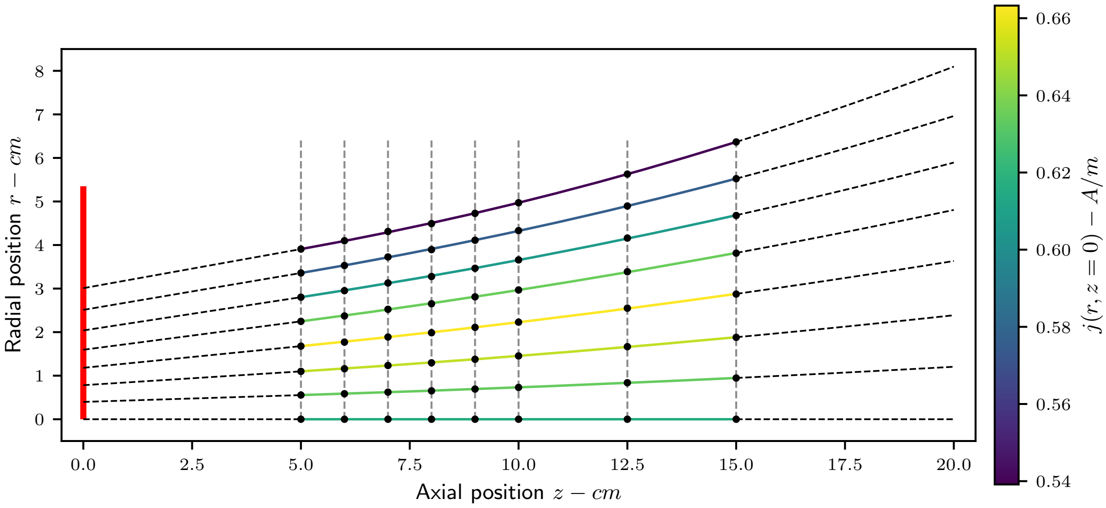

(b) $I_{\text{coil}} = 0.5A$.

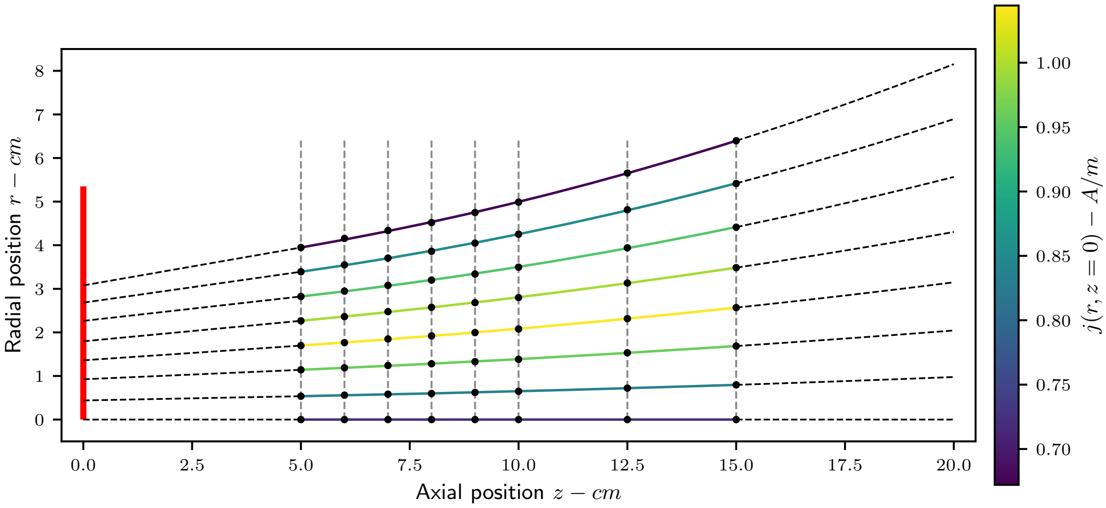

(c) $I_{\text{coil}} = 1A$.

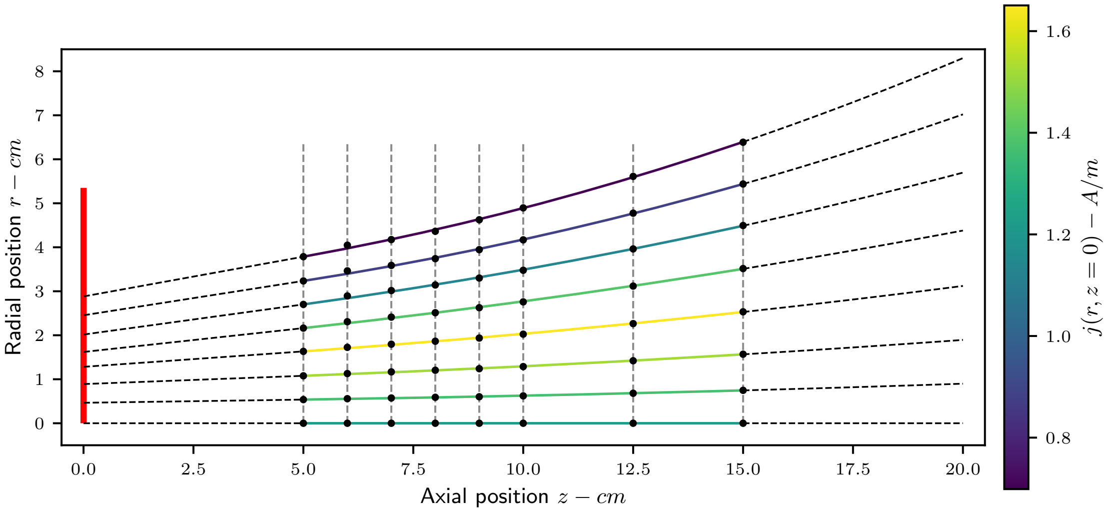

(d) $I_{\mathrm{coil}} = 1.5A$.

Figure A.2: Representation of the rays trajectory with quadratic fit. The ion current density value is taken on the base plane $z = 0$. The vertical red line represents the exit plane of the PFG.